Istraživanje modela kavitacije u računalnoj dinamici fluida

Primer, Niko

Master's thesis / Diplomski rad

2020

Permanent link / Trajna poveznica: https://urn.nsk.hr/urn:nbn:hr:235:910020

Download date / Datum preuzimanja: **2025-03-31**

Repository / Repozitorij:

Repository of Faculty of Mechanical Engineering and Naval Architecture University of Zagreb

UNIVERSITY OF ZAGREB

FACULTY OF MECHANICAL ENGINEERING AND NAVAL
ARCHITECTURE

MASTER'S THESIS

Niko Primer

ZAGREB, 2020

UNIVERSITY OF ZAGREB

FACULTY OF MECHANICAL ENGINEERING AND NAVAL
ARCHITECTURE

MASTER'S THESIS

A STUDY OF CAVITATION MODELS IN COMPUTATIONAL FLUID DYNAMICS

Mentor: Student:

prof. dr. sc. Hrvoje Jasak   Niko Primer

Statement | Izjava

I hereby declare that I have made this thesis independently using the knowledge acquired during my studies and the cited references.

Izjavljujem da sam ovaj rad radio samostalno koristeći znanja stečena tijekom studija i navedenu literaturu.

Zagreb, March 2020   Niko Primer

Sveučilište u Zagrebu	
Fakultet strojarstva i brodogradnje	
Datum	Prilog
Klasa:	
Ur. broj:	

DIPLOMSKI ZADATAK

Student: **Niko Primer** Mat. br.: 0035188608

Naslov rada na
hrvatskom jeziku: **Istraživanje modela kavitacije u računalnoj dinamici fluida**

Naslov rada na
engleskom jeziku: **A Study of Cavitation Models in Computational Fluid Dynamics**

Opis zadatka:

Practical performance limits of numerous engineering devices are directly dependent on the onset, intensity and form of cavitation appearing during operation. Examples include centrifugal pumps, ship propellers and hydrofoils of finned racing boats, such as the ones used in America's Cup. Predicting the onset, form and intensity of cavitation using Computational Fluid Dynamics presents a significant challenge today.

The objective of this study is to test the performance of existing cavitation models on cases relevant for hydrofoil geometries.

The candidate shall perform the following tasks within this project:

- Perform a literature survey of numerical models for cavitating flows and describe in detail the two most significant models, including their equation set and boundary conditions;
- Prepare a computational mesh for two geometries with available experimental or reference numerical results: a 2-D NACA 0009 truncated hydrofoil and a 3-D Delft Twist hydrofoil geometry;
- Perform numerical simulation assuming single-phase incompressible flow for both geometries as a non-cavitating benchmark;
- Perform a simulation of a cavitating flow for both geometries in transient simulation mode, with and without a turbulence model;
- Present a detailed analysis of numerical results for integral properties (lift and drag history), distribution of the pressure coefficient on hydrofoil surfaces, size and position of cavitation bubbles;
- If possible, perform a parametric study of mesh sensitivity of cavitating flow results for a 2-D hydrofoil simulation without a turbulence model;
- Report on experiences with the required mesh size, model convergence and difficulties in simulations.

The Thesis shall list the bibliography and any assistance received during this study.

Zadatak zadan: Datum predaje rada: Predviđeni datum obrane:

16. siječnja 2020. 19. ožujka 2020. 23. – 27.3.2020.

Zadatak zadao: Predsjednica Povjerenstva:

Prof. dr. sc. Hrvoje Jasak Prof. dr. sc. Tanja Jurčević Lulić

Contents

List of Figures

List of Tables

Nomenclature

Acronyms

Greek Symbols

Roman Symbols

p_h	[Pa]	Hydrostatic pressure	26
u_{inlet}	[m/s]	Fluid velocity entering the computational domain	39
k	[m^2/s^2]	Turbulent kinetic energy	21
m^+	[kg/m^3/s]	Condensation mass transfer	30
m^-	[kg/m^3/s]	Vaporization mass transfer	30
$\mathbf{n}$	[-]	Surface normal vector	6
p	[Pa]	Pressure	15
$\mathbf{q}_s$	[-]	Surface source	6
$\mathbf{q}$	[W/m^2]	Specific heat flux	9
q_v	[-]	Volume source	6
Q	[N/m^3]	Volumetric heat source	9
$\mathbf{R}$	[m^2/s^2]	Reynolds stress tensor	20
$\mathbf{r}$	[-]	Right-hand side vector	16
$\mathbf{r}_P$	[m]	Centroid position vector	9
S	[-]	Complex variable	14
S_f	[m^2]	Face surface area	9
S_m	[m^2]	Surface area of V_m	6
$\mathbf{s}_f$	[m^2]	Surface normal vector	9
s	[N/m]	Fluid surface tension	24
n_T	[-]	Tait law characteristic liquid constant	33
p_0	[Pa]	Tait law characteristic liquid pressure	33
T	[K]	Temperature	33
p_{ref}	[Pa]	Tait law reference pressure	33
$\mathbf{u}$	[m/s]	velocity vector	6
$\mathbf{U}$	[m/s]	Velocity scale	20
u_b	[m/s]	Bubble rise velocity	25
V	[m^3]	Material volume	6
p_v	[Pa]	Vapor pressure	26
V_m	[m^3]	Material volume	6
V_P	[m^3]	Volume of the cell	6
$\mathbf{x}$	[m]	Position vector	9

Superscripts

Subscripts

Sažetak

Kavitacija je prirodna pojava pare u struji kapljevine do koje dolazi zbog lokalnog pada tlaka, uzrokovanog efektima strujanja. Ona je štetna pojava koja narušava strukturu struje fluida, uzrokuje buku i vibracije, a može uzrokovati i oštećenja na strojnim elementima. Zbog toga je od izrazitog interesa proučavanje nastanka, te predviđanje kavitacije, radi suzbijanja mogućih neugodnih posljedica. Sa modernim napredkom tehnologije, u tu svrhu se danas sve više koristi Računalna Dinamika Fluida (RDF).

Ovaj rad objašnjava moderno poimanje nastanka kavitacije, te predstavlja matematičke modele koji opisuju ponašanje pare i kapljevine u kavitirajućim strujama. Uz to, prikazuje načine na koji se ti modeli primjenjuju u RDF-u, te pojednostavljenja modela koja se moraju uzeti u obzir.

U sklopu rada su obavljene simulacije u `foam-extend` i `OpenFOAM` programskim paketima, u svrhu validacije kavitacijskih modela. Cilj rada je bio usporediti Schnerr-Sauer kavitacijski model, odnosno implementaciju istog u `OpenFOAM`-u, sa eksperimentalnim rezultatima.

U tu svrhu su izvedene dvije računalne mreže. Prva je 2D mreža u kojoj je prikazano NACA009 krilo s podrezanim izlaznim bridom i korištena je za 2D simulacije strujanja. Druga je 3D mreža u kojoj je prikazano Delft Twist 11 krilo, te je korištena za potpune 3D simulacije strujanja.

Tijekom rada je obavljeno sveukupno 12 simulacija, od toga 8 na 2D mreži i 4 na 3D mreži. Za svaku pojedinu brzinu strujanja odradile su se 4 simulacije. Simulirano je strujanje sa pojavom kavitacije i bez nje, te za svaki slučaj jedno strujanje sa modeliranjem turbulencije, te bez turbulencije. Rezultati simulacija su uspoređeni sa eksperimantalnim rezultatima iz drugih radova.

Na kraju rada je dan osvrt na valjanost rezultata i trenutno stanje RDF istraživanja na području kavitacije.

Ključne riječi: RDF, kavitacija, Rayleigh - Plesset jednadžba, Schnerr - Sauer model, NACA009 krilo s podrezanim izlaznim bridom, Delft Twist 11 krilo, `foam-extend`, `OpenFOAM-7`

Abstract

Cavitation is a natural occurrence of vapor in a flow of liquid, caused by a local drop in pressure. It is a harmful occurrence that disrupts the flow, causes noise and vibrations, and can even inflict structural damage to machine elements. For these reasons, the study of cavitation inception is of particular interest, as is the ability to anticipate cavitation and facilitate the design of engineering devices to avoid the harmful side effects. Thanks to the modern advancements in technology, today, Computational Fluid Dynamics (CFD), is being applied in cavitation research.

This thesis explains the current understanding of cavitation inception and presents the mathematical models that describe the behavior of the vapor and liquid phase in cavitating flows. In addition it shows the methods and simplifications, with which those models are used in CFD.

In the scope of this thesis, simulations were performed using `foam-extend` and `OpenFOAM` software packages, with the purpose of validating the cavitation models. The goal of the thesis was to compare the `OpenFOAM` implementation of the Schnerr-Sauer cavitation model with experimental results.

With that in mind, 2 reference geometries were selected. The first is a 2D mesh in which the NACA009 Truncated Hydrofoil is situated, and it was used for the 2D flow simulations. The second is a 3D geometry in which the Delft Twist 11 Hydrofoil is situated, and it was used for 3D flow simulations.

In this study, a total of 12 simulations was performed. Out of those, 8 were on the 2D mesh, and 4 on the 3D mesh. For each inlet velocity, 4 simulations were performed. Both cavitating and non-cavitating flow was simulated, and for each experimental setup, one simulation with turbulence modeling and one without. The results were compared to experimental research results.

At the end of the thesis, a brief review of the results and the current state of CFD cavitation research was given.

Keywords: CFD, cavitation, Rayleigh - Plesset equation, Schnerr - Sauer model, NACA009 Truncated Hydrofoil, Delft Twist 11 Hydrofoil, `foam-extend`, `OpenFOAM-7`

Prošireni sažetak

Kavitacija je pojava pare u struji tekućina, do koje dolazi zbog pada tlaka. Ako tlak u struji padne ispod tlaka zasićenja za danu temperaturu tekućine, doći će do spontanog isparavanja i pojaviti će se parni mjehuri. Kako su isparavanje i konedenzacija vrlo brzi procesi, pogotovo u usporedbi sa dinamikom strujanja, takvi mjehuri, nakon nastanka mogu putovati nošeni strujom fluida u područja sa višim tlakom. Tada se mjehuri urušavaju, te, kada kapljevina ispunjava prostor mjehura, dolazi do tlačnih udara.

Štetne posljedice kavitacije su narušavanje toka fluida, buka, vibracije, a može doći i do oštećenja strojarskih dijelova. Među najčešća mjesta pojave kavitacije, ubrajaju se uska grla u ventilima, lopatice pumpi i turbina, te podvodna krila na brodovima.

Jake kohezivne sile među molekulama vode sprečavaju razdvajanje molekula, te time i razvoj parnih mjehura u vodi. Te kohezivne sile se često prikauju pomoću površinske napetosti vode, a pritisak koji vrše na mjehur pare u vodi se definira pomoću jednadžbe

$$p_{st} = \frac{2s}{R_b},$$

pri čemu je s površinska napetost vode, a R_b je polumjer mjehura pare.

Iz jednažbe se jasno vidi da je za beskonačno mali mjehur, pritisak p_{st} beskonačno velik, te bi se mjehur odmah urušio. Međutim, u realnim uvjetima, u vodi su uvijek prisutni mali mjehurići plinova, koji uvelike pomažu u nastajanju kavitacije. Budući da su mjehurići realne veličine, tlak zbog kohezivnih sila vode je konačno velik, te može doći do isparavanja vode u mjehurić i rasta kavitacije.

Sile adhezije između molekula vode i površine nekog drugog materijala su puno manje od sila kohezije, te stoga kavitacije često započinju na površinama strojarskih elemenata uronjenih u vodu.

Kavitacija je izuzetno stohastična pojava, i vrlo je teško točno predvidjeti intenzitet i posljedice kavitacije. Kroz povijest se istraživanje kavitacije primarno vršilo eksperimentalnim metodama u hidrotunelima, te je uključivalo snimanje kavitacije kamerama i mjerenje tlaka osjetnicima. Kako bi se mogli uspoređivati različiti uvjeti strujanja sa pojavom kavitacije, definirana je bezdimenzijska varijabla koeficijenta kavitacije

$$\sigma_{cav} = \frac{2(p_{outlet} - p_{vs})}{\rho_l u_{inlet}^2}.$$

Varijabla p_{vs} predstavlja vrijednost tlaka zasićenja, ρ_l je gustoća kapljevite faze, a u_{inlet} i p_{outlet} su vrijednosti koje definiraju uvjete strujanja, a predstavljaju brzinu kapljevine u slobodnoj struji i hidrostatski tlak na izlazu iz domene koja se promatra. Niži koeficijent kavitacije σ_{cav} odgovara intenzivnijoj pojavi kavitacije.

Ovakvo eksperimantalno istraživanje je skupo i dugotrajno zbog potrebe za razvijanjem prototipova modela geometrije. Danas se za istraživanje kavitacije sve više primjenjuje simulacija putem Računalne Dinamike Fluida (RDF), jer upravo pruža relativno jeftino i brzo rješenje uz veliku mogućnost prilagodbe uvjeta strujanja. Za potrebe RDF istraživanja, razvijeni su brojni modeli koji opisuju ponašanje parnih mjehura u struji fluida.

Matematički Modeli Kavitacije

Osnovni opis ponašanja parnih mjerhura prikazuje Rayleigh-Plesset jednadžba.

$$\frac{p_v + p_g - p_h}{\rho} = R_b \frac{\mathrm{d}^2 R_b}{\mathrm{d}t^2} + \frac{3}{2} \left(\frac{\mathrm{d}R_b}{\mathrm{d}t} \right)^2 + \frac{4\nu}{R_b} \frac{\mathrm{d}R_b}{\mathrm{d}t} + \frac{2s}{\rho R_b}.$$

S lijeve strane jednadžbe se nalazi razlika između, tlaka pare p_v i tlaka slobodnih plinova u mjehuru p_g, i hidrostatskog tlaka oko mjehura p_h, kao pokretač rasta mjehura. Desna strana jednadžbe opisuje dinamiku promjene volumena parnog mjehura prikazanog pomoću promjera mjehura R_b. Prikazan je utjecaj viskoznosti ν, površinske napetosti vode s, te član sa drugom derivacijom prikazuje inerciju rasta mjehura. Iako ovaj model opisuje ponašanje parnih mjehura u obliku sfere, i danas se smatra najrelevantnijom jednadžbom za opisivanje dinamike kavitacije, stoga se često primjenjuje za modeliranje kavitacije u području RDF-a.

Pri opisivanju kavitacije Metodom Kontrolnih Volumena (MKV), te primjenjivanju tih modela u RDF-u, mogu se identificirati 4 problema. Prvi problem je što je prisutno više faza u struji fluida. Zakoni očuvanja, se moraju zadovoljiti i za kapljevitu i za parnu fazu fluida, te je broj jednadžbi koje je potrebno riješiti veći. Drugi problem je modeliranje utjecaja jedne faze na drugu (tangencijalna naprezanja na granici među fazama). Treći problem proizlazi iz prirode MKV-a, a odnosi se na računanje položaja granice između faza. Zbog veličine diskretiziranih elemenata prostora, teško je modelirati oštru granicu između faza. Zadnji problem je računanje turbulencije i utjecaja turbulencije na kavitaciju. S tim problemima u vidu, razvijeno je nekoliko pristupa interpretiranju kavitacije.

U modeliranju kavitacije, najčešće se primjenjuju jednofazni modeli mješavine. Ovakvi modeli opisuju struju fluida kao mješavinu parne i kapljevite faze, uz uvođenje dodatne vrijednost α koja opisuje volumni udio parne faze u kontrolnom volumenu. Ovakvo pojednostavljenje smanjuje broj jednadžbi koje je potrebno riješiti na: zakone očuvanja za mješavinu i transportnu jednadžbu za α. Jedan od popularnijih modela za modeliranje α je Schnerr-Sauer model [8] koji se temelji na pojednostavljenoj Rayleigh-Plesset jednadžbi.

$$\frac{\partial \alpha}{\partial t} + \nabla \cdot (\alpha \mathbf{u}) = \left(\frac{n_0}{1 + \frac{4}{3}\pi R_b{}^2} \right) \frac{\mathrm{d}}{\mathrm{d}t} \left(\frac{4}{3}\pi R_b{}^3 \right)$$

Računalne Mreže i Postavke Simulacija

Cilj ovog rada je bio provjeriti točnost implementacije Schnerr-Sauer modela kavitacije u `OpenFOAM`-u. U tu svrhu provedene su simulacije strujanja vode sa, i bez pojave kavitacije. Simulacije su provedene kao 2D simulacije strujanja oko dvodimenzionalne geometrije profila NACA009 s podrezanim izlaznim bridom, te kao potpune 3D simulacije strujanja oko Delft Twist 11 krila.

Računalna mreža za simulacije strujanja oko NACA009 krila je izvedena kao 2D mreža sa 215,097 ćelija (Slika 1).
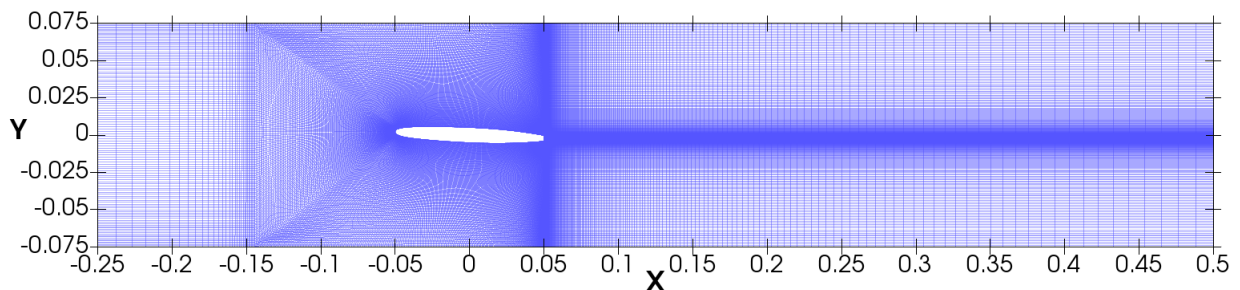
Slika 1: Računalna mreža oko NACA009 krila.

Provedene su simulacije strujanja za ulazne brzine strujanja od 20 m/s i 30 m/s. Za pojedinu brzinu, odrađena je simulacija za slučaj strujanja sa kavitacijom i bez pojave kavitacije, te za svaki od slučaja strujanje modelom turbulencije i bez njega. Za model turbulencije odabran je $k - \omega$ SST model. Sveukupno, na NACA009 mreži, provedeno je 8 simulacija. Slučajevi bez pojave kavitacije, riješeni su pomoću `simpleFoam` rješavača jednadžbi u programskom paketu `foam-extend 4.0`, dok su slučajevi sa kavitacijom riješeni pomoću `interPhaseChangeFoam` rješavača jednadžbi u programskom paketu `OpenFOAM-7`. Za model kavitacije odabran je Schnerr-Sauer model kavitacije, a vrijednosti tlaka u strujanju postavljene su u skladu sa kavitacijskim koeficijentom $\sigma_{cav} = 0.81$. Strujanja sa pojavom kavitacije, rješavana su kao tranzijentne simulacije koje prikazuju period od 0.2 sekunde. Tijekom simulacija, određene su sile uzgona i otpora na krilo, te raspored tlaka po površini krila.

Tablica 1: Rubni uvjeti za strujanje oko NACA009 krila sa pojavom kavitacije.

No.	Patch Name	Laminarno strujanje			Dodatak za turbulentno strujanje	
		$\mathbf{U}$ [m/s]	$\mathbf{p}$ [Pa,]	α_l [-]	$\mathbf{k}$ [m²/s²]	ω [1/s]
01	inlet	`fixedValue; uniform (U_ref);`	`zeroGradient;`	`fixedValue; uniform (α_ref 0 0);`	`fixedValue; uniform k_ref;`	`fixedValue; uniform ω_ref;`
02	outlet	`inletOutlet; uniform (0 0 0); uniform (U_ref 0 0);`	`fixedValue; uniform p_ref;`	`inletOutlet; uniform α_ref; uniform α_ref;`	`inletOutlet; uniform k_ref; uniform k_ref;`	`inletOutlet; uniform ω_ref; uniform ω_ref;`
03	foil	`fixedValue; uniform (0 0 0);`	`zeroGradient;`	`zeroGradient;`	`kqRWallFunction;`	`omegaWallFunction;`
04	up	`slip;`	`zeroGradient;`	`zeroGradient;`	`zeroGradient;`	`zeroGradient;`
05	down	`slip;`	`zeroGradient;`	`zeroGradient;`	`zeroGradient;`	`zeroGradient;`
06	frontBack	`empty;`	`empty;`	`empty;`	`empty;`	`empty;`

(NACA009 `interPhaseChangeFoam` rubni uvjeti)

Iz uvjeta se vidi da je zanemaren utjecaj zidova iznad i ispod krila. Također se može vidjeti da su struja tekućine definirana ulaznom brzinom tekućine u domenu, te hidrostatskim tlakom na izlasku iz domene, te je time osiguran kavitacijski koeficijent $\sigma_{cav} = 0.81$. U `interPhaseChangeFoam` implementaciji Shnerr-Sauer modela koristi se volumni udio kapljevite faze α_l umjesto parne faze, koji se lako izračuna iz jednadžbe

$$\alpha_l = 1 - \alpha.$$

Rubni uvjeti su postavljeni tako da u domenu ulazi tekućina u kapljevitom stanju, a tlak zasićenja je određen na 2300 Pa.

Za potrebe simulacije strujanja oko Delft krila (Slika 2), konstruirana je strukturirana 3D mreža sa 4,779,324 ćelija (Slika 3). Budući da je krilo simetričnog oblika, simuliran je protok fluida samo oko jedne polovice krila, a druga polovica krila je modelirana rubnim uvjetom simetrije.
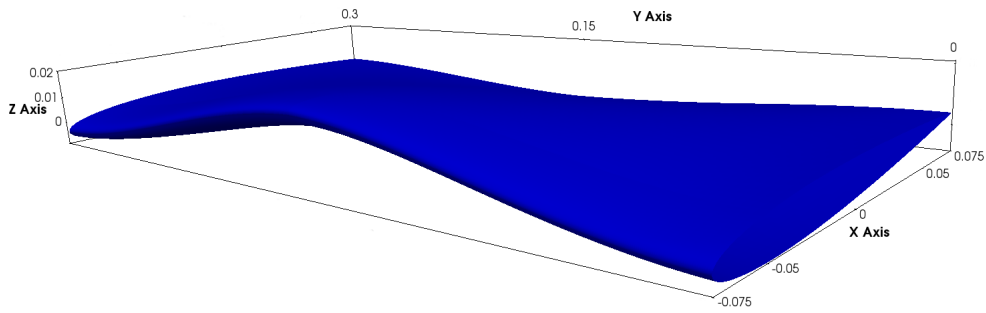
Slika 2: Delft Twist 11 krilo
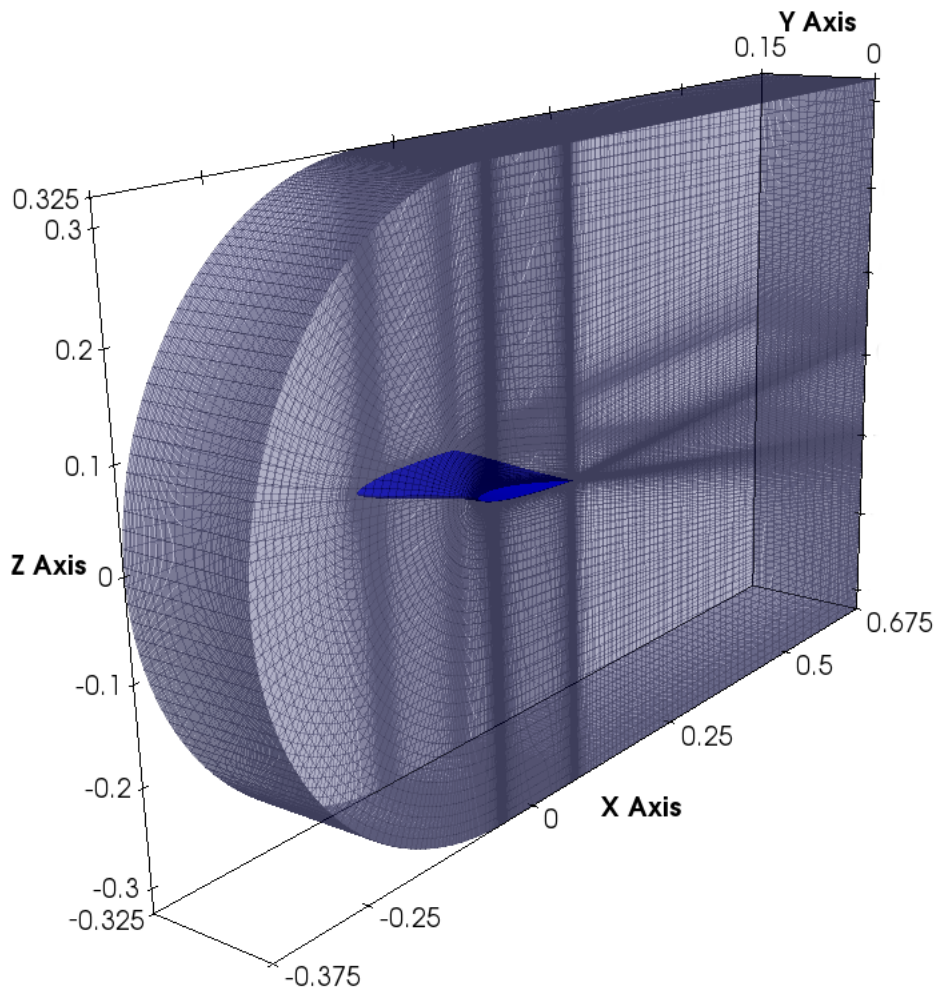
Slika 3: Računalna mreža oko Delft Twist 11 krila

.

Simulacije strujanja oko Delft krila provedene su analogno simulacijama ne NACA009 krilu, ali samo za jednu ulaznu brzinu fluida od 6.75 m/s. Za strujanje sa pojavom kavitacije postavljene su vrijednosti u skladu sa koeficijentom kavitacije $\sigma_{cav} = 1.17$.

Tablica 2: Rubni uvjeti za strujanje oko Delft Twist 11 krila sa pojavom kavitacije.

No.	Patch Name	Delft Twist 11 `interPhaseChangeFoam` rubni uvjeti				
		Laminarno strujanje			Dodatak za turbulentno strujanje	
		$\mathbf{U}$ [m/s]	$\mathbf{p}$ [Pa,]	α_l [-]	$\mathbf{k}$ [m²/s²]	ω [1/s]
01	inlet	fixedValue; uniform (U_ref);	zeroGradient;	fixedValue; uniform (α_{ref} 0 0);	fixedValue; uniform k_ref;	fixedValue; uniform ω_ref;
02	outlet	inletOutlet; uniform (0 0 0); uniform (U_ref 0 0);	fixedValue; uniform p_ref;	inletOutlet; uniform α_{ref}; uniform α_{ref};	inletOutlet; uniform k_ref; uniform k_ref;	inletOutlet; uniform ω_ref; uniform ω_ref;
03	foil	fixedValue; uniform (0 0 0);	zeroGradient;	zeroGradient;	kqRWallFunction;	omegaWallFunction;
04	up	slip;	zeroGradient;	zeroGradient;	zeroGradient;	zeroGradient;
05	down	slip;	zeroGradient;	zeroGradient;	zeroGradient;	zeroGradient;
06	side	slip;	zeroGradient;	zeroGradient;	zeroGradient;	zeroGradient;
07	symmetry	symmetry;	symmetry;	symmetry;	symmetry;	symmetry;

Postavke diskretizacije svojstava prikazane su u dodatku ovog rada.

Rezultati

NACA009

Za izvršavanje simulacija korišteno je više različitih računala. Informacije o trajanju simulacija može se vidjeti u tablici

Tablica 3: Vrijeme trajanja simulacija strujanja oko NACA009 krila sa pojavom kavitacije.

Informacije o NACA009 simulacijama					
Režim strujanja	Ulazna brzina [m/s]	Mikroprocesor	Simulirano vrijeme [s]	Prosječni vremenski korak [s]	Vrijeme trajanja izvršenja simulacije
Laminar	20	Intel(R) Core(TM)2 Quad CPU Q6600 @ 2.40GHz	0.15	$4 \cdot 10^{-6}$	44h 11' 55"
	30	Intel(R) Core(TM) i7-4820K CPU @ 3.70GHz	0.15	$2.5 \cdot 10^{-6}$	18h 13' 8"
Turbulent	20	Intel(R) Core(TM) i5-3570K CPU @ 3.40GHz	0.15	$4 \cdot 10^{-6}$	18h 13' 8"
	30	Intel(R) Core(TM)2 Quad CPU Q6600 @ 2.40GHz	0.15	$2.5 \cdot 10^{-6}$	91h 46' 49"

U svim simulacijama slučajeva kavitirajućeg strujanja, kavitacija je uspješno postignuta. Kako bi se lakše uspoređivali slučajevi strujanja, vrijednosti su usrednjene u vremenu.
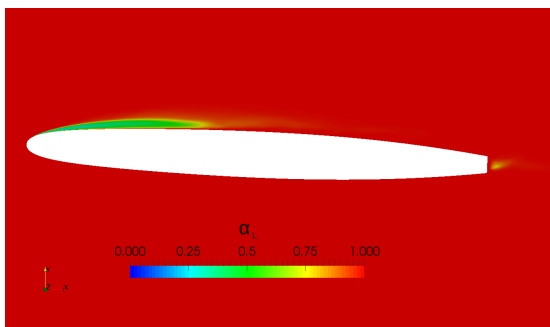
Slika 4: Prikaz srednje vrijednosti raspodjele parne faze u laminarnom strujanju oko NACA009 profila
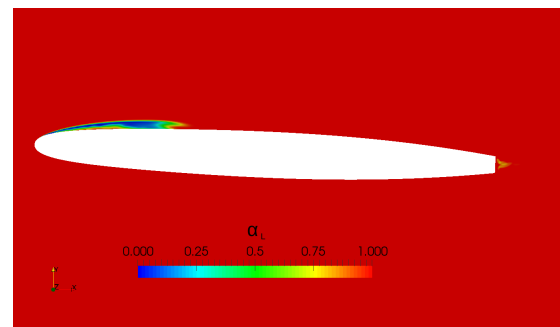
Slika 5: Prikaz srednje vrijednosti raspodjele parne faze u turbulentnom strujanju oko NACA009 profila

Može se primjetiti da slike prikazuju pojavu kavitacije oko nosa krila, te iza repa, što je u skladu sa očekivanjima. Kavitacija u turbulentnom strujanju je mnogo mirnija i teže dolazi do odvajanja parnog mjehura na nosu krila. Također, veća difuznost brzine u strujanju, brže razgrađuje parne mjehure koji se stvaraju. Tranzijentni prikaz kavitacije i odvajanja parnog mjehura, prikazan je u poglavlju 5. Obje slike kavitacije donekle odgovaraju eksperimentalnom istraživanju provedenom u [5], ali čini se da se ponašanje kavitacije u laminarnom strujanju bolje podudara sa stvarnim ponašanjem kavitacije.

Bolju usporedbu rezultata pruža prikaz raspodjele tlaka po krilu.
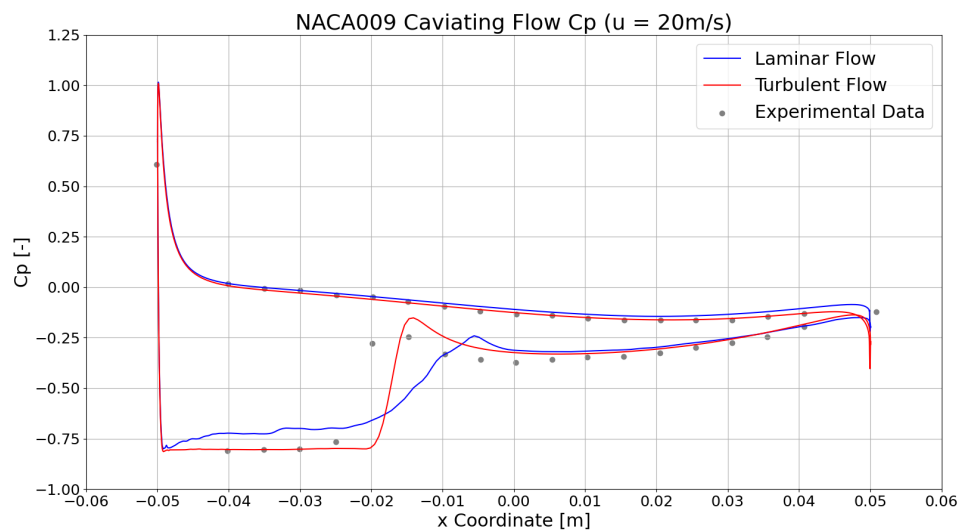
Slika 6: NACA009 C_P usporedba ($u = 20$ m/s)

Iz prikazane usporedbe C_P, izgleda da strujanje turbulencijom bolje prikazuje stvarnu raspodjelu tlaka po krilu iz [5]. Međutim za ulaznu brzinu $u = 30$ m/s slika je nešto drugačija.
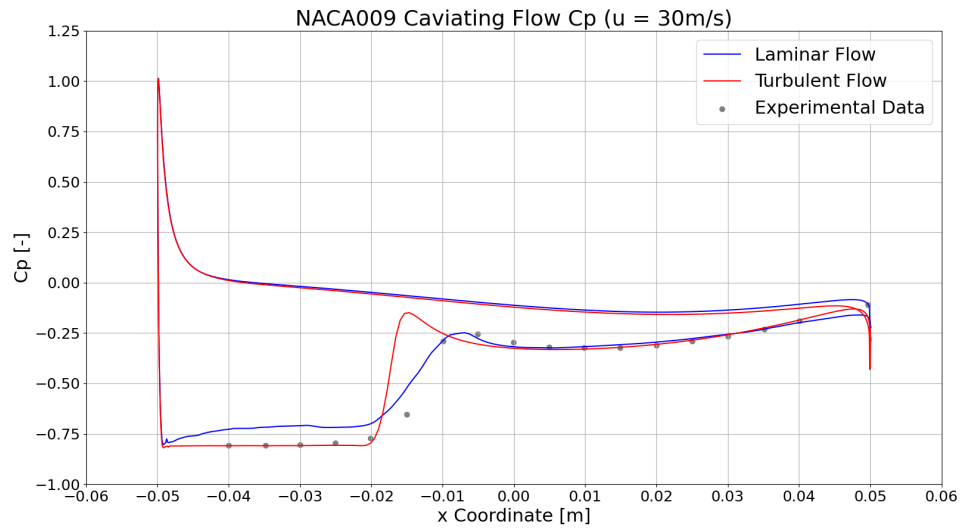
Slika 7: NACA009 C_P usporedba ($u = 30$ m/s)

Prema ovoj uspredbi, model strujanja bez turbulencije puno bolje odgovara stvarnoj slici kavitacije. Moguće je da do ovog razilaženja dolazi zbog samog usrednjavanja vrijednosti za tranzijentnu pojavu. Slike koje prikazuju silu uzgona pojašnjavaju ovaj problem.
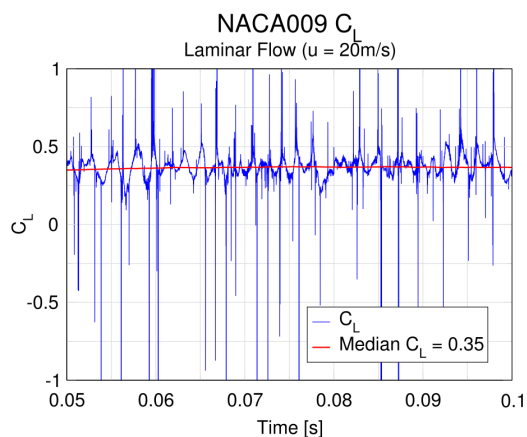
Slika 8: NACA009 laminarno strujanje C_L ($u = 20$ m/s)
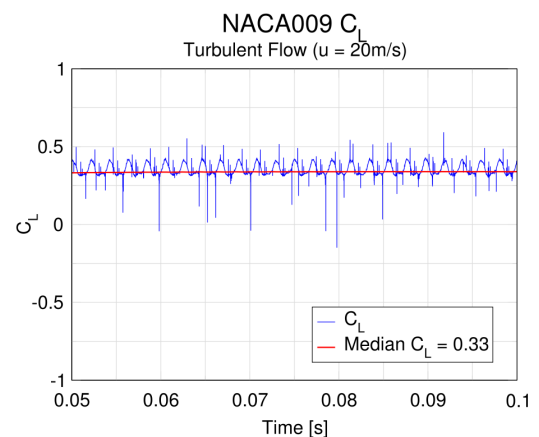
Slika 9: NACA009 turbulentno strujanje C_L ($u = 20$ m/s)

Iz slika se vidi da je ponašanje kavitacije u laminarnom strujanju vrlo nasumično, dok se ponašanje kavitacije u turbulentnom strujanju čini periodično. Kako je period strujanja koji se simulira vrlo malen, usrednjavanje ovako nasumičnog ponašanja možda prikazuje krive rezultate. Za brzinu strujanja od 30 m/s, slična je razlika u rezultatima sile uzgona.

Delft Twist 11

Kako bi se smanjilo vrijeme trajanja simulacija, mreža je podijeljena na više dijelova, te se proračun, pomoću funkcionalnosti višejezgrenih procesora, paralelno izvršavao na svim dijelovima mreže.

Tablica 4: Vrijeme trajanja simulacija strujanja oko Delft Twist 11 krila sa pojavom kavitacije.

Informacije o Delft Twist 11 simulacijama					
Režim strujanja	Mikroprocesor	Broj paralelnih procesa	Simulirano vrijeme [s]	Prosječni vremenski korak [s]	Vrijeme trajanja izvršenja simulacije
Laminar	Intel(R) Core(TM) i7-7800X CPU @ 3.50GHz	6	0.19	$6 \cdot 10^{-6}$	116h 42' 2"
Turbulent	Intel(R) Core(TM) i5-3570K CPU @ 3.40GHz	4	0.18	$4 \cdot 10^{-6}$	291h 43' 17"

U simulacijama kavitirajućeg strujanja oko Delft krila, također je uspješno ostvarena kavitacija. Ekvivalentno strujanju oko NACA009 krila, vrijednosti su usrednjene u vremenu. Za usporedbu, prikazan je središnji presjek.
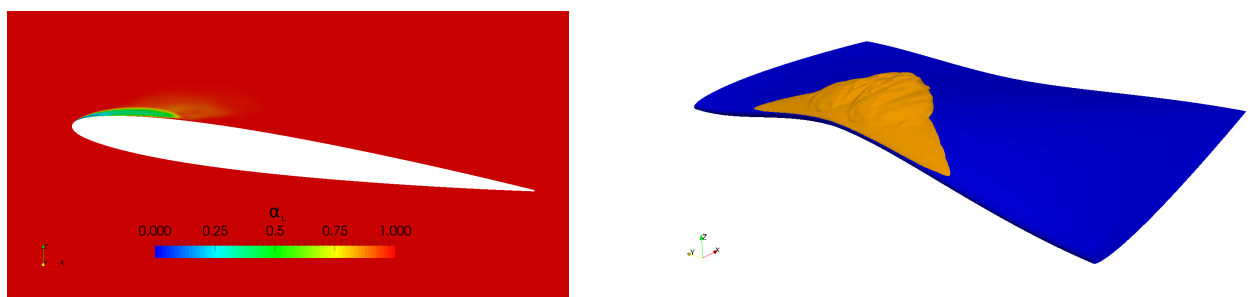
Slika 10: Prikaz srednje vrijednosti raspodjele parne faze u laminarnom strujanju oko Delft Twist 11 krila

.
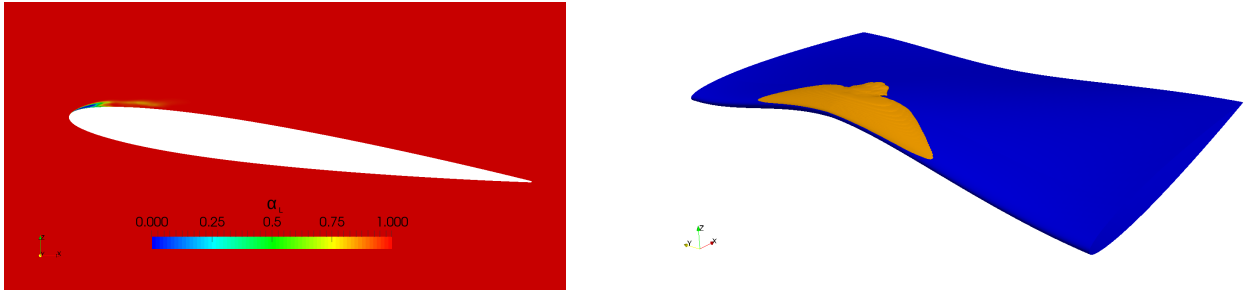
Slika 11: Prikaz srednje vrijednosti raspodjele parne faze u turbulentnom strujanju oko Delft Twist 11 krila

.

Ponovo se može primjetiti da turbulencija umiruje ponašanje kavitacije. U slučaju kavitirajućeg strujanja sa turbulencijom, primarni parni mjehur ostaje bliže krilu, te se odvojeni mjehuri brzo raspadaju u struji fluida. Tranzijentni prikaz kavtacije puno bolje oslikava ovaj fenomen i opisan je u poglavlju 5. Uspoređujući rezultate sa slikama kavitacije iz [6], primjećuju se sličnosti u strukturama parnih mjehura, te načinu odvajanje manjih mjehura. Međutim slike ne odgovaraju u potpunosti. Kao i u slučaju NACA009 kavitirajućeg strujanja, slike laminarnog strujanja bolje odgovaraju ponašanju kavitacije u eksperimentalnim mjerenjima.

Ove simulacije uspoređivane su sa eksperimentalnim rezultatima iz [7] i [9], na temelju sile uzgona na krilo.
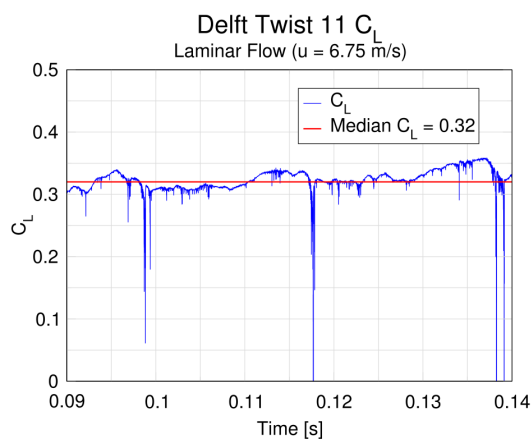
Slika 12: Delft Twist 11 laminarno strujanje C_L
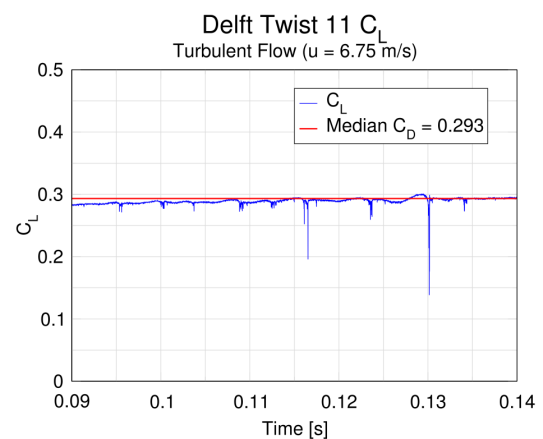
Slika 13: Delft Twist 11 turbulentno strujanje C_L

Vidljivo je da je ponašanje sile uzgona u 3D strujanju puno pravilnije nego u 2D strujanju. Laminarno strujanje bolje prikazuje stohastičnu prirodu kavitacije, ali možda prikazuje pretjerano jake implozije parnih mjehura. Uz to može se primjetiti da slike prikazuju kako srednja vrijednost sile uzgona zapravo raste. Jedna od mogućnosti za to je da je period strujanja koji se u simulacijama uzimao u obzir previše kratak, te bi možda sa duljim periodom došlo do kvalitetnijeg prikaza kavitacije.

Uspoređujući srednje vrijednosti sile uzgona sa drugim mjerenjima vidi se da je drastično podcijenjena sila.

Tablica 5: Vrijednosti koeficijenta uzgona za Delft Twist 11 iz [7] i [9]

Delft Twist 11 C_L	
Experimental [7]	0.53
LES [7]	0.45
RANS $k - \omega$ SST with correction [9]	0.43
Laminar Flow Simulation	0.32
Turbulent Flow Simulation	0.293

Zaključak

Rezltati rada prikazuju da modeli kavitirajućeg strujanja bez utjecaja turbulencije bolje oslikavaju stvarno ponašanje kavitacije, ali možda prikazuju preveliki utjecaj implozija. Uz to se i mora uzeti u obzir da simulacija strujanja, prikazana u ovom radu, bez modeliranja turbulencije nije fizikalna, jer Reynoldsov broj pokazuje da se strujanja nalazi u turbulentnom režimu. S druge strane turbulencija, u kavitirajućim strujanjima, ubija nasumično ponašanje kavitacije i podcjenjuje razvoj odvojenih parnih mjehura. Osrednjavanje vrijednosti i mogući prekratak simulirani period strujanja također dovode u pitanje točnost rezultata. Za daljne istraživanje, predlaže se modifikacija modela turbulencije i uzimanje u obzir duljeg perioda simulacije strujanja.

1 | Introduction

Cavitation is the occurence of vapor, in the form of a cavitation bubble, within a flow of liquid, due to low local pressure, which is generated by high local flow velocities. There are several ways to arrive at the transition of a liquid into vapor, the most common being cooking. However, during cooking, the transition occurs due to the change in temperature. Since the temperature of the fluid and the vapor saturation pressure are linked, this may seem arbitrary. Nonetheless, the term cavitation is generally reserved for the conditions in which the temperature of the bulk fluid, does not change and the cavitation gas appears due to the local drop in pressure below the vapor saturation pressure of the liquid for a given temperature.

The adverse effects of cavitation are noise, vibrations, erosion and disruption of the flow, which, in case of flows around hydrofoils or similar surfaces, result in loss of lift and increase of drag. Vaporization and condensation are very fast processes, especially compared to the dynamics of vapor cavities. Since these vapor cavities are part of the flow, they can be quickly transferred from low pressure areas, to high pressure areas, where they implode. During this collapse, local fluid velocities can exceed the speed of sound, for the local flow conditions, and shock waves occur. The consequence is that cavitation is very noisy and radiates noise over a wide range of frequencies. Also, the local pressure rises rapidly, leading to damage of a nearby surface, which causes erosion. If large ammounts of vapor are present, the implosion can cause pressure variations in the fluid, which can cause large scale vibrations in the mechanical structure. The majority of the adverse effects of cavitation can be attributed to erosion, noise and vibrations [3].

Additionally, cavitation may alter the fluid flow. This can cause sub-optimal flow conditions around propellers for example, resulting in thrust reduction of the propeller. In the case of valves, cavitation may choke the flow.

1.1.   Types of Cavitation

There are different classifications of cavitation. Here cavitation will be separated into three main types. The first type of cavitation is called Bubble Cavitation, shown in Fig. 1.1. The fluid evaporates into separate vapor bubbles which travel with the flow, until they reach a high pressure area where they collapse. The bubbles are not uniform and each bubble affects another so the phenomenon is somewhat random.
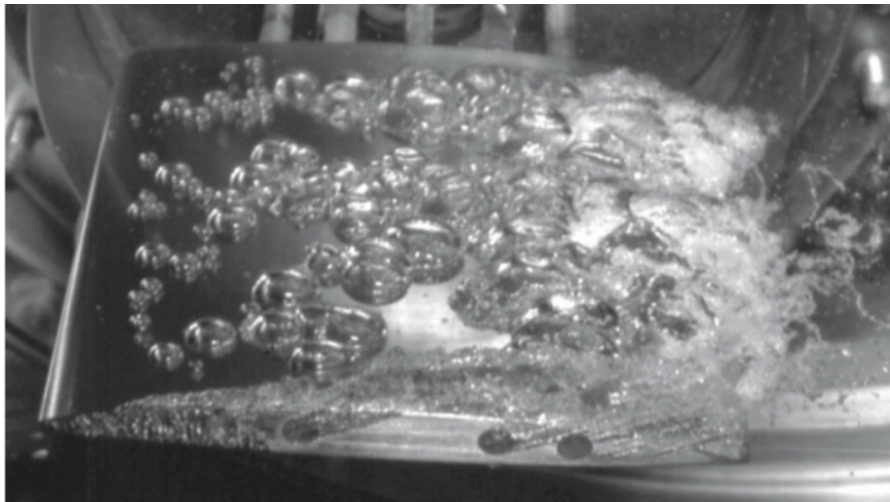
Figure 1.1: Travelling Bubble Cavitation [1].

The second type of cavitation is Sheet Cavitation, Fig. 1.2. This type of cavitation occurs at a surface immersed in the flow. It is a region of vapor which remains approximately at the same position relative to the surface. In this way it seems attached to the surface. At random intervals, parts of the large vapor cavity detach and travel downstream. This is due to the backflow because of the low pressure region. The occurrence is of a very stochastic nature. It is usually impossible to determine the size of the detached cavity or the moment of detachment.
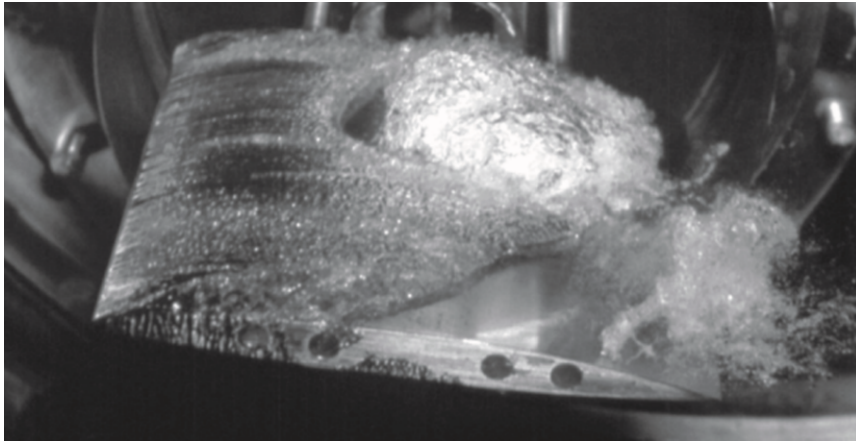
Figure 1.2: Shedding of a Sheet Cavitation [1].

The last type of cavitation is Vortex Cavitation, shown in Fig. 1.3. The fluid cavitates in the core of a vortex, where low pressure zones occur. Vortices are common on rotating machines, like turbines or propellers. Two distinct types of vortices are formed. The first manifests itself on the tips of the blades, where fluid tends to flow over the blade from the high pressure side to the low pressure side. The other vortex forms simply from the fluid passing through the machine, so the core of the of the vortex is aligned with the rotation axis of the machine. Vortex cavitation commonly doesn't erode the machines, but it does cause noise and it disrupts the flow.
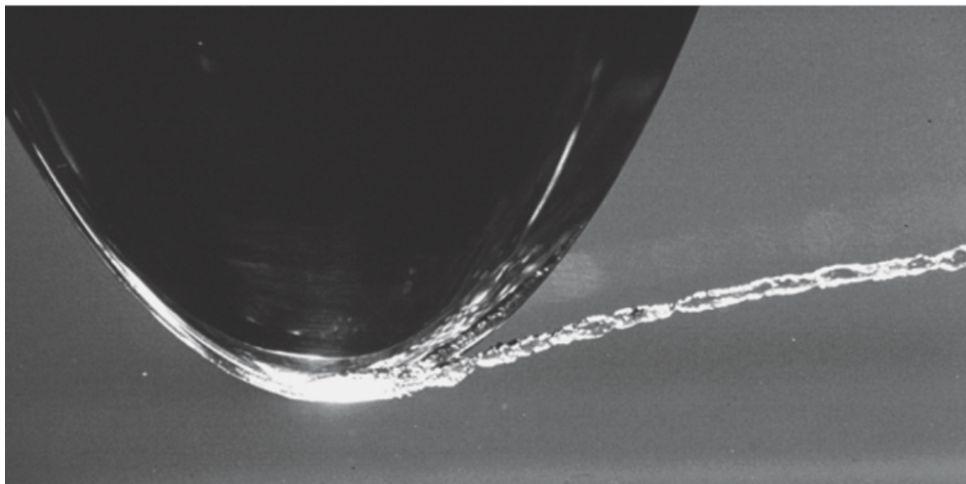
Figure 1.3: Blade Tip Vortex Cavitation [1].

Lastly, in some cases, multiple cavitation types may occur in the same flow.

1.2. Scope of Thesis

This thesis will attempt to examine and validate models for cavitation in Computational Fluid Dynamics (CFD). First, description of the physics of vapor cavities and an overview of of current CFD cavitation models, will be given. Afterwards, several simulations will be performed, in `foam-extend` and `OpenFOAM`, on a 2-D NACA0009 Hydrofoil, and a 3-D Delft Hydrofoil and the results will be compared against experimental results.

1.3. Thesis Outline

This thesis is organised in six Chapters, as follows: Chapter 1 offers an overview of cavitation and serves as an introduction to the thesis. Chapter 2 introduces the basic notions of the Finite Volume Method, used for CFD simulations. Chapter 3 introduces the mathematical models for cavitation and their implementation in CFD. Chapter 4 defines the different geometries used, listing the corresponding boundary conditions. Chapter 5 presents the results of CFD simulations both graphically and numerically, offering appropriate comments and explanations where needed. Chapter 6 serves as the conclusion of the thesis.

2 | Finite Volume Method

2.1. Introduction

The previous chapter introduced the cavitation phenomenon and outlined the theme of the thesis.

The following chapter will introduce the Finite Volume Method, which serves as a basis for CFD analysis. The chapter will focus on describing the basic equations which are used and their discretisation using Finite Volume Method.

2.2. Definition

The Finite Volume Method (FVM) is a numerical technique that transforms the partial differential equations representing conservation laws over differential volumes into discrete algebraic equations over finite volumes (or elements or cells) [10]. The first step in aquiring a solution with this process is the discretisation of the geometric domain, which is done by dividing the space into non-overlapping elements of finite volumes. The partial differential equations are then integrated over each element and transformed into algebraic equations. Finally, the system of algebraic equations is solved to compute the values of the variable of interest in each volume.

2.3. The Scalar Transport Equation

The basic equation used in FVM is the Scalar Transport Equation. The first part of this equation is derived when the Reynolds Transport Theorem (RTT) is applied to a

finite volume. The RTT describes the rate of change of a general property ϕ in a region (control volume, CV) as shown in Fig. 2.1:
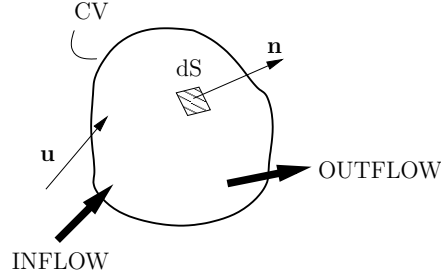
Figure 2.1: Closed system or Control Volume (CV) [2].

The rate of change is affected by the inflow and outflow of the property in the CV, and by the change of the property ϕ inside the CV. This equation can be written as:

$$\frac{\mathrm{d}}{\mathrm{d}t}\int_{V_m}\phi\,dV = \int_{V_m}\frac{\partial\phi}{\partial t}\,dV + \oint_{S_m}\phi(\mathbf{n}\bullet\mathbf{u})dS\,. \tag{2.1}$$

Using the Gauss' Theorem Eq. 2.2 the surface integral can be transformed into a volume integral and Eq. 2.1 can be transformed into Eq. 2.3

$$\int_{V_P}\nabla\cdot\mathbf{a}\,dV = \oint_{\partial V_P}d\mathbf{s}\bullet\mathbf{a} = \oint_{\partial V_P}d\mathbf{n}\bullet\mathbf{a}\,dS\,. \tag{2.2}$$

$$\frac{d}{dt}\int_V\phi\,dV = \int_V\left[\frac{\partial\phi}{\partial t} + \nabla\cdot(\phi\mathbf{u})\right]dV\,, \tag{2.3}$$

which is used to model the convective transport of a general property ϕ.

The surface and volume sources of the general property ϕ also contribute to the change of ϕ inside the CV. This contribution is written as:

$$\frac{d}{dt}\int_V\phi\,dV = \int_V q_v\,dV - \oint_S(\mathbf{n}\bullet\mathbf{q}_s)dS\,. \tag{2.4}$$

Again, using the Gauss' Theorem, the surface source term can be transformed into a volume integral. Inserting Eq. 2.4 into Eq. 2.3, and integrating over the CV ($V = const.$), the following equation is obtained:

$$\frac{\partial \phi}{\partial t} + \nabla \cdot (\phi \mathbf{u}) = q_v - \nabla \cdot \mathbf{q}_s \,. \tag{2.5}$$

The surface source term is modeled using Diffusive Transport. It is based on the observation that a general property ϕ will be transported from an area of greater concentration, to an area of lower concentration. This is modeled using the negative value of the gradient of ϕ, $\nabla\phi$ and the diffusivity coefficient γ [11]:

$$\mathbf{q}_s = -\gamma \, \nabla\phi \,. \tag{2.6}$$

Finally, by inserting Eq. 2.6 into Eq. 2.5 and rearranging, the general form of the Scalar Transport Equation is obtained:

$$\underbrace{\frac{\partial \phi}{\partial t}}_{\text{temporal derivative}} + \underbrace{\nabla \cdot (\phi \mathbf{u})}_{\text{convection term}} - \underbrace{\nabla \cdot (\gamma \nabla \phi)}_{\text{diffusion term}} = \underbrace{q_v}_{\text{source term}} \,. \tag{2.7}$$

The temporal term in the equation, represents the inertia of the system. The convective term represents the transport of the property ϕ using the mass flow, and therefore depends on the flow velocity $\mathbf{u}$. The diffusive term represents the transport of ϕ dependant on the gradient of ϕ. And lastly, the source term defines the local production and/or destrucion of ϕ.

2.3.1. Conservation Laws

By inserting properties of interest into the general Scalar Transport Equation Eq. 2.7, The Laws of Conservation, which govern all fluid flows, are obtained.

Conservation of Mass

By replacing the general property ϕ with fluid density ρ and by defining a zero source term, an equation, describing the Conservation of Mass is obtained:

$$\frac{\partial \rho}{\partial t} + \nabla \cdot (\rho \mathbf{u}) = 0 \,. \tag{2.8}$$

This equation can be further simplified for incompressible flow $\rho = const$.

$$\nabla \cdot \mathbf{u} = 0 \,. \tag{2.9}$$

Conservation of Linear Momentum

The equation for the Conservation of Linear Momentum can be obtained by inserting the linear momentum vector $\boldsymbol{\rho}\mathbf{u}$ into Eq. 2.7.

$$\frac{\partial (\rho \mathbf{u})}{\partial t} + \nabla \cdot (\rho \mathbf{u}\mathbf{u}) = \underbrace{\rho \mathbf{g}}_{\text{gravitational force}} + \underbrace{\nabla \cdot \boldsymbol{\sigma}}_{\text{surface forces}} \,. \tag{2.10}$$

If the flow is incompressible, and the gravitational force term is diregarded, Eq. 2.10 can be written as follows:

$$\underbrace{\frac{\partial \mathbf{u}}{\partial t}}_{\text{local production}} + \underbrace{\nabla \cdot (\mathbf{u}\mathbf{u})}_{\text{convection}} - \underbrace{\nabla \cdot (\nu_{\text{eff}} \nabla \mathbf{u})}_{\text{diffusion}} = - \underbrace{\frac{1}{\rho} \nabla p}_{\text{pressure gradinet}} \,, \tag{2.11}$$

Two characteristics can be observed. Firstly, in the convection term the velocity $\mathbf{u}$ is both the transported and the transporting velocity, which makes the equation non-linear [11]. And secondly, the diffusion term represents the fluid viscosity, and the diffusivity coefficient is in fact the viscosity coefficient of the fluid ν_{eff}.

Conservation of Energy

If the general property ϕ in Eq. 2.7 is replaced by specific internal energy ρe, and the source term is made equal to the sum of the power of the forces acting on the CV, and the net heat flux is modeled using the specific heat flux $\mathbf{q}$ and the volumetric heat source Q as seen in Fig. 2.1, the equation for the Conservation of Energy is obtained.

$$\frac{\partial (\rho e)}{\partial t} + \nabla \cdot (\rho e \mathbf{u}) = \underbrace{\rho \mathbf{g}\boldsymbol{\cdot}\mathbf{u}}_{\text{power of gravity force}} + \underbrace{\nabla \cdot (\boldsymbol{\sigma}\boldsymbol{\cdot}\mathbf{u})}_{\text{power of surface forces}} - \underbrace{\nabla \cdot \mathbf{q} + \rho Q}_{\text{net heat flux}} \,. \tag{2.12}$$

2.4.   Discretisation

The process of converting the governing equation into a set of algebraic equations for the discrete values of ϕ, is called the discretisation process, and the specific methods employed for this conversion are called the discretisation methods. The focus is to replace the continuous exact solution of the partial differential equations with discrete values of the general property ϕ at specified points in the computational domain[10]. It should be noted that each step in the process of discretisation simplifies the equations, and thereby causes the solution of the set of algebraic equations to differ from the true solution of the partial differential equations.

The computational domain is a geometric representation of space, in which the change of the general property ϕ is observed. This space is divided into a finite number of non-overlapping control volumes or cells, in which the governing equations for ϕ are defined. This division is called Space Discretisation. A computational domain that is dicretized is called a mesh, and the discretisation of space, in CFD, is also called meshing.

A cell can be any convex polyhedron as seen on Fig. 2.2, however in most cases the mesh is made from tetrahedrons, hexahedrons and convex dodecahedrons.

The cell centroid P and the centroid position vector $\mathbf{r}_P$ define a polyhedral cell of volume V_P. For a selected face f, a surface normal vector $\mathbf{s}_f$ is defined with a magnitude equal to the area of the selected face S_f. Point N represents the centroid of a neighbouring cell, and the centroids are connected by the delta vector $\mathbf{d}_f = \overline{PN}$ [11].

The cell centroid P is defined as the centre of the Control Volume and is given by the following equation:

$$\int_{V_P} (\mathbf{x} - \mathbf{x}_P)\, dV = \mathbf{0}\,, \tag{2.13}$$

The face centre f is defined in a similair manner:

$$\int_{S_f} (\mathbf{x} - \mathbf{x}_f)\, dS = \mathbf{0}\,. \tag{2.14}$$
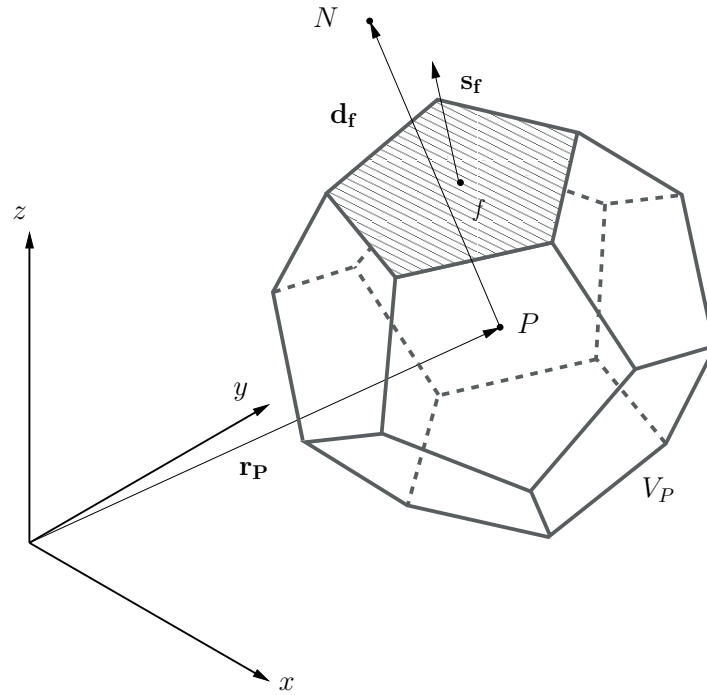
Figure 2.2: Polyhedral finite volume[2].

The surface normal vector $\mathbf{s}_f$ has a magnitude defined by the area of the surface, and is thereby given as:

$$\mathbf{s}_f = \int_{S_f} \mathbf{n}\, dS\,. \tag{2.15}$$

2.4.1. Spatial Variation

The variation of the property ϕ inside the cell can be approximated as linear. The property ϕ at the cell centroid P is given as ϕ_P, while the vector pointing to P is x_P, then the value of property ϕ at any point in the cell is defined as:

$$\phi(t + \Delta t) = \phi^t + \Delta t \left(\frac{\partial \phi}{\partial t}\right)^t\,. \tag{2.16}$$

This approximation is of a second order of accuracy.

Using Eq. 2.17, a volume integral can be formulated as follows:

$$\begin{aligned}
\int_V \phi \, dV &= \int_V \left[\phi_P + (\mathbf{x} - \mathbf{x}_P)\bullet(\nabla\phi)_P\right] dV \\
&= \phi_P \int_V dV + (\nabla\phi)_P\bullet \int_V (\mathbf{x} - \mathbf{x}_P) dV \\
&= \phi_P V_P \, ,
\end{aligned} \tag{2.17}$$

and the surface integral can be evaluated as:

$$\begin{aligned}
\oint_S \mathbf{n}\, \phi \, dS &= \sum_f \int_{S_f} \mathbf{n}\phi_f \, dS_f \\
&= \sum_f \int_{S_f} \mathbf{n}[\phi_f + (\mathbf{x} - \mathbf{x}_f)\bullet(\nabla\phi)_f] \, dS_f \\
&= \sum_f \mathbf{s}_f \phi_f \, .
\end{aligned} \tag{2.18}$$

If the process that is being observed is transient, meaning that ϕ is time dependent, discretisation of time is required. This is achieved by simply dividing the time interval into a series of time steps Δt. The time steps can differ in size, however they can influence the stability of the solution process. This effect is determined by the Courant number, and is described in [10].

2.4.2. Scalar Transport Equation Discretisation

The discretization of the Scalar Transport Equation is performed term by term, starting from the integral form of the equation:

$$\int_V \frac{\partial \phi}{\partial t} \, dV + \oint_S \phi\,(\mathbf{n}\bullet\mathbf{u})\, dS - \oint_S \gamma\,(\mathbf{n}\bullet\nabla\phi)\, dS = \int_V Q_v \, dV \, , \tag{2.19}$$

Temporal Derivative Discretisation

This term represents the change of ϕ inside the CV in regard to time. The simplest method of discretisation is written as:

$$\frac{\partial \phi}{\partial t} = \frac{\phi^n - \phi^o}{\Delta t} \,.$$ (2.20)

This method takes into account only values of ϕ at two time steps, and is of first order accuracy.

- The field value of variable ϕ after the time step at time t_{new}

$$\phi^n = \phi(t = t_{new}) \,.$$ (2.21)

- The field value of variable ϕ before the time-step, at time t_{old}:

$$\phi^o = \phi(t = t_{old}) \,.$$ (2.22)

- The time-step size Δt is defined as:

$$\Delta t = t_{new} - t_{old} \,.$$ (2.23)

By increasing the number of time steps that are considered, the accuracy can be increased. An example of a method that is of second order accuracy is a backward differencing scheme. This method includes a time step before t_{old} and is written as:

$$\frac{\frac{3}{2}\phi^n - 2\phi^o + \frac{1}{2}\phi^{oo}}{\Delta t} \,,$$ (2.24)

where the term ϕ^{oo} is expressed as $\phi^{oo} = \phi(t_{new} - 2\Delta t)$ and the time-step size is kept constant.

The spatial variation of ϕ inside CV was shown as linear in Eq. 2.17, and implemented together with Eq. 2.20, an equation is formulated:

$$\int_V \frac{\partial \phi}{\partial t}\, dV = \frac{\phi^n - \phi^o}{\Delta t} V_P \,, \tag{2.25}$$

where the change of ϕ is defined as the difference between the value ϕ in the center of the CV at time t_{new} and the value of ϕ at time t_{old}, divided by the size of the time-step Δt.

Discretisation of the Convection Term

The Gauss' Theorem Eq. 2.2 is implemented on the convection term from Eq. 2.19, to transform the volume integral into a surface integral:

$$\int_V \nabla \cdot (\phi \mathbf{u})\, dV = \oint_S \phi(\mathbf{n} \bullet \mathbf{u}) dS \,. \tag{2.26}$$

By applying the linear surface variation discretisation from Eq. 2.22, the Eq. 2.26 is transformed into a sum of surface integrals:

$$\oint_S \phi(\mathbf{n} \bullet \mathbf{u}) dS = \sum_f \phi_f (\mathbf{s}_f \bullet \mathbf{u}_f) = \sum_f F\, \phi_f \,, \tag{2.27}$$

where ϕ_f represents the value of ϕ at the centre of the cell face, and the flux F can be expressed as a product of the surface normal vector and the convective velocity $\mathbf{u}_f$:

$$F = \mathbf{s}_f \bullet \mathbf{u}_f \,. \tag{2.28}$$

The value ϕ_f must be calculated. It can be evaluated from ϕ_P and ϕ_N, using one of many different interpolation schemes, eg:

- Central differencing

$$\phi_f = f_x \phi_P + (1 - f_x)\phi_N \,, \tag{2.29}$$

 The value is calculated based on the distance of the surface f from the centers of the CVs. This method is of second order accuracy.

- Upwind differencing

$$\phi_f = max(F, 0)\,\phi_P + max(-F, 0)\,\phi_N\,. \tag{2.30}$$

The value of ϕ_f is completely defined by the flux value and the value of ϕ in the cell that is located upstream in the flow.

Discretisation of the Diffusion Term

The diffusion term is also transormed using the Gauss' Theorem and can be discretized using the same linear method as was used for the covection term:

$$
\begin{aligned}
\int_V \nabla \cdot (\gamma \nabla \phi)\ dV &= \oint_S \gamma(\mathbf{n} \cdot \nabla \phi) dS \\
&= \sum_f \int_{S_f} \gamma(\mathbf{n} \cdot \nabla \phi)\ dS \\
&= \sum_f \gamma_f\, \mathbf{s}_f \cdot (\nabla \phi)_f\,.
\end{aligned}
\tag{2.31}
$$

The gradient ϕ_f, at the surface f, can be approximated as the difference between the values of the ϕ at centre of the neighbouring cells ϕ_N and ϕ_P, divided by the distance between the cell centres:

$$\mathbf{s}_f \cdot (\nabla \phi)_f = |\mathbf{s}_f| \frac{\phi_N - \phi_P}{|\mathbf{d}_f|}\,. \tag{2.32}$$

Discretisation of the Source/Sink Term

Sources and sinks describe local effects and may be modelled by a function of space and time, or any complex variable S. Again, if the linear spatial variation discretization Eq. 2.20 is applied, the term can be written as:

$$\int_V S\, dV = SV_P\,, \tag{2.33}$$

where S is the value of the source term at the centre of the CV.

2.5. Linear System of Equations

After the process of discretisation, a linear equation for the property ϕ, at every cell centroid P, is aquired. A general form of the linear equation, whereby the term ϕ is replaced by x, is given by:

$$a_P x_P + \sum_N a_N x_N = b \,. \tag{2.34}$$

Since the value of ϕ is dependant on the value in the neghbouring cells N, a system of equations can be formulated. This system is usually written as a matrix:

$$[A][x] = [b] \,. \tag{2.35}$$

The matrix $[A]$ contains the coefficients a_P and a_N, the vector $[x]$ contains the values of x in the cell centroids P, and the vector $[b]$ represents the right-hand side, or other contributions to the equation. The matrix $[A]$ is a square matrix of size $N \times N$, where N is the number of cells. However, most of the coeffecents in the matrix are equal to zero, since the differencing schemes determine how many cells influence the value of x_P, and most of them take only neighbouring cells into account.

2.6. Boundary Conditions

Boundary conditions are used to represent the environment outside the computational domain. They assign behavior to the property ϕ at cell faces that bound the computational domain. The type and postion of the boundary conditions are dependant upon the physics of the phenomenon which is being studied. Numerical boundary conditions that are most frequently used in CFD include:

- The *Dirichlet* boundary, defines a fixed value of ϕ at the boundary

$$\phi = const. \tag{2.36}$$

- The *Neumann* boundary condition, which prescribes a fixed gradient or fixed flux at the boundary

$$\mathbf{n} \cdot \mathbf{q}_s = q_b \,. \tag{2.37}$$

- Geometric and Coupled boundary conditions, such as symmetry, cyclic or periodic boundary conditions

2.7.   Pressure-Velocity Coupling Algorithms

The set of equations, Eq. 2.11 and 2.9, which represent the Navier-Stokes equations for incompressible flow, correspond to one vector field governed by one vector equation and one scalar field governed by a scalar equation. It can be observed that these equations are coupled, since the velocity appears in both equations. Since the pressure gradient is present in the momentum equation, a linear coupling between the pressure and the velocity is formed. The pressure field is a scalar field, while the velocity is a vector filed, so in order for the two to be put into relation, a derivation of the pressure equation is needed. This can be achieved by discretising the momentum equation as follows:

$$a_P^{\mathbf{u}}\mathbf{u}_P + \sum_N a_N^{\mathbf{u}}\mathbf{u}_N = \mathbf{r} - \nabla p \,. \tag{2.38}$$

The off-diagonal part of the matrix and the right-hand-side contributions are combined in the operator $\mathbf{H}(\mathbf{u})$:

$$\mathbf{H}(\mathbf{u}) = \mathbf{r} - \sum_N a_N^{\mathbf{u}}\mathbf{u}_N \,. \tag{2.39}$$

The equation in Eq. 2.38 can be transformed into:

$$a_P^{\mathbf{u}}\mathbf{u}_P = \mathbf{H}(\mathbf{u}) - \nabla p \,, \tag{2.40}$$

and rearranged into:

$$\mathbf{u}_P = (a_P^{\mathbf{u}})^{-1}(\mathbf{H}(\mathbf{u}) - \nabla p) \,. \tag{2.41}$$

By inserting Eq. 2.41 into Eq. 2.9, a pressure equation for incompressible flow is formed as:

$$\nabla \cdot \left[(a_P^{\mathbf{u}})^{-1} \nabla p \right] = \nabla \cdot ((a_P^{\mathbf{u}})^{-1} \mathbf{H}(\mathbf{u})). \tag{2.42}$$

Now that the pressure-velocity coupling is established, an algorithm for solving the equations can be introduced. For the purpose of this thesis, the SIMPLE, PISO and PIMPLE algorithms will be explained, since they are present in the cases that will be studied.

2.7.1.   SIMPLE Algorithm

The Semi-Implicit Algorithm for Pressure-Linked Equations (SIMPLE), is the earliest pressure-velocity coupling algorithm used [12]. The SIMPLE algorithm is, in [11], described as:

1. Initial guess of the pressure field p^*.

2. The Momentum Predictor step: Momentum equation is solved using the guessed pressure.
$$a_P^{\mathbf{u}} \mathbf{u}_P = \mathbf{H}(\mathbf{u}) - \nabla p^*. \tag{2.43}$$

3. The Pressure Correction Step: New pressure calculation based on the velocity field
$$\nabla \cdot \left[(a_P^{\mathbf{u}})^{-1} \nabla p \right] = \nabla \cdot ((a_P^{\mathbf{u}})^{-1} \mathbf{H}(\mathbf{u})). \tag{2.44}$$

4. Conservative face flux F assembly based on the pressure solution
$$F = \mathbf{s}_f \boldsymbol{.} \mathbf{H}(\mathbf{u}) - a_N^p (p_N - p_P). \tag{2.45}$$

5. Repeat until convergence is reached.

In order to ensure the stability of the algorithm, under-relaxation of the equations is introduced, whereby the new values are paritally constructed from the old values, from the previous time-step, and partially from the newly calculated values. As a consequence, the algorithm takes more steps to converge to a solution, but is more stable.

$$p^{**} = p^* + \alpha_P(p - p^*)\,, \tag{2.46}$$

$$\mathbf{u}^{**} = \mathbf{u}^* + \alpha_U(\mathbf{u} - \mathbf{u}^*), \tag{2.47}$$

The following constraints for the relaxation coefficients are apllied:

$$
\begin{aligned}
0 &< \alpha_P \leq 1\,, \\
0 &< \alpha_U \leq 1\,, \\
\alpha_P &+ \alpha_U \approx 1\,.
\end{aligned} \tag{2.48}
$$

2.7.2.   PISO Algorithm

The Pressure-Implicit algorithm with Splitting of Operators (PISO) is an extension of the basic SIMPLE algorithm using one predictor and two corrector steps [13].

1. The pressure field p^* from previous corrector or time-step is used, with the conservative fluxes corresponding to p^* also being available.

2. The momentum equation is discretised using the available flux field.

3. The Momentum Predictor step: Momentum equation is solved using the guessed pressure
$$a_P^{\mathbf{u}}\mathbf{u}_P = \mathbf{H}(\mathbf{u}) - \nabla p^*.$$

4. The Pressure Correction Step: New pressure calculation based on the velocity field
$$\nabla \cdot \left[(a_P^{\mathbf{u}})^{-1}\nabla p\right] = \nabla \cdot ((a_P^{\mathbf{u}})^{-1}\mathbf{H}(\mathbf{u})).$$

5. Conservative face flux F assembly based on the pressure solution
$$F = \mathbf{s}_f \boldsymbol{\cdot} \mathbf{H}(\mathbf{u}) - a_N^p(p_N - p_P).$$

6. Cell-centred velocity field is updated explicitly with the assembled momentum coefficients
$$\mathbf{u}_P = (a_P^{\mathbf{u}})^{-1}(\mathbf{H}(\mathbf{u}) - \nabla p).$$

7. If convergence is not reached, repeat from the pressure correction step.

8. Repeat sequence using a new time-step

The PISO algorithm is mainly used when the simulation time-step is controlled by physical constraints and where temporal accuracy is important, i.e. Large Eddy Simulation [11].

2.7.3.   PIMPLE ALgorithm

The PIMPLE algorithm is a combination of the SIMPLE and PISO algorithms. It allows for large Courant numbers, or large time-step sizes, and is therefore frequently used for transient problems. The algorithm searches for the correct steady state solution for each time-step using under-relaxation [14]. Outer corrector loops are used to ensure convergence inside a time-step loop. When the defined tolerance criterion for the steady-state solution is reached, the outer correction loop is ended and the algorithm moves on to the next time-step.

2.8.   Turbulence Modelling

The occurence of turbulence in nature presents a difficult problem. The stochastic nature of the phenomenon means that a complete solution, taking into account all the fluctuating values, is computationally very demanding. The task of turbulence modelling is to create models and manipulate equations to be able to simulate turbulence interaction for specific conditions [11].

There exist several different approaches to turbulence modelling such as: Direct Numerical Simulation (DNS), Reynolds-Averaged Navier-Stokes Equations (RANS) and Large Eddy Simulation (LES). In the scope of this thesis a RANS turbulence model is used, as it is less computationally expensive then the others.

Turbulence causes the values of pressure, velocity and other properties to fluctuate in time and space. The Reynolds-Averaged Navier-Stokes are assembled by decomposing the values of pressure and velocity into a sum of mean ($\overline{\mathbf{u}}$, $\overline{p}$) and fluctuating values ($\mathbf{u}'$, p') as follows:

$$\mathbf{u} = \overline{\mathbf{u}} + \mathbf{u}' \,, \tag{2.49}$$

$$p = \overline{p} + p' \,. \tag{2.50}$$

By inserting Eq. 2.49 and 2.50 into Eq. 2.11 and eliminating products of mean and fluctuating values, the following expression is given:

$$\frac{\partial \overline{\mathbf{u}}}{\partial t} + \nabla \cdot (\overline{\mathbf{u}}\,\overline{\mathbf{u}}) - \nabla \cdot (\nu \nabla \overline{\mathbf{u}}) = -\nabla \overline{p} + \nabla \cdot (\overline{\mathbf{u}'\mathbf{u}'}) \,, \tag{2.51}$$

$$\nabla \cdot \overline{\mathbf{u}} = 0 \,,$$

where the term $\overline{\mathbf{u}'\mathbf{u}'}$ is a second rank symmetric tensor called the Reynolds stress tensor $\mathbf{R}$:

$$\mathbf{R} = \overline{\mathbf{u}'\mathbf{u}'} \,. \tag{2.52}$$

The Reynolds Stress tensor can be assembled using the second rank symmetric mean velocity gradient $\overline{\mathbf{S}}$ and turbulent viscosity ν_t:

$$\mathbf{R} = \underbrace{\nu_t}_{\text{turbulent viscosity}} \underbrace{\frac{1}{2} \left[\nabla \overline{\mathbf{u}} + (\nabla \overline{\mathbf{u}})^T \right]}_{\text{tensor } \overline{\mathbf{S}}} \,, \tag{2.53}$$

where the turbulent viscosity ν_t is modelled using the velocity scale $\mathbf{U}$, the length-scale Δ and a dimensionless constant A, which allows the model to be tuned to actual physical phenomena:

$$\nu_t = A\,\mathbf{U}\Delta \,. \tag{2.54}$$

The velocity scale can be approximated using turbulent kinetic energy $U \approx |\mathbf{u}'|$, where the turbulent kinetic energy is given by:

$$k = \frac{3}{2}\mathbf{u}'^2 \,. \tag{2.55}$$

In the scope of this thesis a two equation RANS model, called $k - \omega$ SST model [15] is used. It is a combination of the $k - \varepsilon$ model [16, 17] and the $k - \omega$ model [18].

2.8.1.   The $k - \varepsilon$ Model

This model is a popular, yet simple, two-equation model consisting of two partial differential equations used to describe turbulence. The first of the two equations describes the turbulence kinetic energy k:

$$\frac{\partial k}{\partial t} + \nabla \cdot (\overline{\mathbf{u}}k) - \nabla \cdot [(\nu_{eff})\nabla k] = G - \varepsilon \,. \tag{2.56}$$

The second equation of the $k - \varepsilon$ model is the equation for the turbulent dissipation ε, i.e. the dissipation of the turbulent kinetic energy:

$$\frac{\partial \varepsilon}{\partial t} + \nabla \cdot (\overline{\mathbf{u}}\varepsilon) - \nabla \cdot [(\nu_{eff})\nabla \varepsilon] = C_1 \, G \frac{\varepsilon}{k} - C_2 \frac{\varepsilon^2}{k} \,. \tag{2.57}$$

Where the terms for G used in Eq. 2.56 and 2.57 and for ν_t are given by:

$$G = \nu_t \left[\frac{1}{2}(\nabla\overline{\mathbf{u}} + \nabla\overline{\mathbf{u}}^T) \right]^2 \,, \tag{2.58}$$

$$\nu_t = C_\mu \frac{k^2}{\varepsilon} \,. \tag{2.59}$$

A detailed overview of the model, its implementation and the various constants used, is given by Launder et al. in [16, 17].

2.8.2.   The $k - \omega$ SST Model

The $k - \omega$ is the result of the combination of the $k - \varepsilon$ model and the $k - \omega$ models. The $k - \varepsilon$ model is used for modelling the the turbulence in the stream far from the wall, and the $k - \omega$ developed by Wilcox [18] is used for the inner boundary layer close to the wall. The fundamental two-equation model is described by:

$$\frac{\partial k}{\partial t} + \nabla \cdot (\overline{\mathbf{u}}k) - \nabla \cdot [(\nu_{eff})\nabla k] = min\,(G, C_1, \beta^* k\omega) - \beta^* k\omega\,, \tag{2.60}$$

describing the turbulent kinetic energy k, and the following equation describing the specific dissipation rate ω:

$$\frac{\partial \omega}{\partial t} + \nabla \cdot (\overline{\mathbf{u}}\omega) - \omega\nabla \cdot \overline{\mathbf{u}} - \nabla \cdot [\nu_{eff}\nabla\omega] = \gamma\,min\left[S_2, \frac{c_1}{a_1}\beta^*\omega\,max\left(a_1\omega, b_1 F_{23}\sqrt{S_2}\right)\right]$$
$$- \beta\omega^2 + (1 - F_1)CD_{k\omega}\,. \tag{2.61}$$

Where the terms for G used in Eq. 2.60 are given by:

$$G = \nu_t S_2\,, \tag{2.62}$$

$$S_2 = 2\left[\frac{1}{2}(\nabla\overline{\mathbf{u}} + \nabla\overline{\mathbf{u}}^T)\right]^2\,, \tag{2.63}$$

and the turbulent viscosity ν_t is described by:

$$\nu_t = \frac{a_1 k}{max\left[a_1\omega, b_1 F_{23}\sqrt{2}\left|\frac{1}{2}(\nabla\overline{\mathbf{u}} + \nabla\overline{\mathbf{u}}^T)\right|\right]}\,. \tag{2.64}$$

Eq. 2.60 and 2.61 describe the $k - \omega$ SST model according to Menter and Esch [15] with updated coefficients from [19]. The consistent production term from [15] and [19] were updated according to [20], while the optional F_3 term was added according to [21].

2.9.   Closure

This chapter introduced the basic equations and methods used to solve fluid flow problems using CFD.

The next chapter will focus on the additional equations and mathematical models used for describing cavitating flows in CFD.

3 | Cavitation Mathematical Model

3.1. Introduction

The previous chapter gave a brief overview of the Finite Volume Method and the governing equations for incompressible Newtonian fluid flow, which is an important basis for any CFD simulation.

The present chapter deals with the physics of cavitation inception, the dynamics of vapour cavities and the formulation of mathematical models, describing cavitation, in CFD.

3.2. Cavitation Inception

Although it was previously stated that cavitation occurs when the pressure in a fluid flow drops below the saturated vapor pressure, in reality, cavitation inception is more complicated to define. Research has shown, that the cohesive forces between the water molecules have a great influence on the inception [22]. The cohesive forces are represented by surface tension s, and the pressure they exert on a bubble is equal to:

$$p_{st} = \frac{2s}{R_b} \qquad (3.1)$$

Because of this pressure, theoretically, the fluid does not cavitate at the vapor saturation, but at a lower pressure called the inception pressure. This difference between the vapor saturation pressure and the inception pressure is defined as the tensile strength of the

fluid [3]. The mutual attraction between water molecules is very strong. So strong in fact, that theoretically, pure water does not cavitate. However, it is nearly impossible to create "pure" water. Contaminations, like dissolved gas particles, always exist in water, and lower the tensile strength of water.

In practice, the main mechanism for inception is the growth of these small gas bubbles called *nuclei* [3]. They may vary in size, from a few microns to nearly visible bubbles of the order of 1 mm. Nuclei tend to escape the fluid through two mechanisms: bubble rise and dissolution.

The bubble rise velocity is governed by the Stokes' law Eq. 3.2, which equates the buoyancy of the bubble to the drag force:

$$u_b = \frac{g{D_b}^2}{18\nu} \tag{3.2}$$

Logically, all gas bubbles should, in time rise to the surface and escape the fluid. However, in nature, turbulent motions in the upper layer of the fluid may keep the bubbles from getting to the surface and trap them in the fluid.

In the case of dissolution, the air in the bubble dissolves in the surrounding water due to diffusion and the vapor in the bubble condensates. Transport of gas through the bubble wall is governed by Henry's law, which states that at a constant temperature, the amount of given gas dissolved in a given type and volume of liquid is directly proportional to the partial pressure of a given gas in equilibrium with that liquid. This is relatively slow process, much slower then evaporation.

Another "weak spot" in the water are the adhesive forces between the water and other materials. These forces are much lower then the cohesive forces, so when low pressure areas occur around a surface, like the surface of a wing, the cavitation will start at the surface, where the tensile strangth of the fluid is weaker. The roughness of the surface also plays a part in cavitation inception. The micro-chasms in the surfaces, can store nuclei, which in turn act as cavitation sources.

To summarize, because of the need to know the concentration and size of nuclei, cavitation inception pressure is difficult to determine accurately. In sea water, the breaking of waves and abundant biological life, serve as excellent sources of nuclei. Experiments show that the tensile strength of sea water in prototype conditions is close

to zero, and that actually cavitation will take place at the saturated vapor pressure [3]. In this regard, this thesis will also presume cavitation inception at the vapor saturation pressure.

3.3.   Bubble Dynamics

The pressure inside a spherical bubble can be expressed as the sum of the vapor pressure and the free gas pressure inside the bubble. This pressure counteracts the hydrostatic pressure of the fluid p_h and the surface tensions pressure. For a stationary bubble of radius R_b, that isn't changing in volume, an equation for determining the value of the vapor pressure can be given as:

$$p_v = p_h + \frac{2s}{R_b} - p_g,$$
(3.3)

where p_v is the vapor pressure and s is the surface tension. If the equation is unbalanced, the bubble will increase or decrease in size until an equilibrium is achieved.

The behaviour of the bubble was first derived by Lord Rayleigh [23]. Later, Plesset [24] combined it with the contents of a gas-vapor bubble and the Rayleigh-Plesset equation as seen in Eq. 3.4 was formed:

$$\frac{p_v + p_g - p_h}{\rho} = R_b \frac{\mathrm{d}^2 R_b}{\mathrm{d}t^2} + \frac{3}{2} \left(\frac{\mathrm{d}R_b}{\mathrm{d}t} \right)^2 + \frac{4\nu}{R_b} \frac{\mathrm{d}R_b}{\mathrm{d}t} + \frac{2s}{\rho R_b}.$$
(3.4)

This equation shows very important occurence in cavitating flows, illustrated in Fig.3.1.
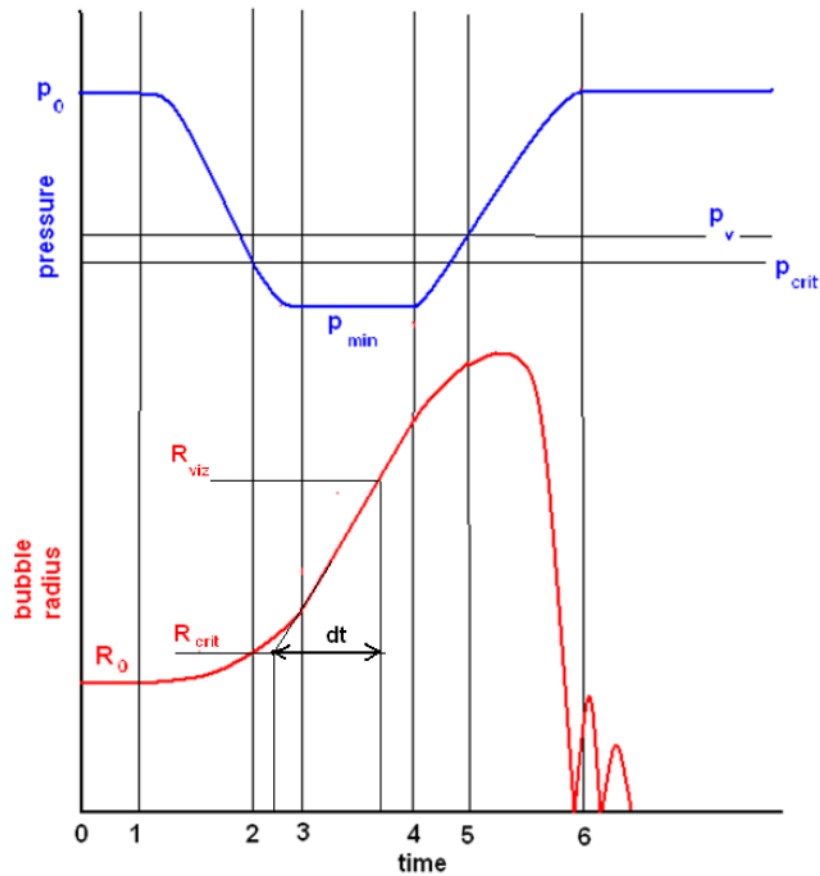
Figure 3.1: Bubble growth graph. [3]

As the pressure drops, the bubble begins to grow, and reaches a linear growth rate as the pressure stabilizes at p_{min}. When the pressure increases, the bubbles rate of growth begins to decrease, but it overshoots past the vapor pressure value p_v. This inertia causes the bubble to enter a high pressure area with a considerable size, and as the pressure difference on the bubble wall is very significant, the bubble rapidly collapses, until the walls of the bubble touch and it implodes. The energy of the collapse is then converted into a very high local pressure and can cause damage on mechanical structures in the vicinity of the implosion.

The Rayleigh-Plesset equation Eq. 3.4 is often used in CFD to provide a model for the phase change of water into vapor when cavitation occurs.

3.4.   Cavitation Modeling in CFD

Now that a basis for understanding the behavior of cavitation has been established, an implementation of models, that describe this behavior, in CFD will be elaborated upon. There exist four main problems when trying to solve cavitating flows in CFD.

Firstly, the flow in question is multiphase. In most cases, the flow is assumed to be two-phase, with the phases being liquid and vapor. In certain fringe cases, a third phase, representing the free gas may be introduced [25]. Each phase must satisfy the Conservation Laws, so the number of equations that must be solved increases with the implementation of phases. Additionally, there is the problem of mass transfer between the phases. This can be solved using the Rayleigh-Plesset equation Eq.3.4, but solving the complete equation is computationally expensive [25].

Secondly, there is the problem of determining the physical properties and behavior of the mixture. In other words, the two phases interfere with each other and disrupt the flow. For instance, the velocity of the liquid and vapor phase isn't equal, and therefore there exists a shear force on the interface between the phases.

Thirdly, the question of the location of the interface between the phases. Because of the nature of the discretisation of space in the FVM, it is difficult to show the exact location of the change from one phase to another. Also, the general property ϕ was, so far, generally assumed to be linearly distributed across a CV. In the case of phase change, in certain cells this is incorrect. Since if the phase change takes place inside a CV, a discontinuity in the distribution of ϕ, inside that CV, must exist. This can cause numerical errors in the solution. The problem of interface modeling in CFD, however, will not be further discussed in this thesis.

Lastly, there is the question of turbulence. Recent research has shown that turbulence has an influence on the development of cavitation and the seperation of cavities [26]. But, the inclusion of turbulence models makes the system of equation more unstable and difficult to solve.

With these problems in mind, certain assumptions about the flow are made in order to simplify the set of equations required to solve. Considering this cavitating flow models can be seperated into [25]:

- **Two Fluid Models**

  These full seven equation models are the most complete. They are formed from

the Conservation Laws for each phase and a separate transport equation for the volume ratio of the vapor phase inside the CV, α. This equation models the transfer of mass from one phase to another. Two Fluid Models take into account the non-equilibrium effects between the phases (differences in pressure, velocity and temperature). Turbulence may also be modeled with additional equations. Since complete Two Fluid Models are computationally expensive, they are used only simple geometries and inviscid flows.

- **Reduced Models with Five Equations**

  These models are obtained from a simplification of the complete two-fluid model. They are comprised of two mass conservation equations, one conservation equation for the mixture momentum, one conservation equation for the mixture energy and one non-conservative equation for α to describe the flow topology. They involve two temperatures, so it is possible to reproduce thermodynamic non-equilibrium effects for cavitation simulation in diesel injectors.

- **One Fluid Mixture Models**

  These models treat the fluid as a mixture, where the physical properties of the mixture are determined by the value of α. The models are comprised of three conservation laws for the mixture and an additional equation for α. These models are very common and will be further discussed in this thesis.

3.4.1.   One Fluid Mixture Models

The One Fluid Mixture Model, also called the Diffusion Model [27] is based on the assumption that the liquid and vapor phases have the same dynamics, and the slip between the phases can therefore be neglected. The velocity of both phases at the interface is considered equal and denoted as $\mathbf{u}$. This model focuses on the behavior of the mixture composed of the vapor and liquid phase, with the density of the mixture defined as:

$$\rho_m = \alpha \rho_v + (1 - \alpha)\rho_l, \tag{3.5}$$

where ρ_l is the liquid phase density, ρ_v is the vapor phase density and α is the volume ratio of the vapor phase inside the CV.

If it is presumed that the change in temperature is negligible, the Conservation of Energy can be disregarded and the equations for the flow are defined as:

$$\frac{\partial \rho_m}{\partial t} + \nabla \cdot (\rho_m \mathbf{u}) = 0, \tag{3.6}$$

$$\frac{\partial (\rho_m \mathbf{u})}{\partial t} + \nabla \cdot (\rho_m \mathbf{u}\mathbf{u}) = \nabla \cdot \boldsymbol{\sigma}, \tag{3.7}$$

where Eq. 3.6 is the Conservation of Mass for the mixture and Eq. 3.7 represents the Conservation of Linear Momentum of the mixture.

An additional equation for the volume ratio of the vapor phase α is required to close the system. Here, three approaches were developed.

The first approach treats the mass transfer between phases explicitly. The transfer modeled as a source term Γ_g in the transport equation for α Eq. 3.8.

$$\frac{\partial \alpha}{\partial t} + \nabla \cdot (\alpha \mathbf{u}) = \frac{\Gamma_g}{\rho_v}. \tag{3.8}$$

The source term is modeled with two terms as seen in Eq. 3.9. The term m^- represents the vaporization process, while the second term, m^+ represents the condensation process.

$$\Gamma_g = m^- + m^+. \tag{3.9}$$

A popular model for the terms was developed by Merkle [28] shown in Eq. 3.10 and Eq. 3.11.

$$m^- = \frac{C_{dest}\rho_l^2 min(0, p_m - p_{vs})\alpha}{\rho_v(0,5\rho_l U_\infty^2)t_\infty} \tag{3.10}$$

$$m^+ = \frac{C_{prod}\rho_l max(0, p_m - p_{vs})(1-\alpha)}{(0,5\rho_l U_\infty^2)t_\infty} \tag{3.11}$$

Another very popular model was developed by Kunz [29], and can be seen in equations Eq. 3.12 and Eq. 3.13.

$$m^- = \frac{C_{dest}\rho_v min(0, p_m - p_{vs})(1 - \alpha)}{(0, 5\rho_l U_\infty{}^2)t_\infty} \tag{3.12}$$

$$m^+ = \frac{C_{prod}\rho_v \alpha (1 - \alpha)^2}{t_\infty} \tag{3.13}$$

Both models are experimentally derived and similar in nature. They define the intensity of vaporization with the difference between the mixture pressure p_m and the vapor saturization pressure p_{vs}. In the Merkle model, if the pressure p_m is lower then p_{vs}, vaporization occurs, and if it is higher, condensation occurs. This difference simulates the inertia of the cavitation bubble. The Kunz model uses a simplified form of the Ginzburg-Landau potential for the condensation term [29]. Both models use experimental constants C_{dest} and C_{prod}, and reference values U_∞ and t_∞, that are used to adapt the model to simulation conditions.

The second approach to defining an equation for α is somewhat similar to the first. Again, the mass transfer between phases is treated explicitly, but the mass transfer source term is derived from a simplified Rayleigh-Plesset equation. Such models were successfully proposed by Kubota [30], Singhal [31] and the most famous Schnerr-Sauer [8] model which can be seen here:

$$\frac{\partial \alpha}{\partial t} + \nabla \cdot (\alpha \mathbf{u}) = \left(\frac{n_0}{1 + \frac{4}{3}\pi R_b{}^2} \right) \frac{d}{dt} \left(\frac{4}{3}\pi R_b{}^3 \right), \tag{3.14}$$

where the change of the cell vapor fraction α now depends on the number of nuclei n_0 per cell volume times the volume change of a single cavitation bubble $\frac{4}{3}\pi R_b{}^3$ and the convective transport [8].

The change of R_b is derived from the Rayleigh-Plesset equation Eq. 3.4, that can be simplified into:

$$R_b \frac{d^2 R_b}{dt^2} + \frac{3}{2} \left(\frac{dR_b}{dt} \right)^2 = \sqrt{\frac{2}{3} \frac{p_{vs} - p_m}{\rho_l}} \tag{3.15}$$

The right hand side of the equation is an adequate description of inertia-controlled bubble growth [8]. In practice, this term is often implemented as a basis for constructing

m^- and m^+ terms and a mass transfer source term is defined as in Eq. 3.9.

Although this formulation is considered more physically relevant, the Rayleigh-Plesset equation is assumed to govern the radius evolution of a single spherical bubble, whereas clouds of vapor are composed of many bubbles that strongly interact with each other [4].

The last approach uses a thermodynamic state law to express the value of α. The most common one is the Barotropic State Law that states that the void fraction value α is solely determined by the hydrostatic pressure in the fluid.

$$\alpha = f(p) \tag{3.16}$$

The pressure p, in turn, is coupled with the density of the liquid ρ_m, which can be seen in Fig. 3.2.
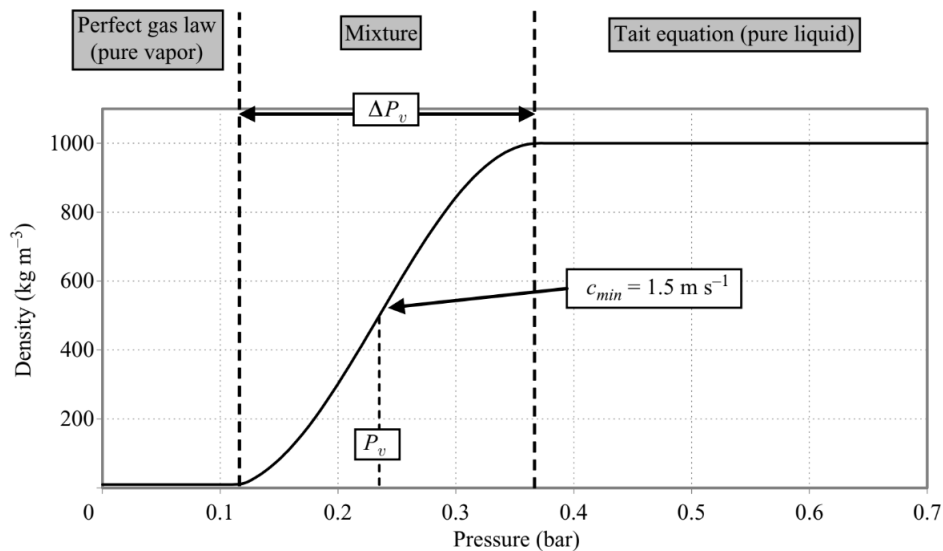
Figure 3.2: Density change according to the Barotropic State Law [4].

Three distinct areas on the curve can be distinguished. The first is far below the vapor saturation pressure, where the fluid behaves like a perfect gas and follows the perfect gas equation:

$$\frac{p}{\rho_m} = RT \tag{3.17}$$

where p is the pressure, ρ_m is the mixture density, which is, in this case, the vapor density. T is the temperature and R is the gas constant.

The second is the area far above the vapor saturation pressure, where the fluid behaves like a liquid and can be described using the Tait state law [32] as seen in Eq. 3.18.

$$\frac{\rho_m}{\rho_{ref}} = \left(\frac{p + p_0}{p_{ref}^T + p_0} \right)^{\frac{1}{n_T}} \tag{3.18}$$

The value ρ_{ref} is the reference density of the liquid, p_{ref}^T is the pressure at the outlet, and p_0 and n_T are constants that describe the physical properties of the liquid.

While the first two areas describe low compressibility configurations, the area around the vapor saturization pressure, with a high slope, describes the high compressibility of the mixture of the two phases [4]. Several equations of state for applied to vapor-liquid phase equilibria may be found in literature [33]. Most of them use the sound velocity c as a value for determinig the compressibility.

The major difference between the state law approach and the previous two is the absence of time relaxation in the state law models [4]. The state law models in their original form define both vaporization and cavitation as instantaneous processes. However, this can be corrected in implementations if needed.

3.5.   Closure

This chapter presented the theoretical background needed for understanding the inception and behavior of cavitation. It also introduced cavitation models which can be implemented in CFD and elaborated on One Fluid Cavitation Models.

The following chapter will describe the geometries used in the simulations, and the simulation setup for the validation of the Schnerr-Sauer cavitation model.

4 | Geometry and Computational Domain

4.1. Introduction

The previous chapter dealt with the physics of cavitation and the modeling of cavitation for use in CFD.

This chapter will elaborate the setup of the simulations that were performed with the goal of validating cavitation models. The chapter will first describe the model geometry, computational domain and case setup for the NACA009 Truncated Hydrofoil and then for the Delft Twist 11 Hydrofoil.

4.2. NACA Truncated Hydrofoil

4.2.1. Model Geometry

The NACA009 Truncated Hydrofoil is a symmetrical airfoil, based on the NACA0009 airfoil.
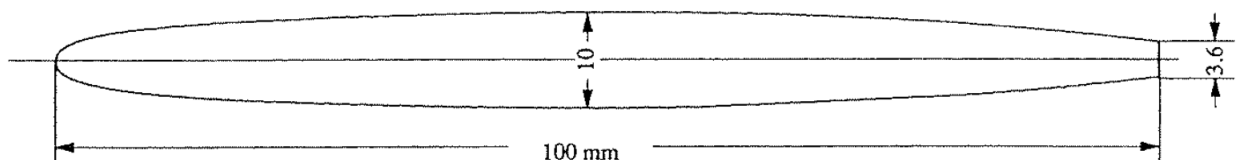
Figure 4.1: Dimesions of the NACA009 Truncated Hydrofoil [5].

The chord length of the foil is 100 mm, while the maximum thickness is equal to 10 mm. The trailing edge ends with a thickness of 3,6 mm. These dimensions were taken from the Phd Thesis of Philippe Dupont [5].

The curve of the airfoil was calculated using the equation in Eq. 4.1.

$$y = \frac{1}{2}(0,346755\sqrt{x} - 0,43071x + 0,49929x^2 - 0,49861x^3 + 0,119515x^4). \tag{4.1}$$

4.2.2. Computational Domain

The curve, aquired from the Eq. 4.1, was imported into Pointwise Mesh Generation Software in order to construct the Computational Domain. Only 2-D simulations were ran on the NACA009 foil, so the mesh was constructed as a structured 2-D mesh with 215,097 hexahedral cells and one cell length in the z coordinate axis direction. The domain inlet was set at 2 chord lengths from the leading edge of the foil, while the outlet was set at 4 chord lengths from the trailing edge. The foil is set at an angle of attack α_{at} of 2,5°.
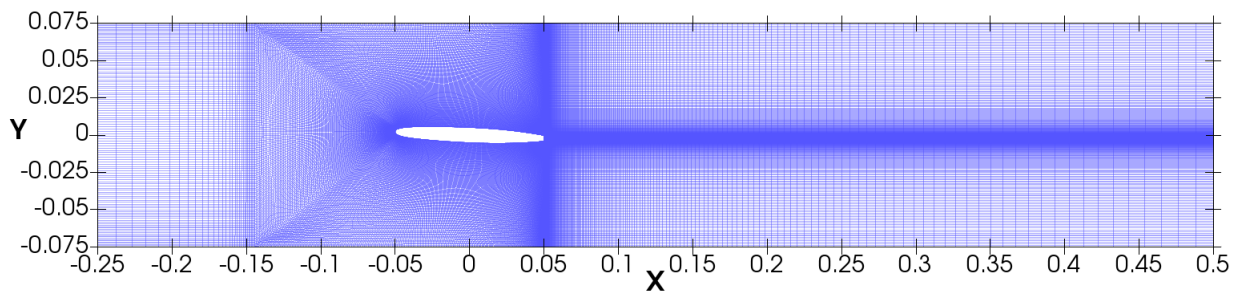
Figure 4.2: The Computational Domain around the NACA009 foil.

From Fiq. 4.2, it can be observed that the mesh is more dense around the foil and behind the trailing edge. This is the area where cavitation is expected. The areas around the leading and trailing edge of the foil can more clearly be seen on figures Fig. 4.3 and Fig. 4.4.
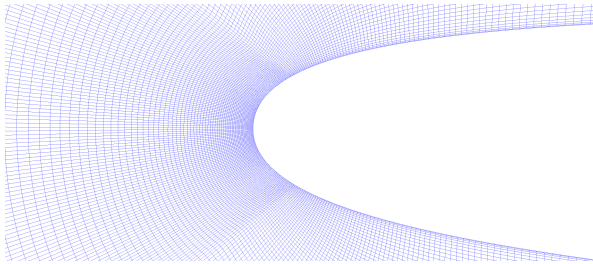
Figure 4.3: The mesh around the leading edge of the NACA009 foil.
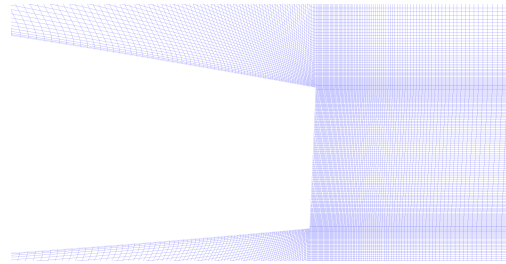
Figure 4.4: The mesh around the trailing edge of the NACA009 foil.

4.2.3.   Case Setup

Simulations are divided into steady non-cavitating flow simulations, that were executed using the `simpleFoam` solver in `foam-extend 4.0`, and transient cavitating flow simulations executed using the `interPhaseChangeFoam` implemented in `OpenFOAM-7`. All simulations were ran as 2-D simulations, so the changes of the properties in the z coordinate axis direction were ignored. The upper and lower wall were treated as a slip condition, meaning there was no reduction in fluid velocity at these surfaces. For the fluid, in all simulations only water was considered. In all cases, the temperature change in the flow was disregarded.

Simulations were performed for inlet flow speeds of 20 and 30 m/s, using a laminar and $k - \omega$ SST turbulence model. For the cavitating flow simulations, cavitation coefficient σ_{cav} was defined as:

$$\sigma_{cav} = \frac{2(p_{outlet} - p_{vs})}{\rho_l u_{inlet}^2}. \tag{4.2}$$

During simulations, the cavitation coefficient was held at $\sigma_{cav} = 0,81$.

Also, for every case the pressure coefficient C_P, lift coefficient C_L and drag coefficient C_D was measured. These dimensionless coefficents were used to compare the simulation results. The equations for each coefficient are as follows:

$$C_P = \frac{2(p - p_{ref})}{\rho_{ref} u_{ref}^2}, \tag{4.3}$$

$$C_L = \frac{2L}{\rho_{ref} u_{ref}{}^2 A_{ref}},$$ (4.4)

$$C_D = \frac{2D}{\rho_{ref} u_{ref}{}^2 A_{ref}}.$$ (4.5)

For the reference pressure of the pressure coefficient, the outlet pressure p_{outlet} was chosen. As for the other reference values in the coefficients, for the reference velocity u_{ref}, the velocity at the inlet u_{inlet} was chosen, and for the reference density ρ_{ref}, the liquid density ρ_l was chosen. The variables L and D refer to the lift and drag force respectfully.

What follows is the setup for the individual cases.

simpleFoam

The `simpleFoam` solver uses the previously described SIMPLE algorithm for solving the system of linear equations. In the scope of this thesis, two simulations of laminar fluid flow, and two simulations of turbulent fluid flow were studied. The laminar flow simulations are physically inaccurate, because the Reynolds number far exceeds the turbulent flow threshold, but were executed to study the effect of turbulence on the cavitation. During laminar flow simulations only the fluid velocity u and pressure p are calculated. For the turbulent flow simulations, with the $k - \omega$ SST turbulence model, two additional values are calculated. The turbulent kinetic energy k and the specific dissipation rate ω.

The intention was to use these cases as a measuring stick for the cavitating flow simulations. In the following tables are the boundary conditions and initial values for each simulation.

Table 4.1: Boundary Conditions for the NACA009 laminar and turbulent flow `simpleFoam` simulations

		NACA009 `simpleFoam` Boundary Conditions			
No.	**Patch Name**	**Laminar FLow B.C.**		**Additional Turbulence B.C.**	
		U $[\mathrm{m/s}]$	**p** $[\mathrm{m^2/s^2}]$	**k** $[\mathrm{m^2/s^2}]$	ω $[1/\mathrm{s}]$
01	inlet	`fixedValue;` `uniform (`U_{ref}`);`	`zeroGradient;`	`fixedValue;` `uniform k`$_{ref}$`;`	`fixedValue;` `uniform` ω_{ref}`;`
02	outlet	`inletOutlet;` `uniform (0 0 0);` `uniform (`U_{ref}` 0 0);`	`fixedValue;` `uniform p`$_{ref}$`;`	`inletOutlet;` `uniform k`$_{ref}$`;` `uniform k`$_{ref}$`;`	`inletOutlet;` `uniform` ω_{ref}`;` `uniform` ω_{ref}`;`
03	foil	`fixedValue;` `uniform (0 0 0);`	`zeroGradient;`	`kqRWallFunction;`	`omegaWallFunction;`
04	up	`slip;`	`zeroGradient;`	`zeroGradient;`	`zeroGradient;`
05	down	`slip;`	`zeroGradient;`	`zeroGradient;`	`zeroGradient;`
06	frontBack	`empty;`	`empty;`	`empty;`	`empty;`

The `fixedValue` boundary conditions are *Dirichlet* boundray conditions with the reference value being the value of the property, defined at the boundary. The `zeroGradient` boundary conditions are *Neumann* boundary conditions and they define a zero value flux of the property at the boundary. The `inletOutlet` is a special *Dirichlet* condition, that sets multiple values of the property at the boundary, and differentiates between them according to the direction of the flow. In all simulations in the scope of this thesis, the `inletOutlet` condition was used to limit the backflow of the fluid back into the computational domain through the outlet patch. Although this condition isn't physically correct, it stabilizes the system of equations and if the outlet patch is put at a sufficient distance from the foil, the condition shouldn't affect the accuracy of the final solution. The `WallFunction` conditions are special conditions that describe the behavior of the property in the boundary layers, while the `slip` condition, which was already described, was, in this case, used to limit the influence of the wall on the fluid flow. Finally, the `empty` boundary condition, simply defines that this is a 2-D simulation and the change

of the property perpendicular to these boundary patches can be disregarded.

Following in the next two tables are the reference values used for the simulations. The reference pressure value was calculated using the equation Eq. 4.2 and the condition $\sigma_{cav} = 0,81$. For the turbulence, an intensity of 1% was chosen.

Table 4.2: Reference values for the NACA009 `simpleFoam` simulations ($u_{inlet} = 20$ m/s)

`simpleFoam` Reference Values ($u_{inlet} = 20$ m/s)			
U [m/s]	**p** [m²/s²]	**k** [m²/s²]	ω [1/s]
20	163,43	0,06	27,2

Table 4.3: Reference values for the NACA009 `simpleFoam` simulations ($u_{inlet} = 30$ m/s)

`simpleFoam` Reference Values ($u_{inlet} = 30$ m/s)			
U [m/s]	**p** [m²/s²]	**k** [m²/s²]	ω [1/s]
30	366,8	0,135	135

interPhaseChangeFoam

The `interPhaseChangeFoam` solver is a solver intended for transient homogenous mixture fluid flow. Contained in the `OpenFOAM-7` implementation of the solver, are implementations of the Merkle, Kunz and Schnerr-Sauer cavitation models. In the scope of this thesis, the Schnerr-Sauer model was validated. As with the `simpleFoam` simulations, four simulations were carried out. Due to the characteristics of cavitation, all simulations were transient, with two laminar flow simulations and two turbulent flow simulations. Again, due to the high Reynolds number, the laminar flow simulations were not physically correct.

The flow was treated as a homogenous mixture, and the values of the mixture velocity u and pressure p were calculated, as well as the liquid fraction ration α_l. For the turbulent flow, the $k - \omega$ SST turbulence model was chosen. The discretisation parameters are shown in Appendix A.

A comment should be made about the liquid fraction ratio α_l. In the `interPhaseChangeFoam` implementation of the Schnerr-Sauer cavitation model, the value that is calculated is the liquid fraction ration α_l instead of the void fraction ratio α from Chapter 3. These values are however directly linked with the following equation:

$$\alpha_l = 1 - \alpha \tag{4.6}$$

Table 4.4: Boundary Conditions for the NACA009 laminar and turbulent flow `interPhaseChangeFoam` simulations

NACA009 interPhaseChangeFoam Boundary Conditions						
No.	Patch Name	Laminar FLow B.C.			Additional Turbulence B.C.	
		$\mathbf{U}$ [m/s]	$\mathbf{p}$ [Pa,]	α_l [-]	$\mathbf{k}$ [m^2/s^2]	ω [1/s]
01	inlet	fixedValue; uniform (U$_{ref}$);	zeroGradient;	fixedValue; uniform (α_{ref} 0 0);	fixedValue; uniform k$_{ref}$;	fixedValue; uniform ω$_{ref}$;
02	outlet	inletOutlet; uniform (0 0 0); uniform (U$_{ref}$ 0 0);	fixedValue; uniform p$_{ref}$;	inletOutlet; uniform α_{ref}; uniform α_{ref};	inletOutlet; uniform k$_{ref}$; uniform k$_{ref}$;	inletOutlet; uniform ω$_{ref}$; uniform ω$_{ref}$;
03	foil	fixedValue; uniform (0 0 0);	zeroGradient;	zeroGradient;	kqRWallFunction;	omegaWallFunction;
04	up	slip;	zeroGradient;	zeroGradient;	zeroGradient;	zeroGradient;
05	down	slip;	zeroGradient;	zeroGradient;	zeroGradient;	zeroGradient;
06	frontBack	empty;	empty;	empty;	empty;	empty;

The boundary conditions are equivalent to the conditions in `simpleFoam` conditions. For the liquid fraction ration α_l, the inlet value was set to 1, so pure liquid phase water would flow into the computational domain. The vapor saturation pressure was set at 2300 Pa.

Table 4.5: Reference values for the NACA009 `interPhaseChangeFoam` simulations $(u_{inlet} = 20$ m/s$)$

interPhaseChangeFoam Reference Values ($u_{inlet} = 20$ m/s)				
$\mathbf{U}$ [m/s]	$\mathbf{p}$ [Pa,]	α_l	$\mathbf{k}$ [m^2/s^2]	ω [1/s]
20	163430	1	0,06	27,2

Table 4.6: Reference values for the NACA009 `interPhaseChangeFoam` simulations ($u_{inlet} = 30$ m/s)

`simpleFoam` Reference Values ($u_{inlet} = 30$ m/s)				
U [m/s]	**p** [Pa,]	α_1	**k** [m²/s²]	ω [1/s]
30	366800	1	0,135	135

4.3.   Delft Twist 11 Hydrofoil

4.3.1.   Model Geometry

The Delft Twist 11 Hydrofoil is a wing of rectangular planform, the section shape being uniform over the whole span, but the orientation with respect to the incoming flow varying in the spanwise direction. If the angle of attack is set at 0° at both ends of the wing, it is 11° at the mid-span. The geometrical model of the wing may be seen in the figure Fig. 4.5.
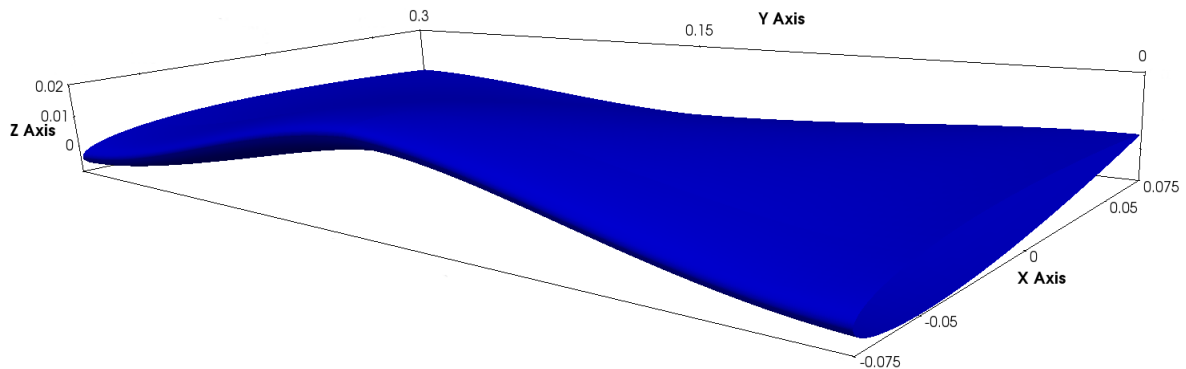
Figure 4.5: The Delft Twist 11 Hydrofoil

The section shape is a modified NACA 4-digit profile. Its basic shape is given by the function:

$$z = \frac{0,09}{0,2}(0,2969\sqrt{x} - 0,126x - 0,3516x^2 + 0,2843x^3 + 0,1015x^4), \qquad (4.7)$$

while the spanwise variation of the angle of attack is given by:

$$\alpha_{at} = \alpha_{max}(2|y-1|^3 - 3|y-1|^2 + 1), \qquad (4.8)$$

with the maximum angle of attack α_{max} being 11°.

It should be noted that, even though the equation Eq. 4.7, produces a finite thickness at the trailing edge, it was too small to satisfy the requirements of the milling process by which the Delft Twist 11 foil was manufactured, so the trailing edge thickness was modified to 0,4 mm.

4.3.2.   Computational Domain

A complete geometric description of the Delft Twisted Foil was acquired as a B-spline surface from [34]. Pointwise Mesh Generation Software was used to generate the computational domain. The inlet patch was designed as an arc in order to reduce the non-orthogonality between cells. The inlet was set at 2 chord lengths from the leading edge, while the outlet was set at 4 chord lengths from the trailing edge. At the ends of the foil the angle of attack α_{at} was set at -2°.
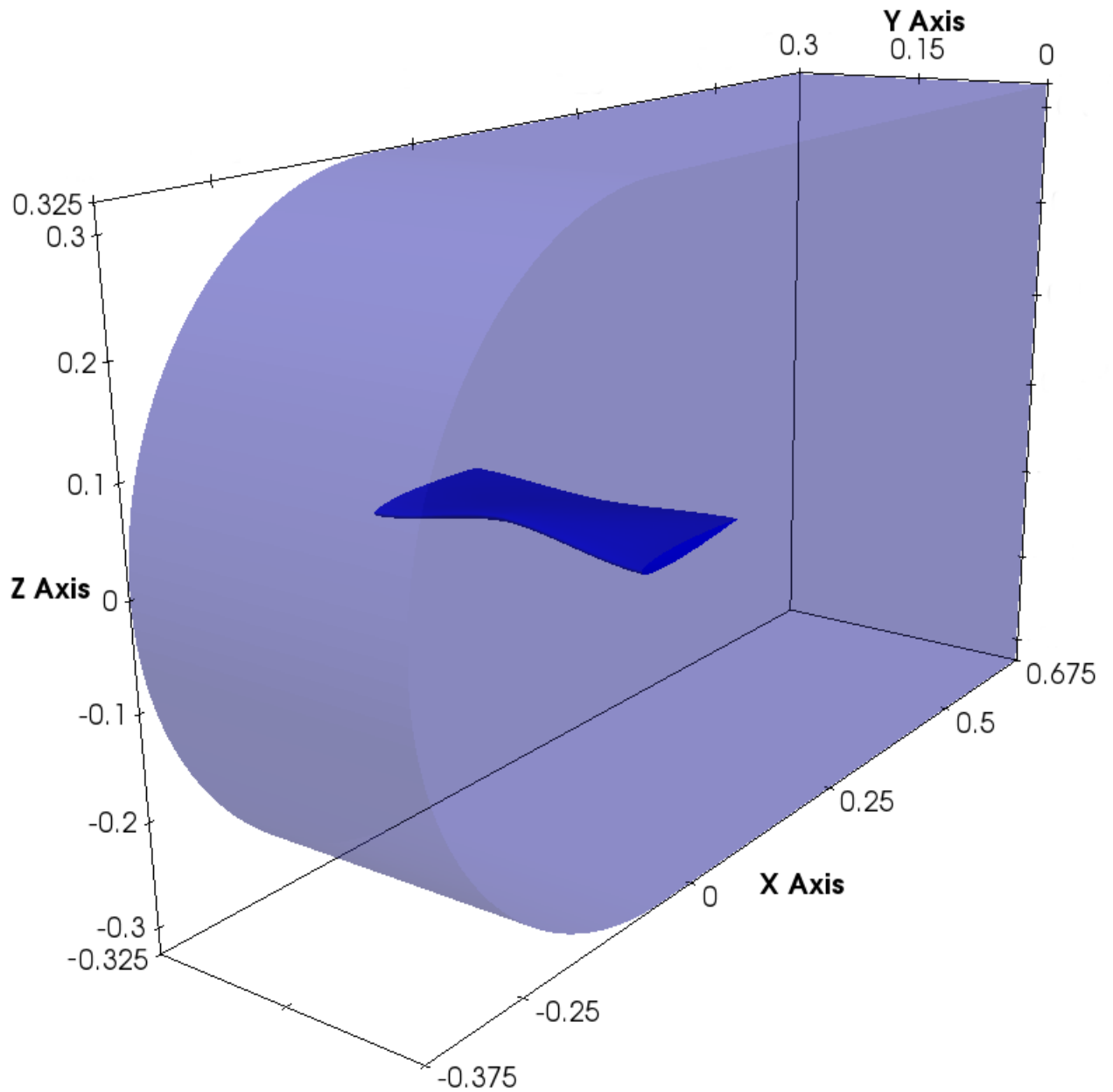
Figure 4.6: The Computational Domain around the Delft Twist 11 Hydrofoil

In reality however, since the wing is symmetric only half the domain seen in Fig. 4.2 was used in the simulations. From that, a 3-D structured mesh with 4,779,324 hexahedral cells was constructed and can be seen on Fig 4.7.
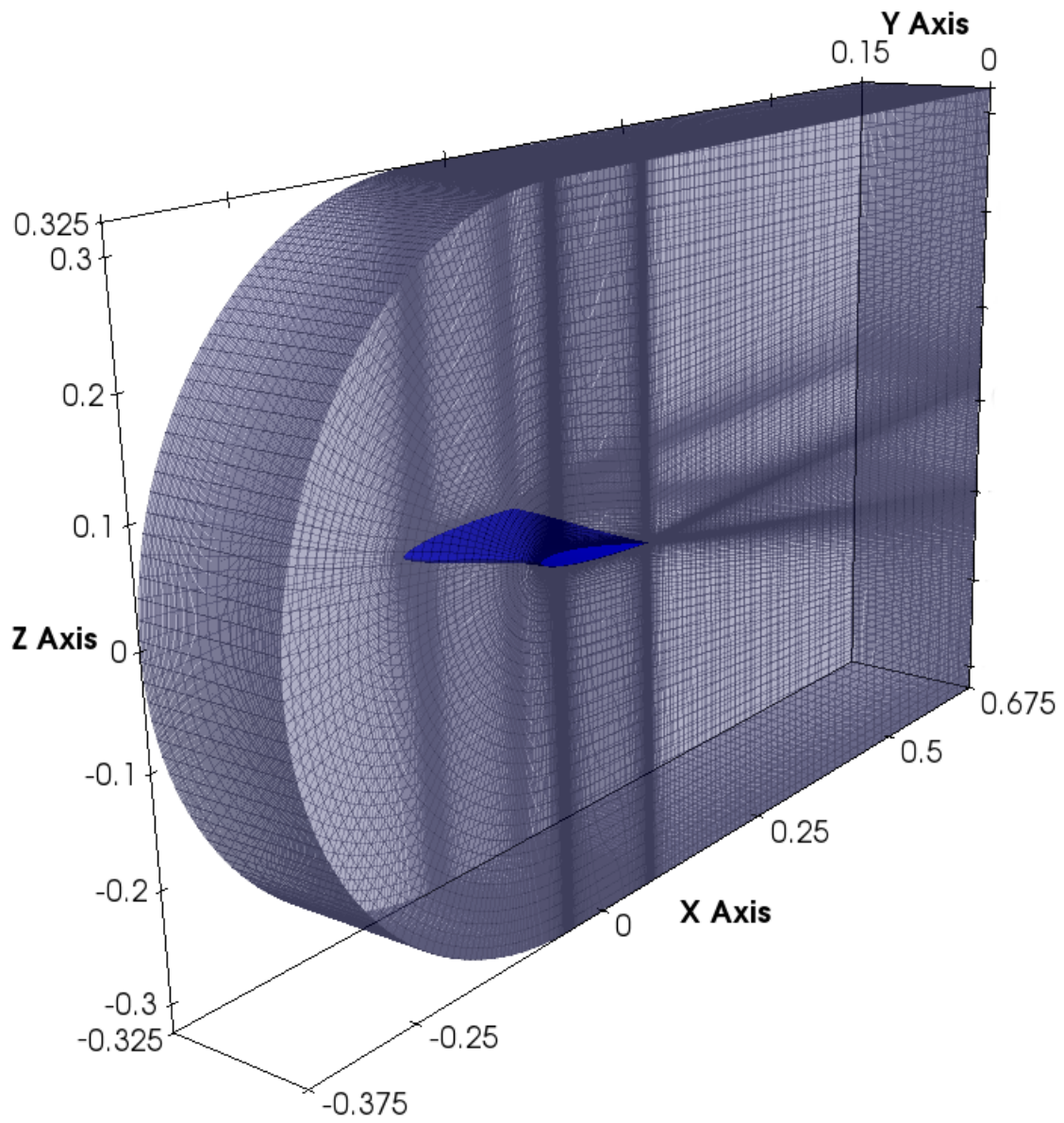
Figure 4.7: The Isolated Computational Domain around the Delft Twist 11 Hydrofoil

For a more detailed view of the mesh cross section, perpendicular to the flow direction, reference figure Fig 4.8.
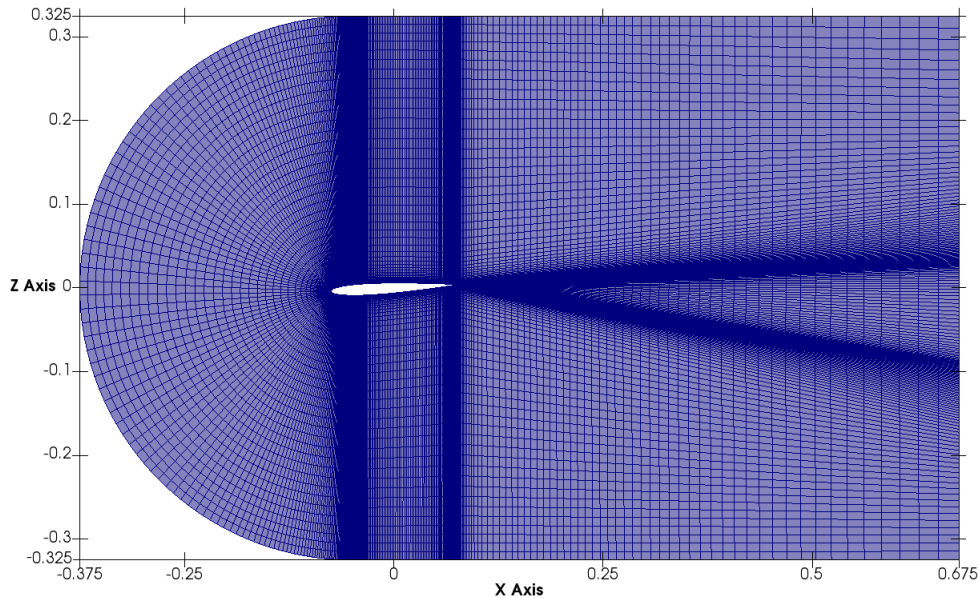
Figure 4.8: Cross Section of the Delft Twist 11 Hydrofoil Mesh

The cross section was taken at the end of the wing, and the angle of attack $alpha_{at}$ is clearly visible. Also, again, it can be observed that the mesh is more dense around the foil, and the trailing edge.

4.3.3.   Case Setup

As with the NACA009 foil, non-cavitating water flow simulations were performed using the `simpleFoam` solver in `foam-extend 4.0`, and transient cavitating water flow simulations, using the `interPhaseChangeFoam` implemented in `OpenFOAM-7`. Again, the temperature change of the fluid was disregarded.

Since the wing is symmetrical, and the boundary conditions are symmetrically arranged, it can be assumed that the flow on one side of the wing will mirror the other. Therefore the wing was divided at the mid-span line. At the divide, a `symmetry` boundary condition was used.

The dimensionless coefficients C_P, C_L and C_D were measured. Unlike in the NACA009 cases, for the Delft foil, simulations were perfomed with only one inlet fluid velocity $u_{inlet} = 6,75$ m/s.

```
simpleFoam
```

Equivalent to the NACA009 case setup, using the `simpleFoam` solver, one laminar flow and one turbulent flow simulation was performed. The setup for the cases on the Delft Twist 11 Hydrofoil can be seen below.

Table 4.7: Boundary Conditions for the Delft Twist 11 foil laminar and turbulent flow `simpleFoam` simulations

Delft Twist 11 `simpleFoam` Boundary Conditions					
		Laminar FLow B.C.		**Additional Turbulence B.C.**	
No.	**Patch Name**	**U** $[\mathrm{m/s}]$	**p** $[\mathrm{m^2/s^2}]$	**k** $[\mathrm{m^2/s^2}]$	ω $[\mathrm{1/s}]$
01	inlet	`fixedValue;` `uniform (U`$_\mathrm{ref}$`);`	`zeroGradient;`	`fixedValue;` `uniform k`$_\mathrm{ref}$`;`	`fixedValue;` `uniform ω`$_\mathrm{ref}$`;`
02	outlet	`inletOutlet;` `uniform (0 0 0);` `uniform (U`$_\mathrm{ref}$` 0 0);`	`fixedValue;` `uniform p`$_\mathrm{ref}$`;`	`inletOutlet;` `uniform k`$_\mathrm{ref}$`;` `uniform k`$_\mathrm{ref}$`;`	`inletOutlet;` `uniform ω`$_\mathrm{ref}$`;` `uniform ω`$_\mathrm{ref}$`;`
03	foil	`fixedValue;` `uniform (0 0 0);`	`zeroGradient;`	`kqRWallFunction;`	`omegaWallFunction;`
04	up	`slip;`	`zeroGradient;`	`zeroGradient;`	`zeroGradient;`
05	down	`slip;`	`zeroGradient;`	`zeroGradient;`	`zeroGradient;`
06	side	`slip;`	`zeroGradient;`	`zeroGradient;`	`zeroGradient;`
07	symmetry	`symmetry;`	`symmetry;`	`symmetry;`	`symmetry;`

The boundary conditions are very similar to the NACA009 boundary conditions, the difference being the `symmetry` condition. This condition simulates the mirrored values inside the domain, across the symmetry patch. It is a very valuable tool, since it enables the user to reduce the required domain space, and thereby the mesh size.

Table 4.8: Reference values for the Delft Twist 11 `simpleFoam` simulations

`simpleFoam` Reference Values ($u_{inlet} = 6.75$ m/s)			
U [m/s]	**p** [m^2/s^2]	**k** [m^2/s^2]	ω [1/s]
6,75	97	0,06	27,2

interPhaseChangeFoam

Two transient cavitating flow simulations, using the `interPhaseChangeFoam` implementation of the Schnerr-Sauer cavitation model, were performed. The simulation were setup identical to the NACA0009 cases performed in the scope of this thesis. The discretisation parameters for the simulations are the same as for the NACA009 simulations, and are shown in Appendix A. The setup for the cases can be seen below.

Table 4.9: Boundary Conditions for the Delft Twist 11 foil laminar and turbulent flow `interPhaseChangeFoam` simulations

		Delft Twist 11 `interPhaseChangeFoam` Boundary Conditions				
		Laminar FLow B.C.			Additional Turbulence B.C.	
No.	Patch Name	**U** [m/s]	**p** [Pa,]	α_l [-]	**k** [m^2/s^2]	ω [1/s]
01	inlet	fixedValue; uniform (U$_{ref}$);	zeroGradient;	fixedValue; uniform (α_{ref} 0 0);	fixedValue; uniform k$_{ref}$;	fixedValue; uniform ω_{ref};
02	outlet	inletOutlet; uniform (0 0 0); uniform (U$_{ref}$ 0 0);	fixedValue; uniform p$_{ref}$;	inletOutlet; uniform α_{ref}; uniform α_{ref};	inletOutlet; uniform k$_{ref}$; uniform k$_{ref}$;	inletOutlet; uniform ω_{ref}; uniform ω_{ref};
03	foil	fixedValue; uniform (0 0 0);	zeroGradient;	zeroGradient;	kqRWallFunction;	omegaWallFunction;
04	up	slip;	zeroGradient;	zeroGradient;	zeroGradient;	zeroGradient;
05	down	slip;	zeroGradient;	zeroGradient;	zeroGradient;	zeroGradient;
06	side	slip;	zeroGradient;	zeroGradient;	zeroGradient;	zeroGradient;
07	symmetry	symmetry;	symmetry;	symmetry;	symmetry;	symmetry;

Table 4.10: Reference values for the Delft Twist 11 `interPhaseChangeFoam` simulations

`interPhaseChangeFoam` Reference Values (u_{inlet} = 6.75 m/s)				
U [m/s]	**p** [Pa,]	α_1	**k** [m^2/s^2]	ω [1/s]
6,75	29000	1	0,06	60

4.4.   Closure

This chapter served as a description of the foil geometry and the setup of the simulations used to validate the Schnerr-Sauer cavitation model.

The next chapter will show the results of the simulations and compare them to results derived from experimental research.

5 | Results

5.1.   Introduction

The previous chapter described geometric characteristics of the NACA009 Truncated Hydrofoil and the Delft Twist 11 Hydrofoil. It also presented the case setup for the individual simulations performed on the foils.

This chapter will show the results of those simulations and compare them to data derived from experimental research. The chapter will also discuss the difficulties that occurred during the simulations.

5.2.   NACA009 Truncated Hydrofoil

The results of the simulations performed on the NACA009 Truncated Hydrofoil are presented in this section. The focus is put on the cavitating flow simulations, while the non-cavitating flow simulation results are used as a benchmark for comparison.

5.2.1.   Non-cavitating Flow

Simulations of non-cavitating flow were performed as steady state simulations, however an interesting phenomenon was witnessed. Because of the nature of the flow around the hydrofoil, vortexes started manifesting at the trailing edge of the wing. The vortexes cause the solution to oscillate, and the problem becomes a transient problem, so a single steady state solution cannot be formed. However since the simulation was performed as a steady state simulation, the time variable was disregarded and an arbitrary time vari-

able was defined that only serves to define the number of iteration steps for the solver. Therefore, the image of the flow at every time step, or iteration, is correct, however the time scale is incorrect. The solution shows the correct size and position of the vortexes, but the time frame, or frequency with which they occur is incorrect.
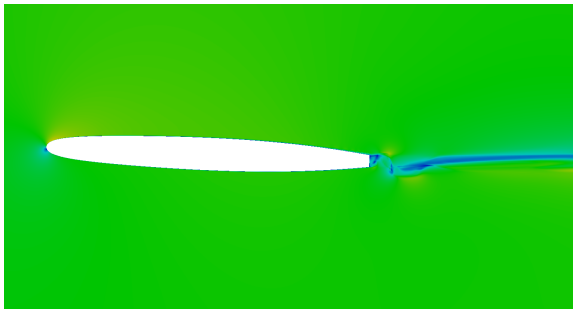
Time Step 1
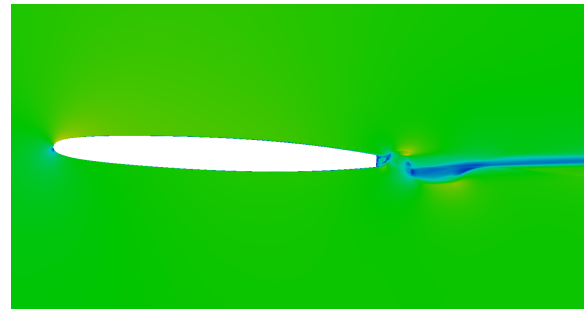
Time Step 2
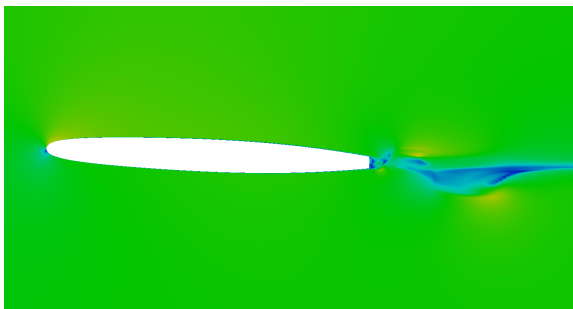
Time Step 3
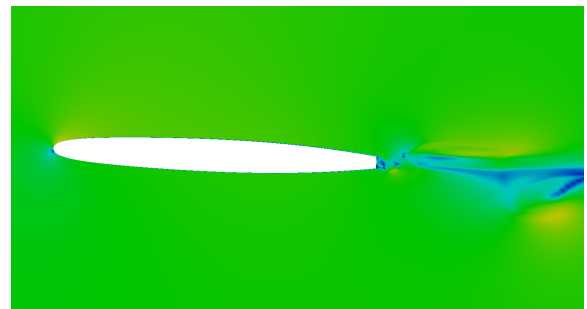
Time Step 4
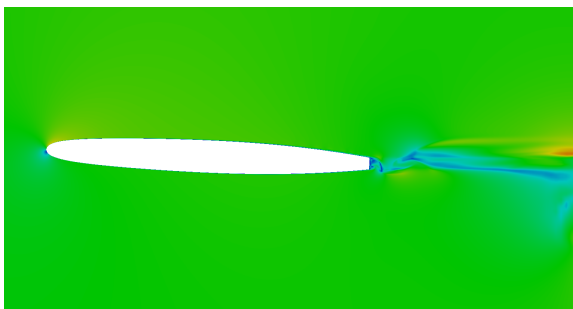
Time Step 5
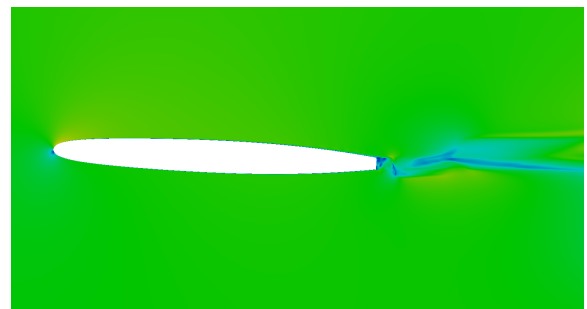
Time Step 6

Figure 5.1: Vortex formation in NACA009 `simpleFoam` simulations.

In an attempt to produce a solution for the average flow conditions, the results of each time step in the simulation were averaged. Since the time scale of the simulation

is incorrect, this averaging won't produce physically legitimate results. Still, it was presumed, this averaging would produce a sufficiently accurate image of the flow or at least better than individual time instances.

These averaged results were used to compute the pressure coefficient C_P. The pressure coefficient on the foil was drawn as a curve for the pressure and suction sides of the wing. A visual representation of the measurement is shown in the following figures.
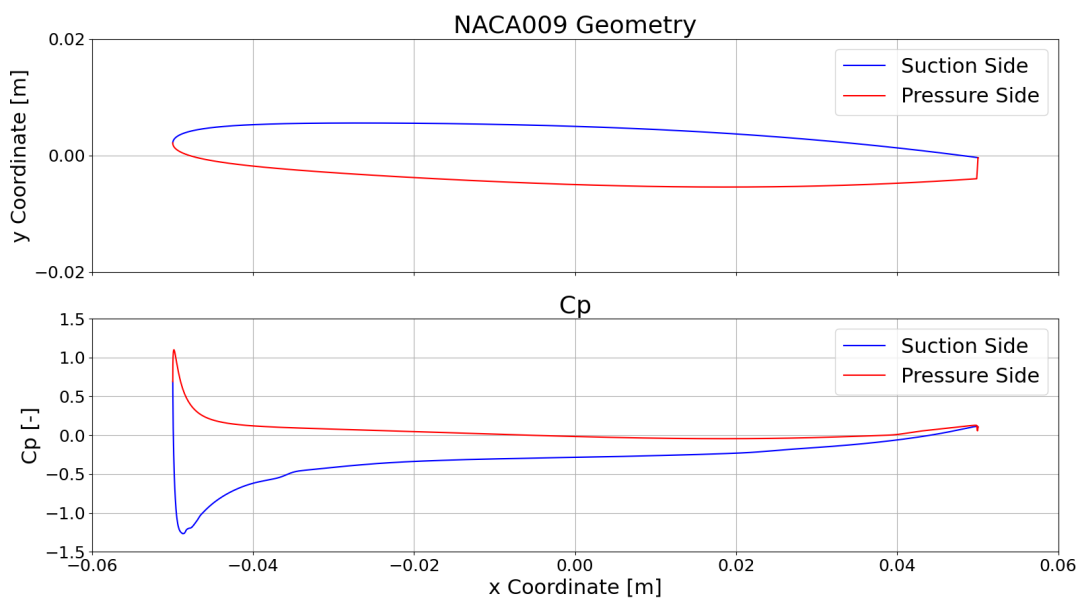
Figure 5.2: Representation of C_P on the NACA009 pressure side and suction side.
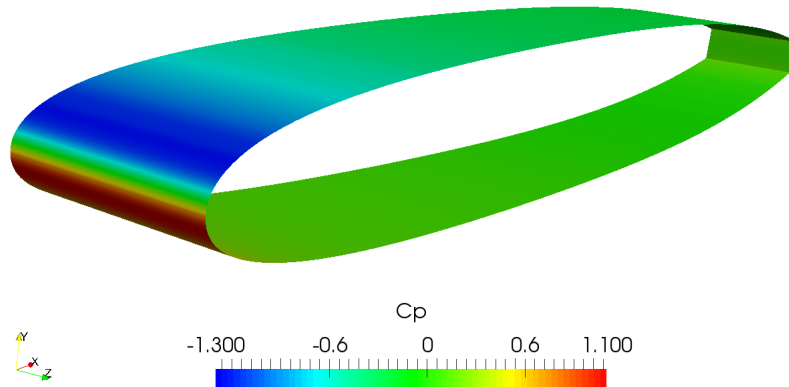
Figure 5.3: Pressure distribution on the foil in a non-cavitating flow.

The figures Fig. 5.2 and Fig. 5.3 represent the pressure distribution on the wing in the laminar flow conditions for the inlet velocity $u = 20$ m/s. However they are presented here merely to serve as a clarification for the measurement of the C_P curves. With that in mind, the rest of the results of the non-cavitating flow simulations will be skipped, and presented only when they are needed to contextualize the cavitating flow results.

5.2.2.   Cavitating Flow

Cavitating flow simulations were executed as transient simulations with a duration of about 0.2 seconds, using multiple machines. Some information on the computational demand of the simulations may be seen in the following table.

Table 5.1: NACA009 cavitating flow simulations CPU demand.

NACA009 Cavitating Flow Simulation Information					
Flow Conditions	Inlet Velocity [m/s]	Machine CPU	Simulated Time [s]	Average Time Step Size [s]	Simulation CPU Time
Laminar	20	Intel(R) Core(TM)2 Quad CPU Q6600 @ 2.40GHz	0.15	$4 \cdot 10^{-6}$	44h 11' 55"
	30	Intel(R) Core(TM) i7-4820K CPU @ 3.70GHz	0.15	$2.5 \cdot 10^{-6}$	18h 13' 8"
Turbulent	20	Intel(R) Core(TM) i5-3570K CPU @ 3.40GHz	0.15	$4 \cdot 10^{-6}$	18h 13' 8"
	30	Intel(R) Core(TM)2 Quad CPU Q6600 @ 2.40GHz	0.15	$2.5 \cdot 10^{-6}$	91h 46' 49"

Cavitation was successfully achieved in all simulations. Both the turbulent flow and laminar flow simulations showed vapor cavities emerging on the suction side of the foil near the leading edge and behind the trailing edge of the foil, as expected by the results of the pressure distribution around the foil in the non-cavitating flow simulations. A sequence of images depicting the shedding of a vapor cavity can be seen in Fig 5.4.
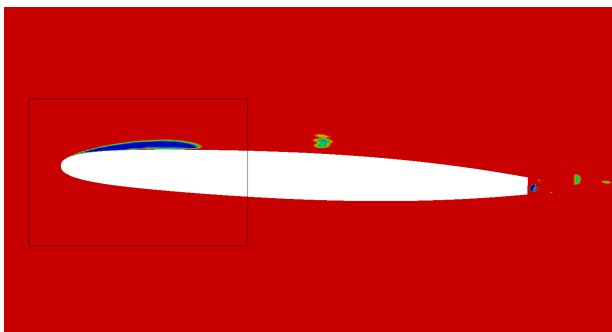
t = 0.14 s
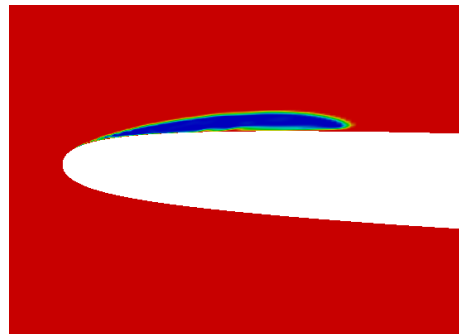
t = 0.142 s
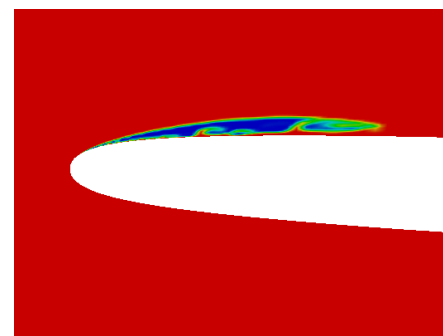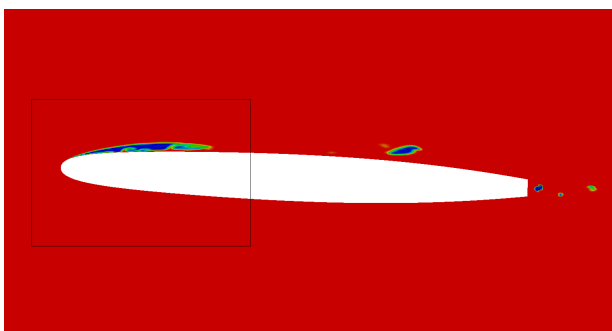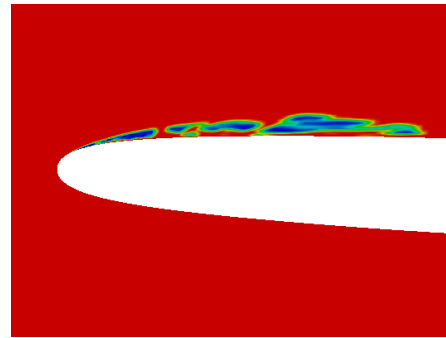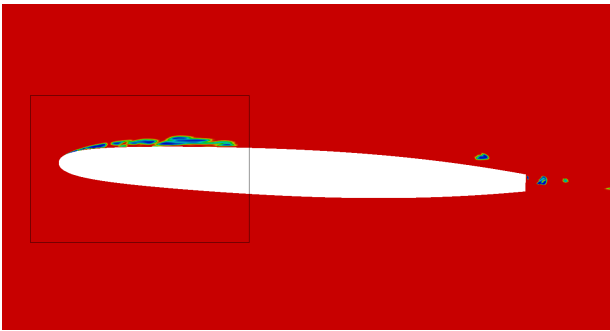
$$t = 0.144 \text{ s}$$

$$t = 0.146 \text{ s}$$

$$t = 0.148 \text{ s}$$

t = 0.15 s

t = 0.152 s
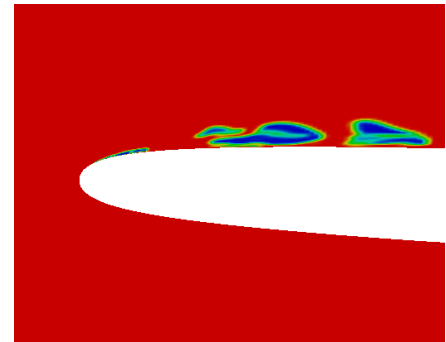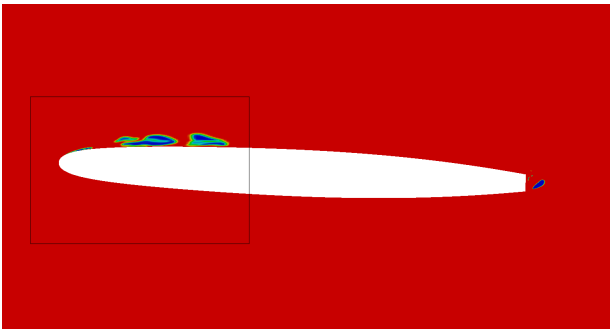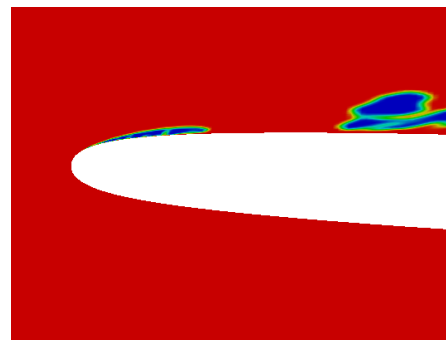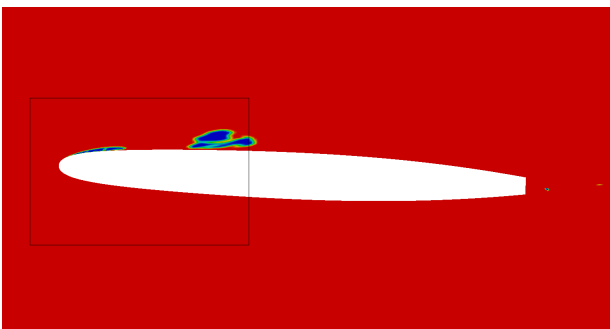
t = 0.154 s
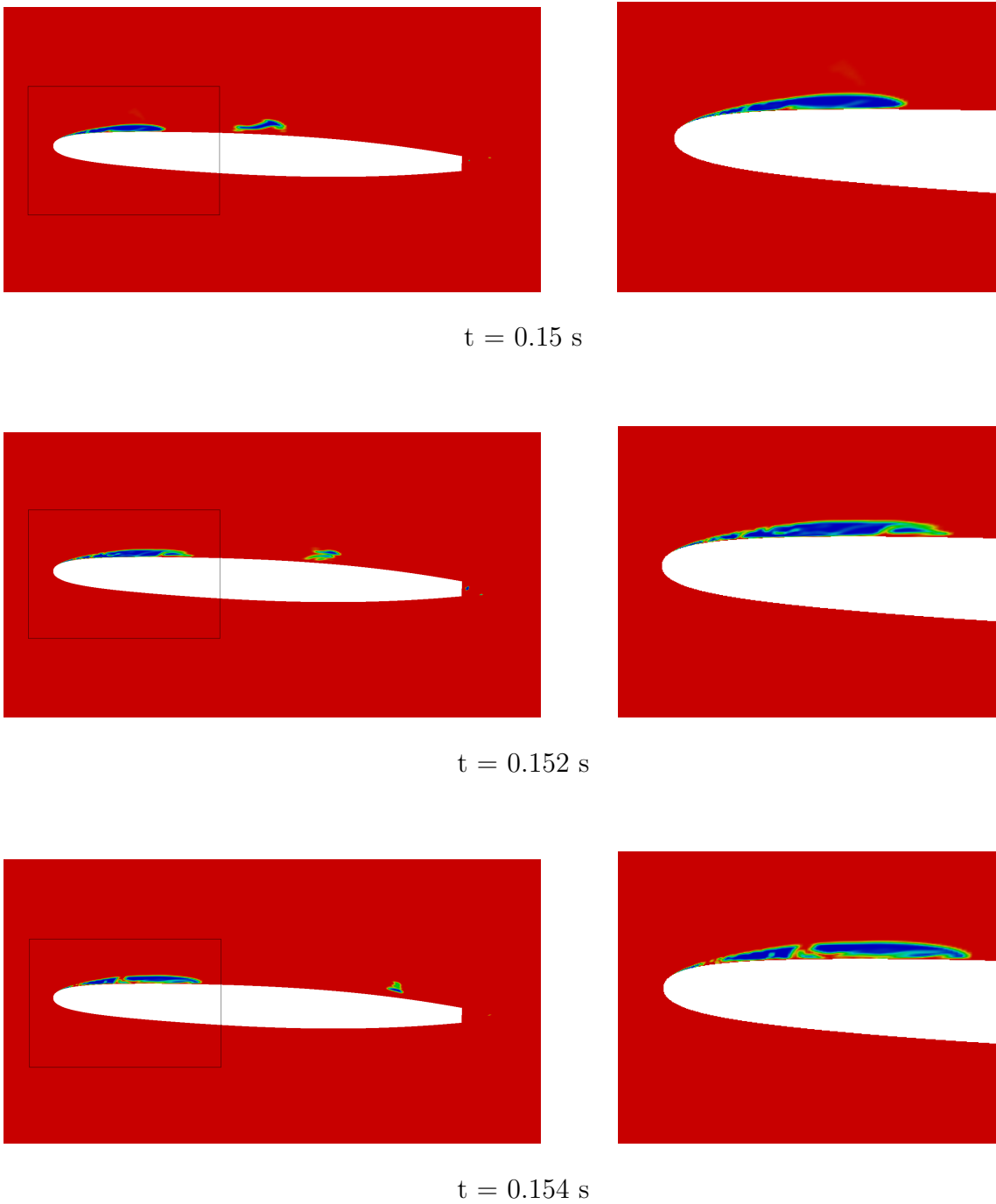
Figure 5.4: Sheet cavity behavior in a NACA009 laminar flow simulation.

The time frame shown in Fig. 5.4 is equal to 0.014 seconds meaning that the frequency of the vapor shedding is extremely high.

The turbulent flow conditions produced a somewhat different image as seen in Fig. 5.5
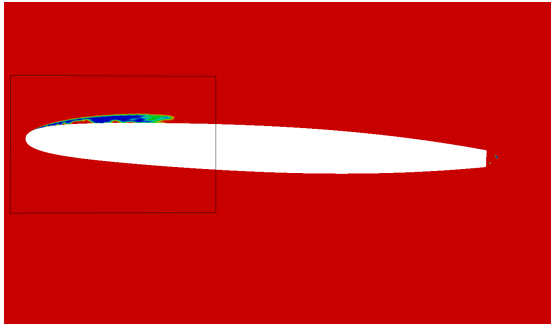
t = 0.8 s
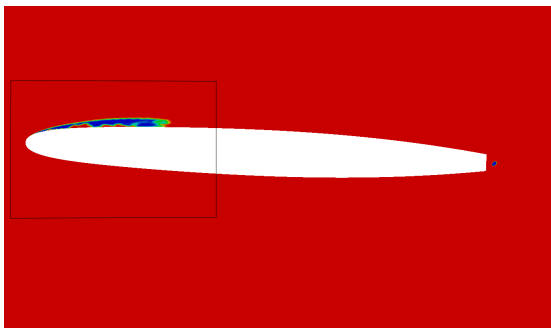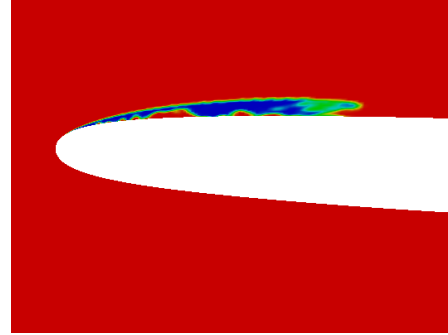
t = 0.85 s
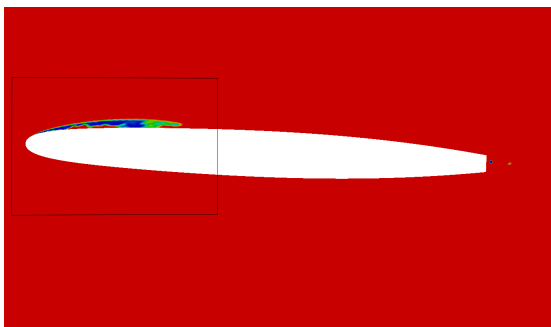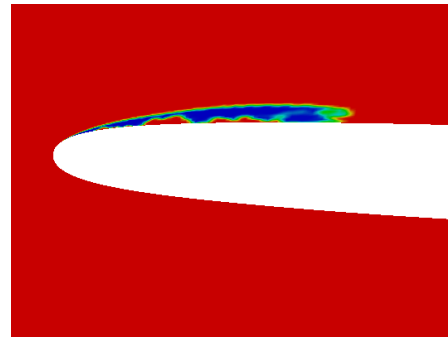
t = 0.9 s

t = 0.95 s
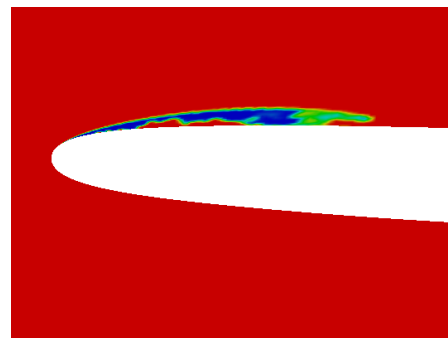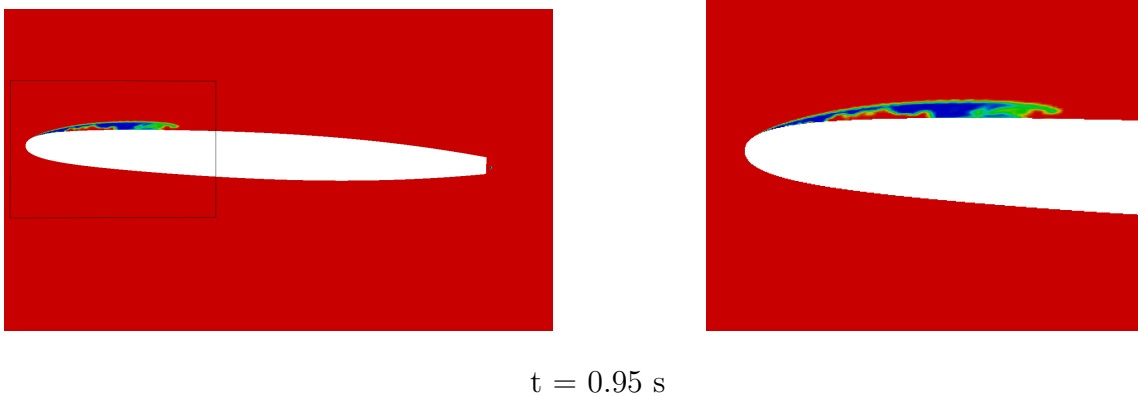
Figure 5.5: Sheet cavity behavior in a NACA009 turbulent flow simulation.

Although both Fig. 5.4 and Fig. 5.5 show a similar duration in time, Fig. 5.5 doesn't show any vapor shedding. Also, the vapor bubbles at the trailing edge are much more uniform and occur in regular intervals, but dissolve very quickly.

In order to compare the results of different flow conditions, the values in the flow were averaged over time. However, as mentioned in Chapter 2, transient solvers attempt to calculate a correct solution for each time step, but this means that the first time step takes a lot of time to solve. This is because the first time step calculates the values based on the initial conditions of the flow, and it is very difficult to set the initial conditions close to a correct solution. To alleviate the stress on the solver, the correct solution is not required in the first couple of time steps, but instead the solution will converge in time to a correct one and from that time step on each new time step will give a correct image of the flow. Using this knowledge, the first couple of solutions were disregarded in the averaging, and the values were averaged over the time frame between 0.05 seconds and 0.2 seconds. The Fig. 5.6 shows the average vapor cavity position in the simulation without turbulence modeling.
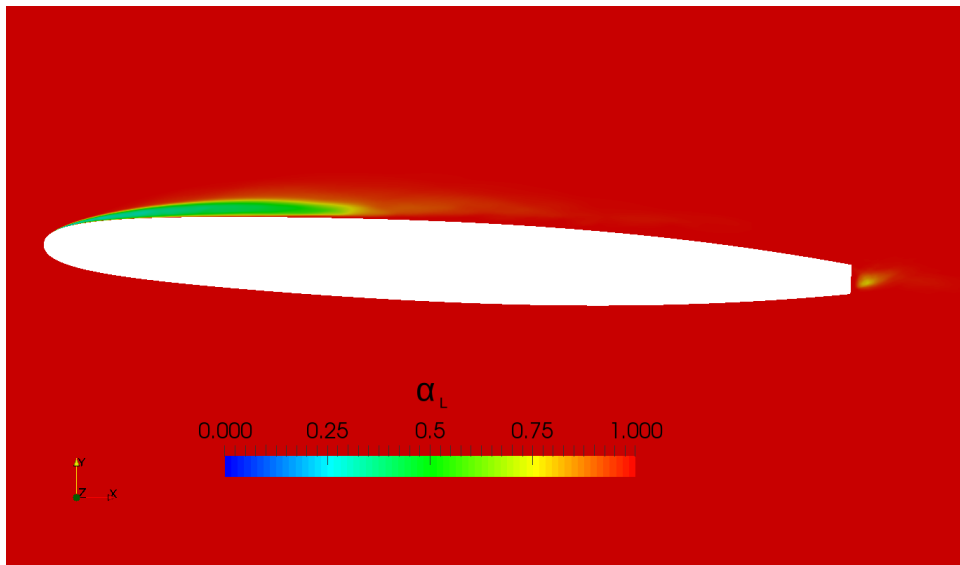
Figure 5.6: Average vapor fraction distribution around the NACA009 Hydrofoil for a laminar flow ($u = 20$ m/s).

The vapor distribution is actually represented by the liquid fraction ration α_l, meaning that the absence of the liquid phase, represents the vapor phase. The smearing is present, because the vapor cavities constantly form, detach and travel downstream.

In comparison, the average result for the turbulent flow simulation is more focused. The behavior of the vapor cavities is less violent and the results in Fig. 5.7, reflect the observations made from Fig. 5.5.
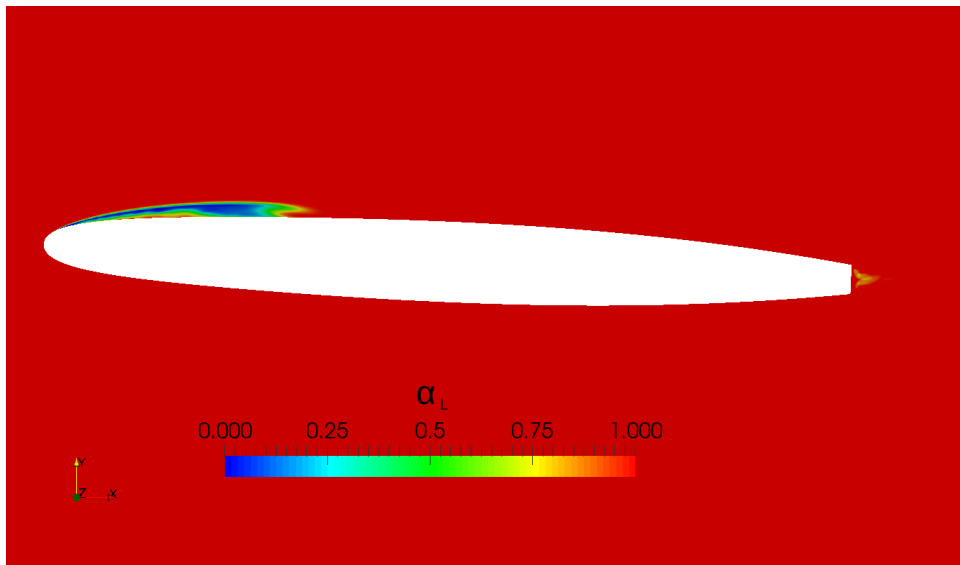
Figure 5.7: Average vapor fraction distribution around the NACA009 Hydrofoil for a turbulent flow ($u = 20$ m/s).

Both the laminar flow and the turbulent flow images show similar size cavities to the experimentally derived results from [5].
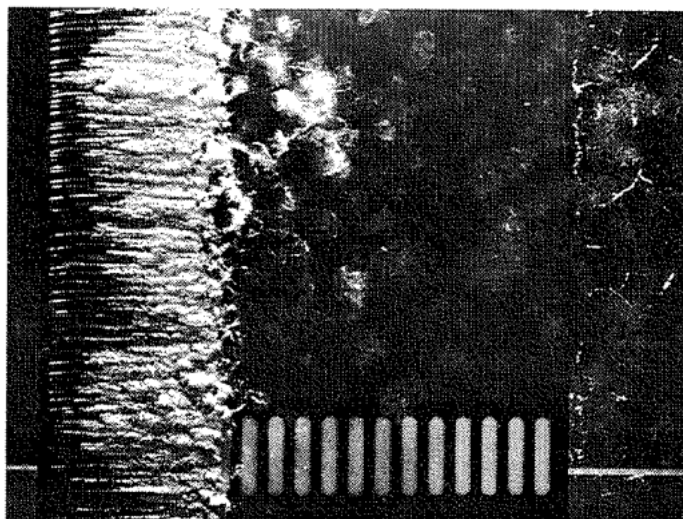
Figure 5.8: Photograph of a sheet vapor cavity on the NACA009 foil [5].
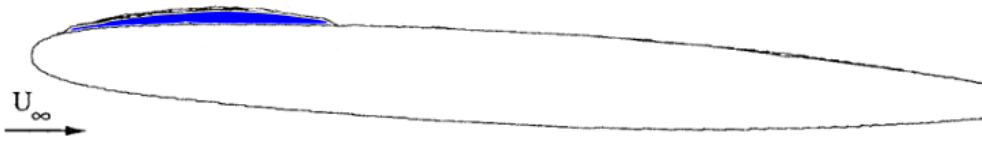
Figure 5.9: Measurement of the sheet vapor cavity on the NACA009 foil [5].

Comparing the images for the average vapor cavity position for the turbulent flow in Fig. 5.7 and the experimental measurement in Fig. 5.9, the size of the cavity is almost identical. As for the laminar flow, the average vapor cavity position from Fig. 5.6, shouldn't be used as a criterion of comparison to the experimental results. The transient images of the sheet cavity in Fig. 5.4, however, show a similar size cavity to the experimental results.

The pressure and velocity distribution around the foil is shown in the following figures.
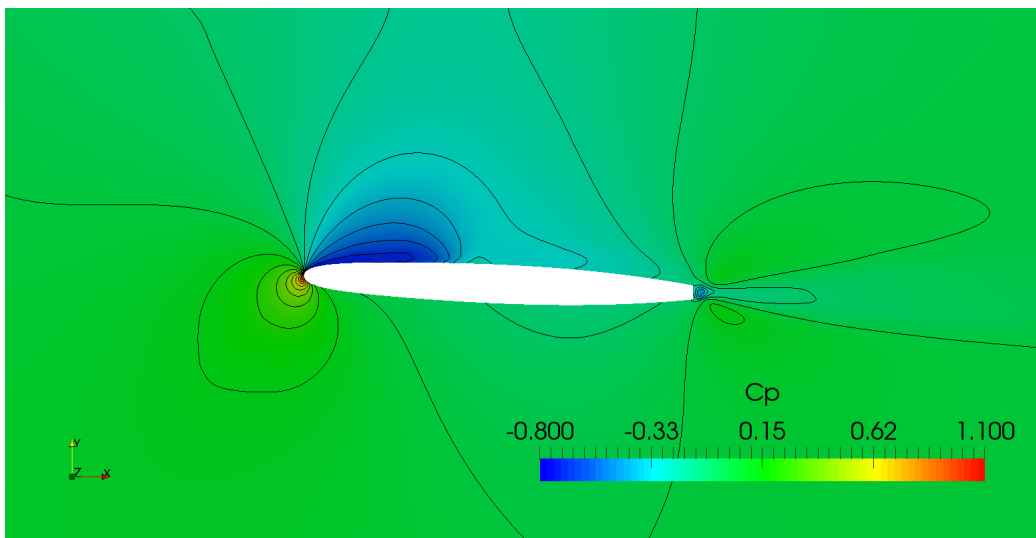
Figure 5.10: Pressure distribution around the NACA009 foil in a laminar cavitating flow ($u = 20$ m/s).
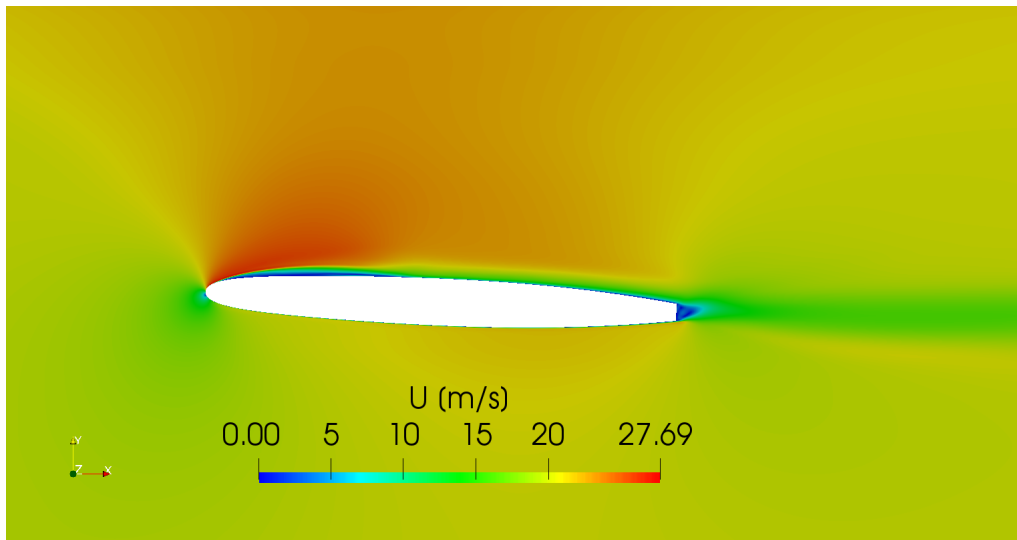
Figure 5.11: Fluid velocity around the NACA009 foil in a laminar cavitating flow ($u = 20$ m/s).

And for the turbulent cavitating flow:
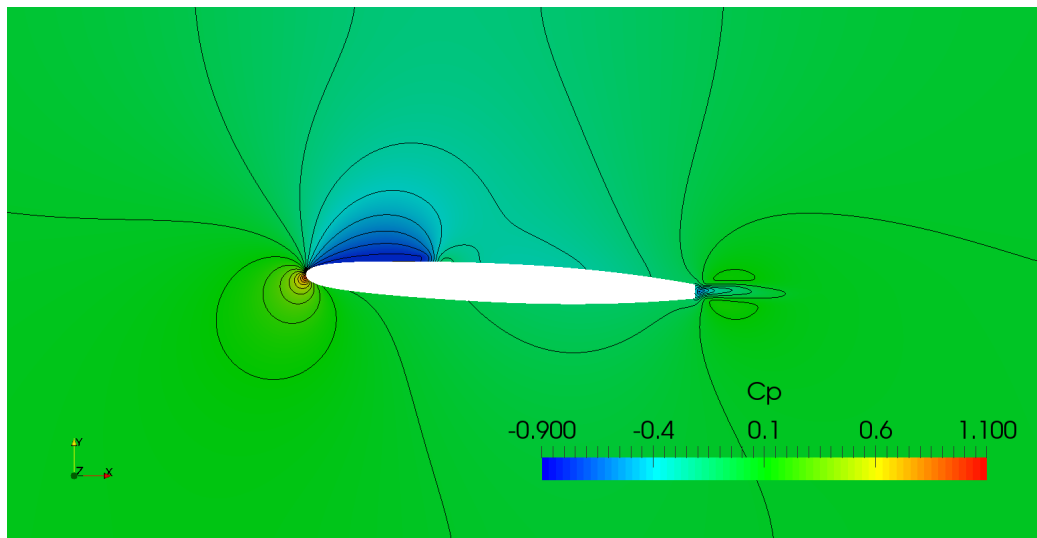
Figure 5.12: Pressure distribution around the NACA009 foil in a turbulent cavitating flow ($u = 20$ m/s).
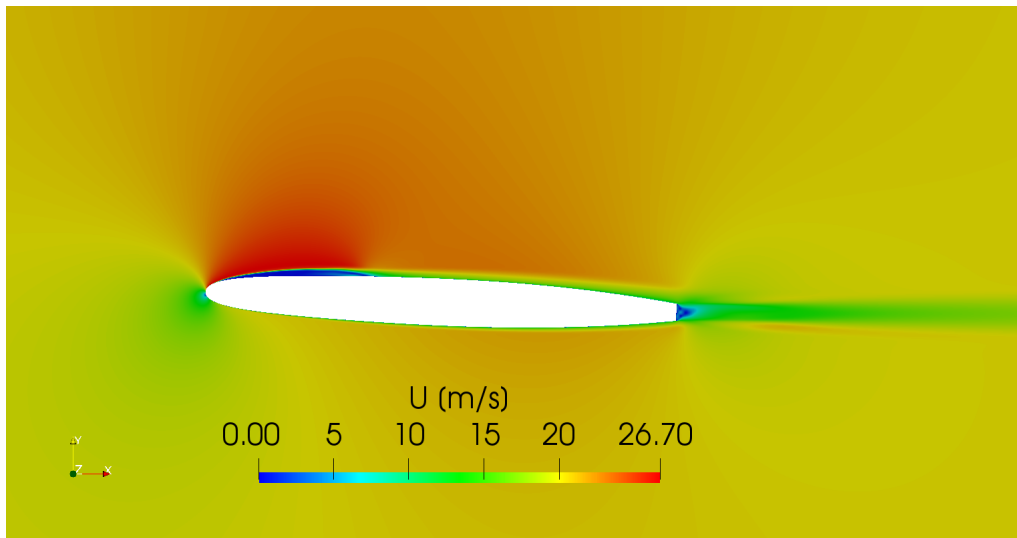
Figure 5.13: Fluid velocity around the NACA009 foil in a turbulent cavitating flow ($u = 20$ m/s).

The cavitation images for the flow velocity $u = 30$ m/s, are similar to the ones that were shown, with the differences between the laminar and turbulent flow being identical to those that were already presented. With that in mind, the vapor cavity images for the increased flow velocity, will be skipped over.

The pressure distribution on the wing as expected mimics the areas where the cavities occur.
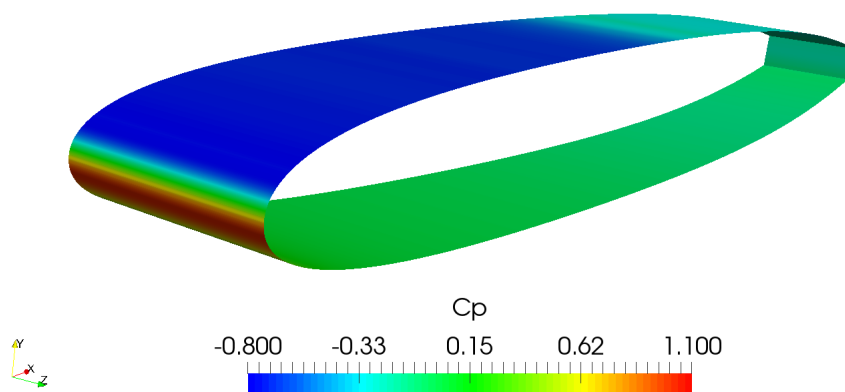
Figure 5.14: Pressure distribution on the NACA009 foil in a cavitating flow.

Comparing to the results from Fig. 5.3, the low pressure area near the leading edge of the wing is longer. Once cavitation begins manifesting, it begins to represent an obstacle for the flow, which causes this low pressure area to expand. In Fig 5.3, the pressure distribution measurements are shown in comparison to the measurements from [5].
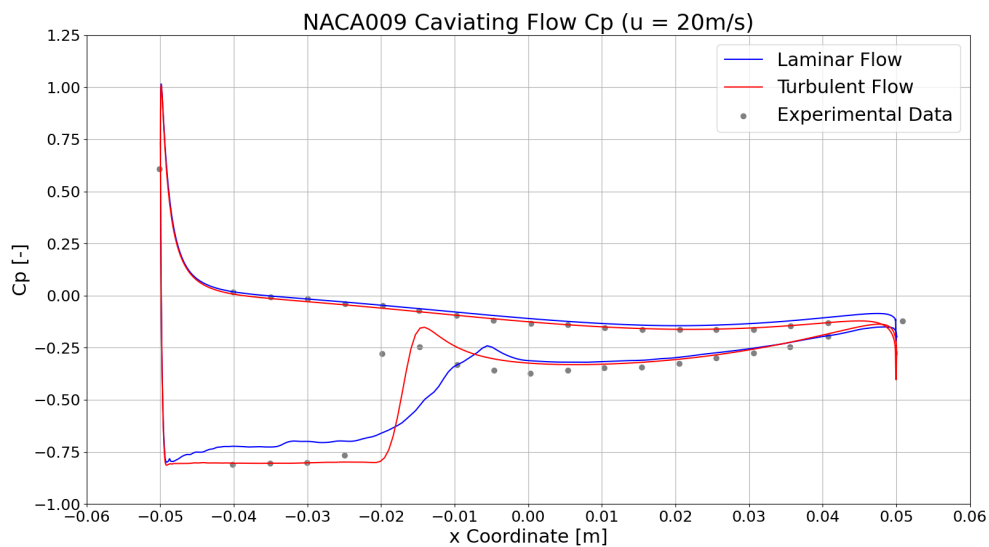
Figure 5.15: NACA009 cavitating flow C_P validation ($u = 20$ m/s).

On the pressure side of the foil, both the turbulent and laminar flow results, match the experimental results, however on the suction side, the results diverge. The turbulent flow better approximates the curve of the experimental results, but neither model is a prefect fit. The pressure distribution in the turbulent flow is steadier, which corresponds to the vapor cavity behavior. The steep climb of the pressure, downstream of the cavity is likely due to the increased diffusion from the turbulence.

For context, the pressure distribution can be compared to the non-cavitating flow simulation results.
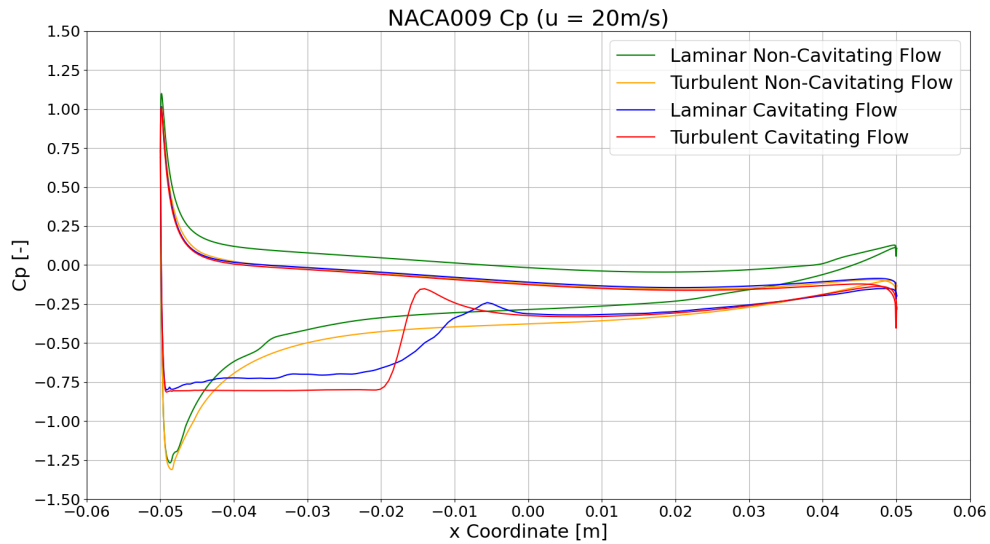
Figure 5.16: NACA009 foil C_P comparison ($u = 20$ m/s).

It can be observed that the laminar non-cavitating flow diverges from the other results, on the pressure side of the foil. This may stem from the averaging of the results, in the `simpleFoam` simulations, being physically incorrect.

For the flow velocity $u = 30$ m/s, the pressure distribution results are the following:
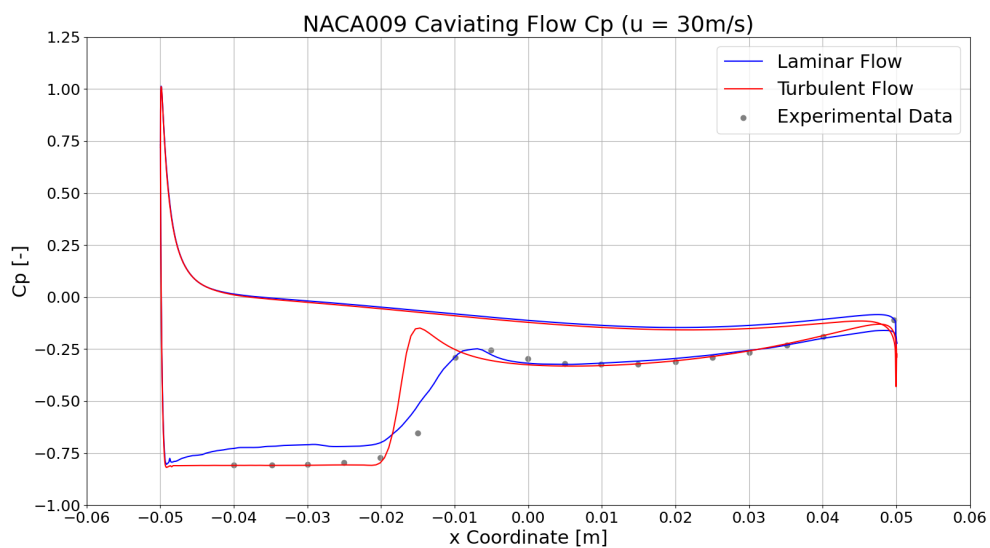
Figure 5.17: NACA009 cavitating flow C_P validation ($u = 30$ m/s).

For the increased flow velocity, the pressure distribution is better modeled by the laminar flow.

When compared to the non-cavitating flow simulation results:
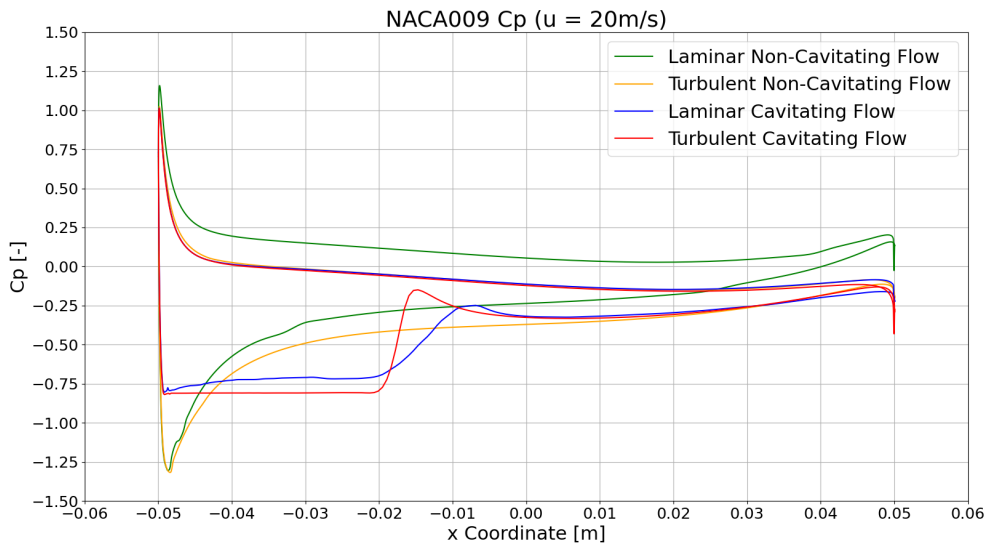
Figure 5.18: NACA009 foil C_P Comparison ($u = 30$ m/s).

Again, the non-cavitating laminar flow diverges from other results.

In addition to the pressure distribution, the lift and drag coefficients of the wing were measured. The following figures present the lift and drag coefficient values in a time frame from 0.05 to 0.1 seconds.
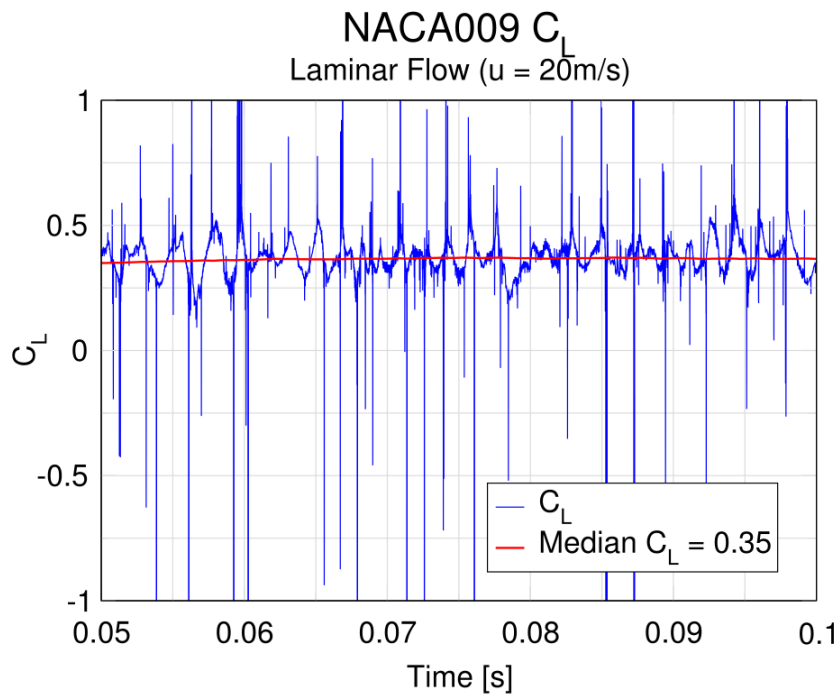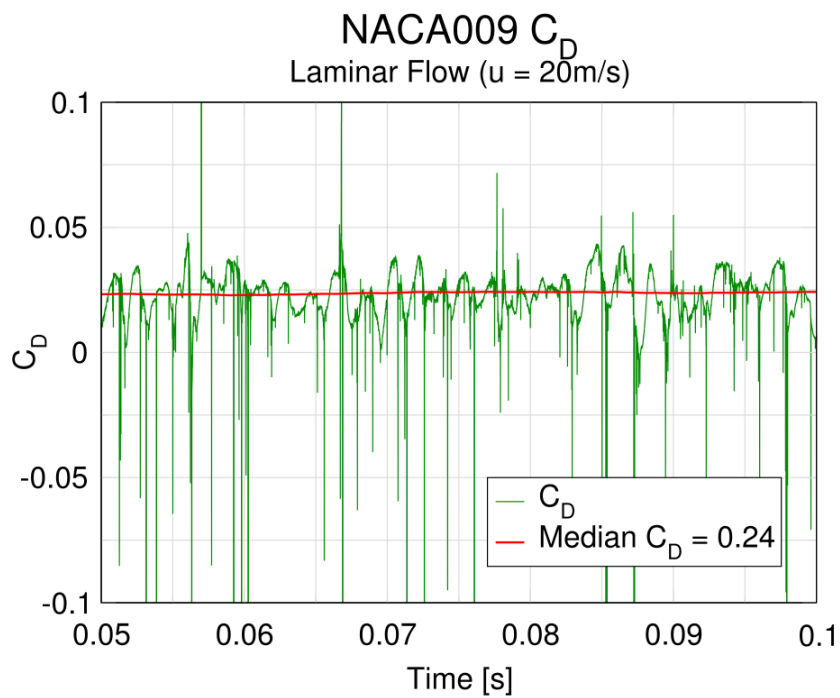
Figure 5.19: NACA009 laminar flow C_L ($u = 20$ m/s).
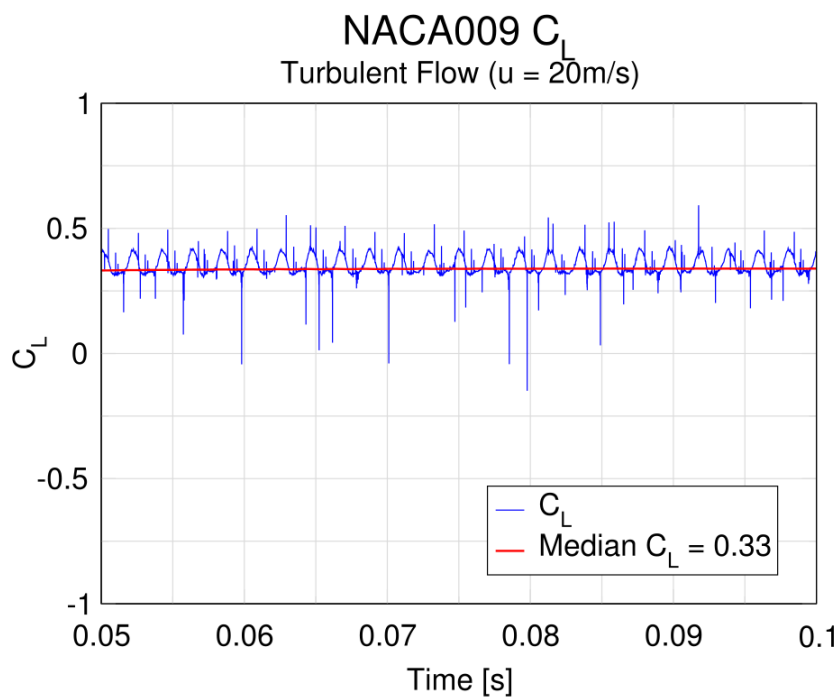
Figure 5.20: NACA009 turbulent flow C_L ($u = 20$ m/s).

Fig. 5.19 and Fig. 5.20 show the variation of the lift force on the foil in time. The laminar flow produces a very irregular signal. The high amplitude spikes in the signal represent vapor cavity implosions, while the lower amplitudes could represent the cavity detachment. The signal models a very stochastic behavior, which is in accordance with the nature of cavitation. Also it can be observed that the frequency of the cavitation detachment is very high, which is seen on Fig. 5.4. On the other hand, the turbulent flow produces a much more regular signal.

The drag coefficient graphs are very similar to the lift coefficient ones, albeit on a different scale.

Figure 5.21: NACA009 laminar flow C_D ($u = 20$ m/s).
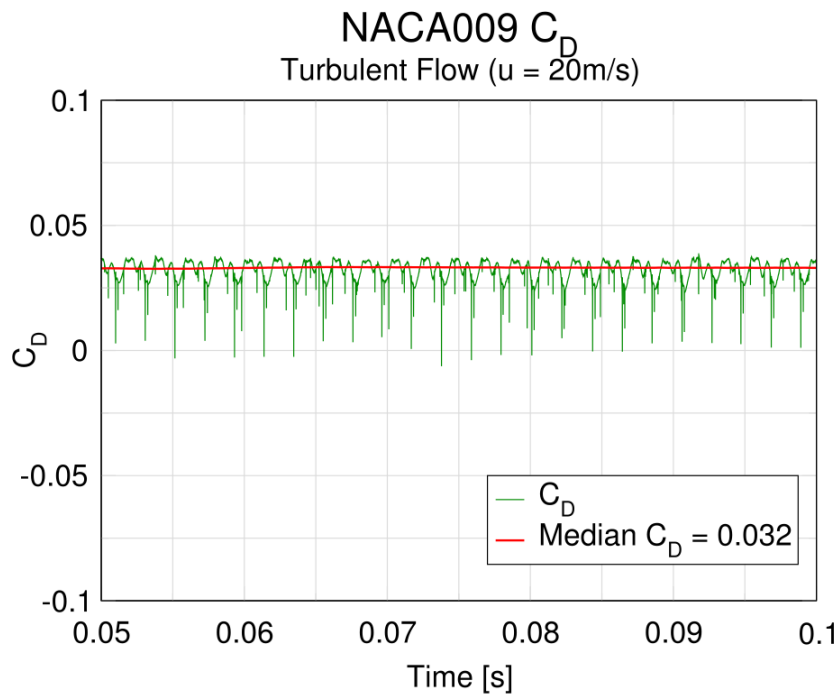
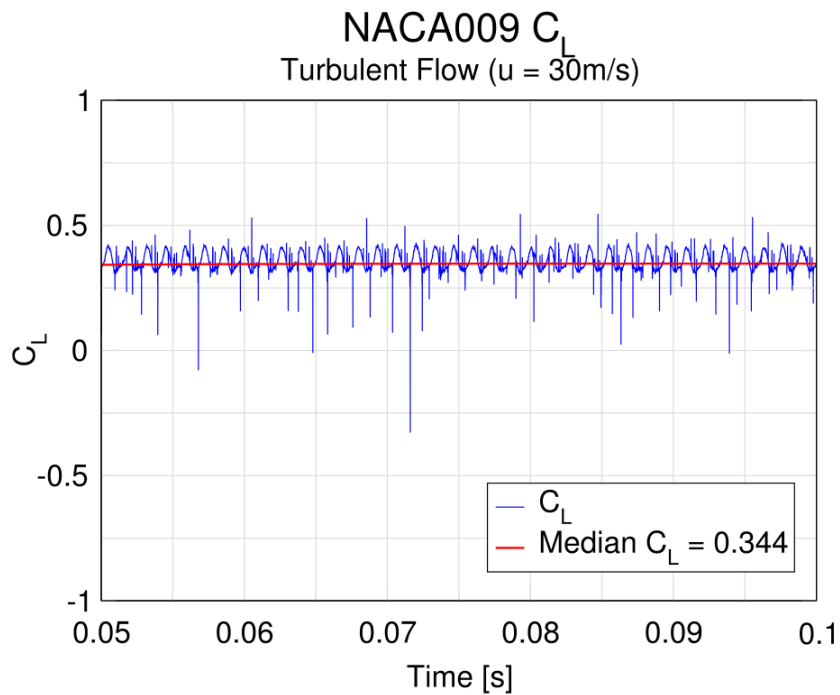Figure 5.22: NACA009 turbulent flow C_D ($u = 20$ m/s).

The results may be compared to the non-cavitating flow values:

Table 5.2: Lift and Drag coefficient values of the NACA009 non-cavitating flow simulations

	NACA009 C_L, C_D	
	Laminar Flow	Turbulent Flow
C_L	0.36	0.34
C_D	0.005	0.02

The drag coefficient is significantly different for both the laminar and the turbulent flows. For the laminar flow, the drag force is five times higher with the occurence of cavitation, and the lift force lower.

For the increased flow velocity, the cavitating flow results are of a similar nature.
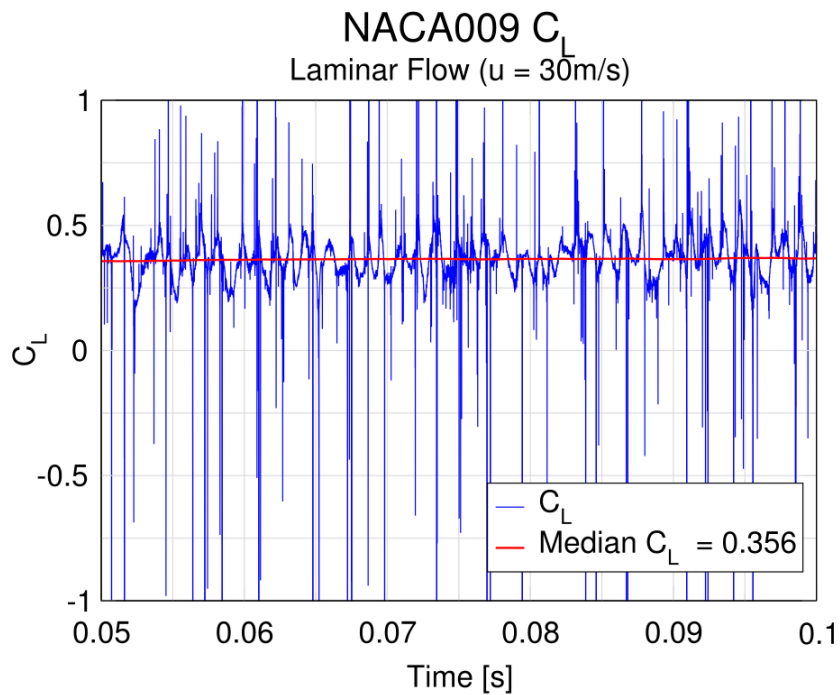
Figure 5.23: NACA009 laminar flow C_L ($u = 30$ m/s).

Figure 5.24: NACA009 turbulent flow C_L ($u = 30$ m/s).
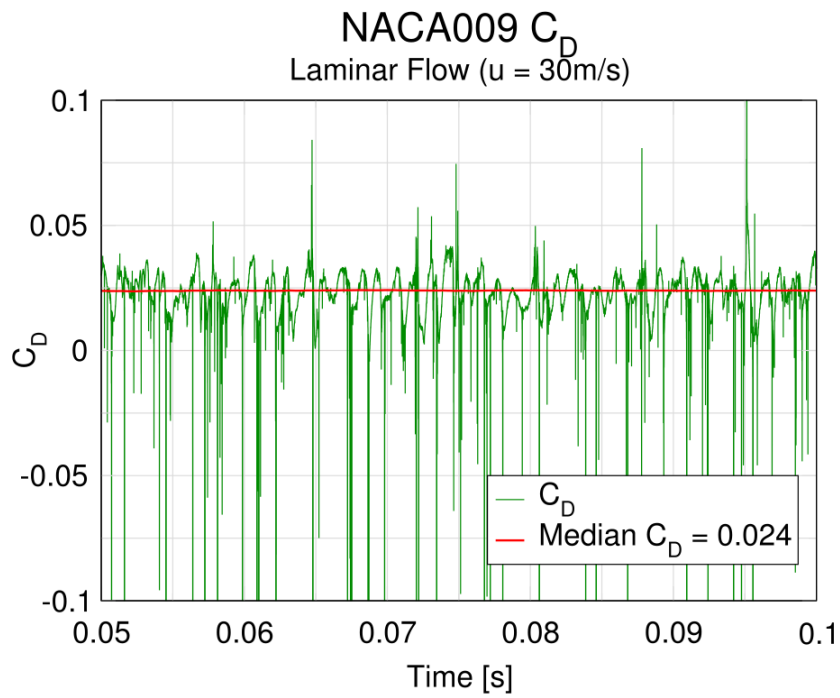
Figure 5.25: NACA009 laminar flow C_D ($u = 30$ m/s).
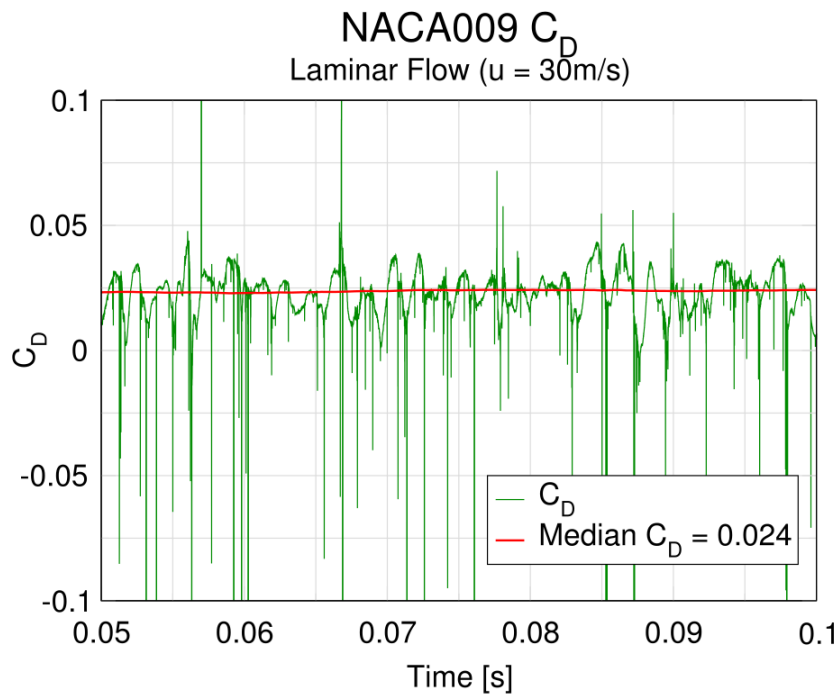
Figure 5.26: NACA009 turbulent flow C_D ($u = 30$ m/s).

Interestingly, the median values for the coefficients are very similar with respect to the presence of turbulence, even though Fig. 5.24 shows that the frequency of the cavitation shedding has increased.

5.3.   Delft Twist 11 Hydrofoil

This section will present the results of the simulations performed on the Delft Twist 11 Hydrofoil. As with the NACA009 results, the focus will be on the cavitating flow simulation.

5.3.1.   Non-cavitating Flow

As with the NACA009 `simpleFoam` simulations, the solutions turned out to be semi-transient. For a further explanation of this phenomenon, the NACA009 Truncated Hydrofoil Section of this Chapter can be referenced. In order to compare the results of the simulations, the values were averaged over the time steps. The low pressure distribution on the foil can serve as prediction of the area where cavitation should occur.
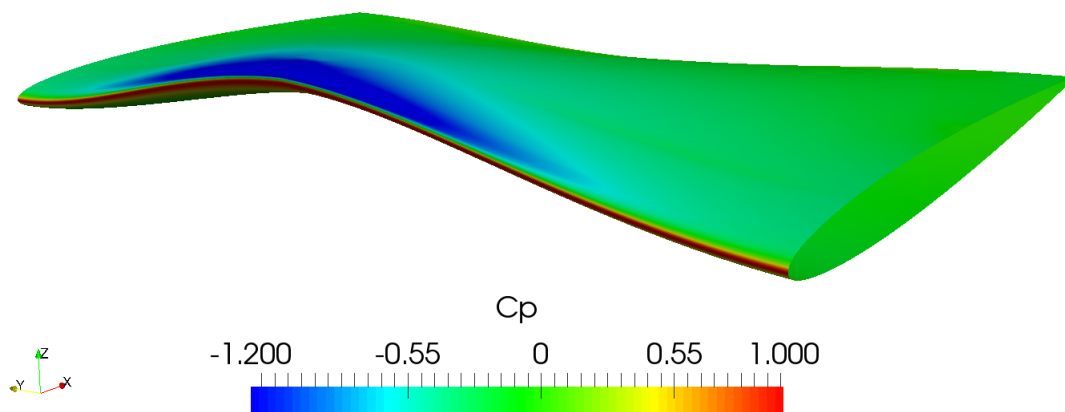

Figure 5.27: Delft Twist 11 non-cavitating flow pressure distribution.

As with the NACA009 results, other non-cavitating flow results will be presented only if needed to compare to the cavitating flow results.

5.3.2. Cavitating Flow

The simulations of the cavitating flow around the Delft Twist 11 Hydrofoil were executed as transient simulations for a time frame of about 0.18 seconds. To speed up the computing process, parallel computing using multi-core processors was applied.

Table 5.3: Delft Twist 11 cavitating flow simulations CPU demand.

| Delft Twist 11 Cavitating Flow Simulation Information					
Flow Conditions	Machine CPU	Number of Parralel Processes	Simulated Time [s]	Average Time Step Size [s]	Simulation CPU Time
Laminar	Intel(R) Core(TM) i7-7800X CPU @ 3.50GHz	6	0.19	$6 \cdot 10^{-6}$	116h 42' 2"
Turbulent	Intel(R) Core(TM) i5-3570K CPU @ 3.40GHz	4	0.18	$4 \cdot 10^{-6}$	291h 43' 17"

In both the laminar and turbulent flow, sheet cavitation emerged around the the midspan point, as indicated by the pressure distribution on the foil in the non-cavitating flow simulations.
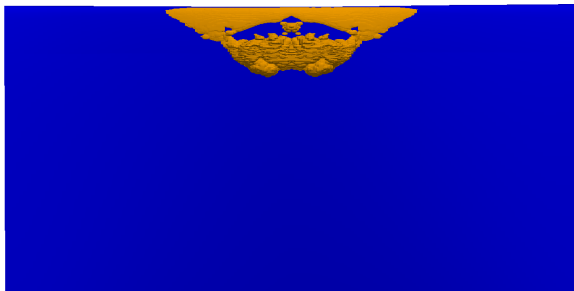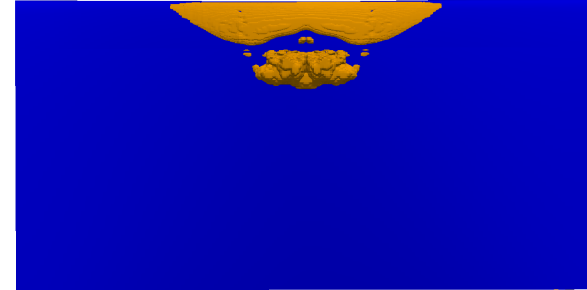

t = 0.1100 s
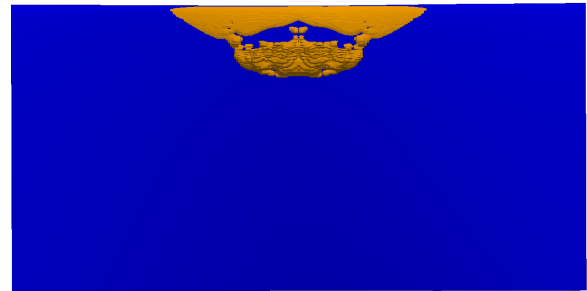
t = 0.1112 s

t = 0.1124 s

t = 0.1136 s

<div align="center">

t = 0.1148 s   t = 0.1160 s
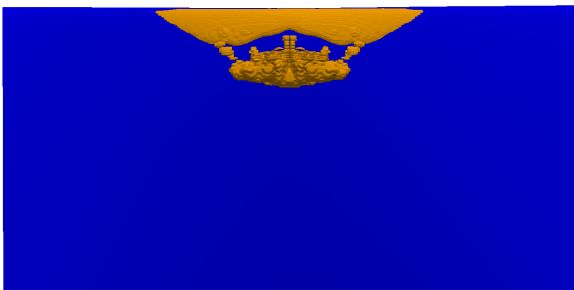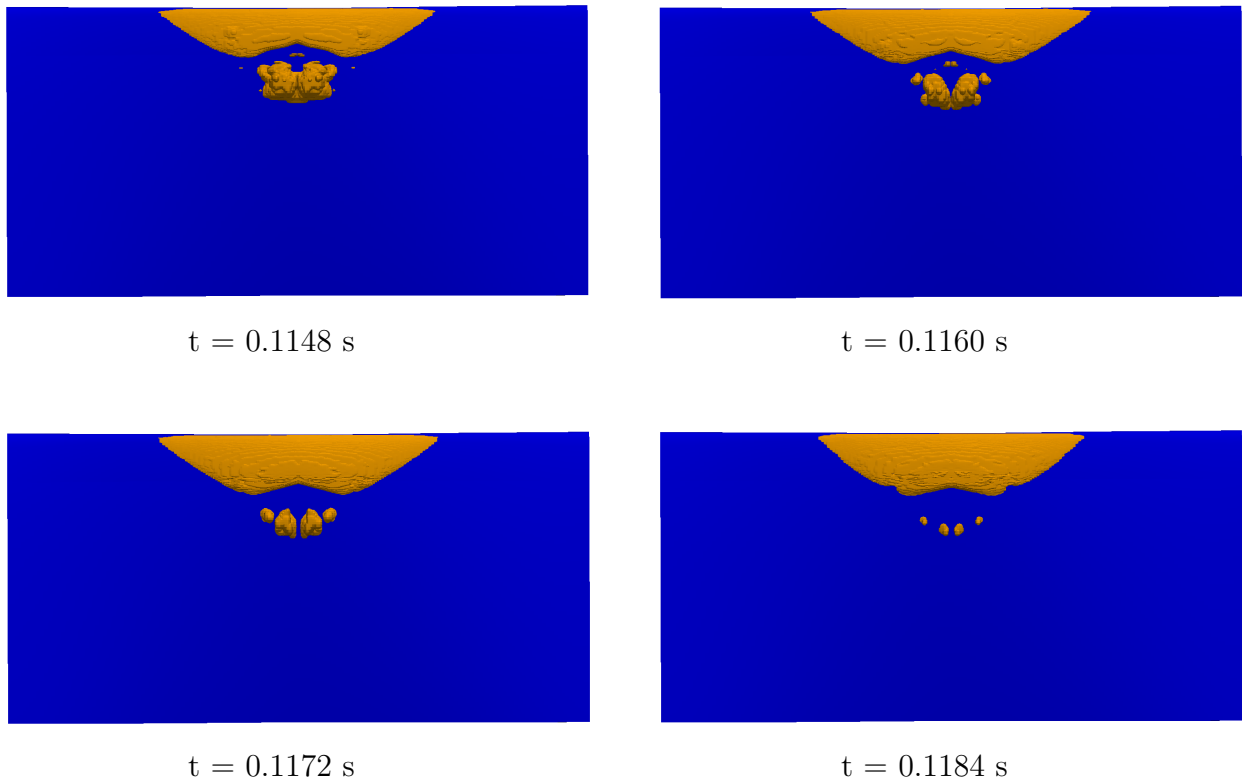
t = 0.1172 s   t = 0.1184 s

</div>

Figure 5.28: Sheet cavity behavior in a Delft Twist 11 laminar flow simulation.

The images depict the shedding of the vapor cavity and the motion of the detached bubble downstream. A large attached sheet cavity forms, and then the liquid phase flow reverses and divides the cavity. This cavitation behavior is physically correct and is confirmed and modeled by [6] and shown in Fig. 5.29. It should also be noted that, compared to the NACA009 cavity shedding seen in Fig. 5.4, the detached cavity does not travel very far downstream, however it is difficult to compare these results because of the differences in the σ_{cav} and the hydrofoil geometry.
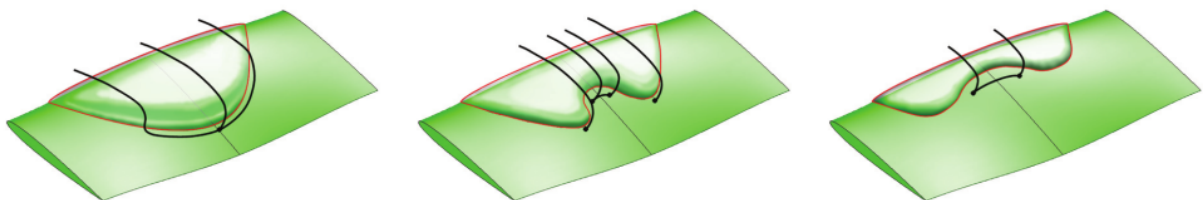

Figure 5.29: Cavitation shedding model [6].

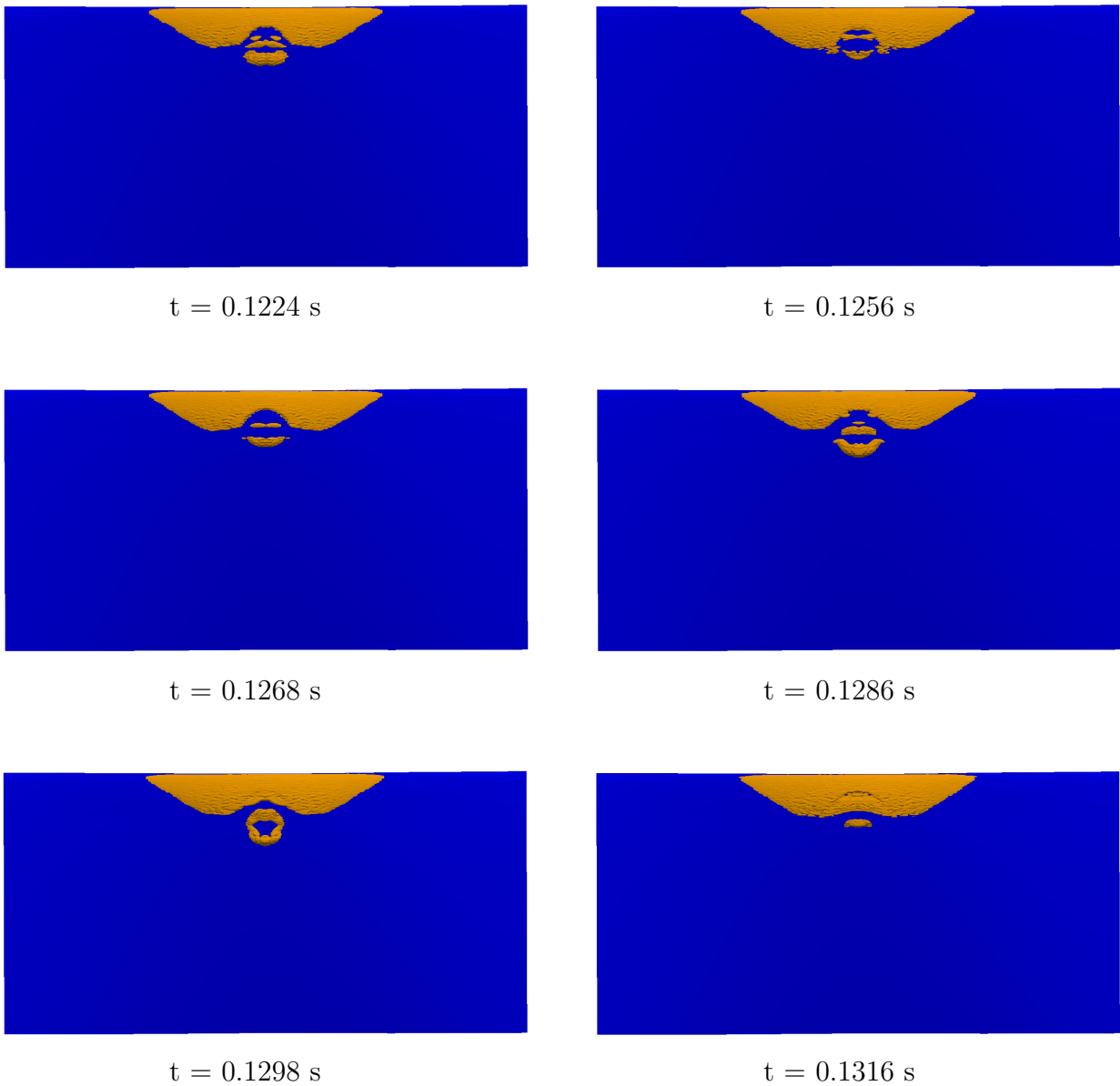For the turbulent flow simulations, the cavity shedding looks different.

<table>
<tr><td>t = 0.1224 s</td><td>t = 0.1256 s</td></tr>
</table>

t = 0.1224 s   t = 0.1256 s

t = 0.1268 s   t = 0.1286 s

t = 0.1298 s   t = 0.1316 s

Figure 5.30: Sheet cavity behavior in a Delft Twist 11 turbulent flow simulation.

While the horseshoe shape of the cavity, after shedding, fits the model depicted in Fig. 5.29 even better then the laminar flow results, the full evolved attached cavity doesn't ever form in the turbulent flow. Instead the cavitation is constantly shedding, and the attached cavity is an almost perpetual horseshoe state.

When compared to the experimental results from [6] and LES simulation results from [7], the results show some similarities in the shape of both the attached cavity and the detached bubble to the results from the laminar flow simulations.
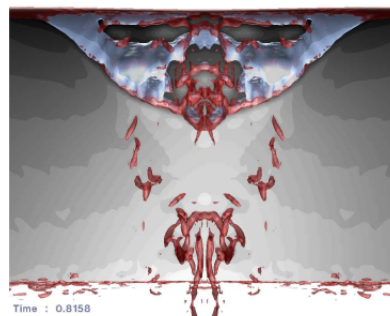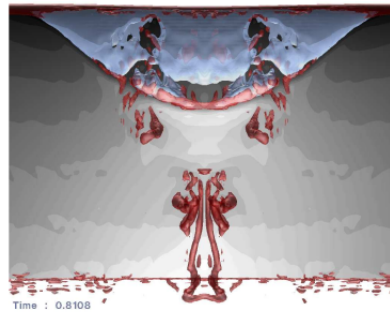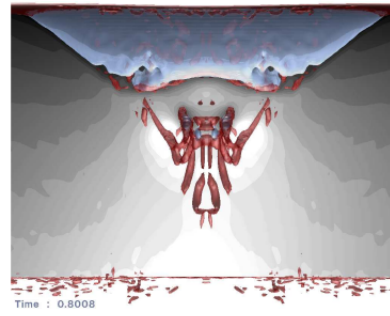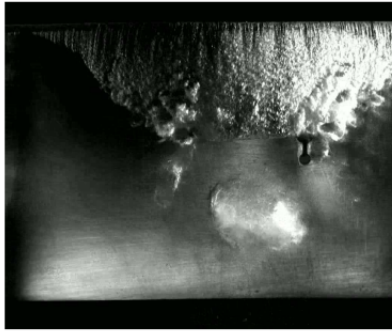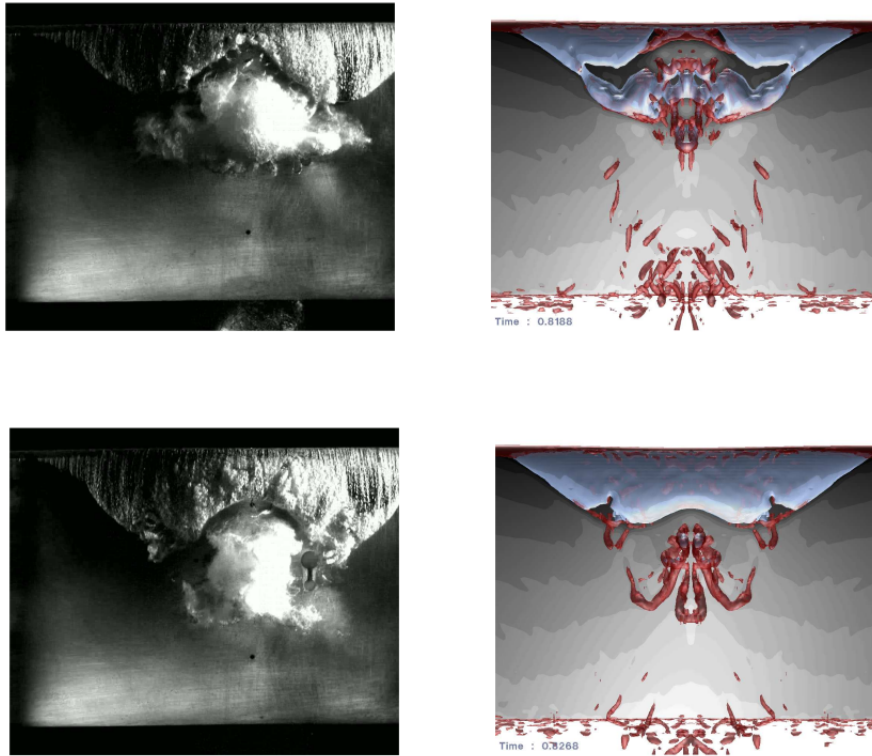
Figure 5.31: Experimental (left) [6] and LES (right) [7] cavitation shedding results.

To compare the results of the cavitating flow simulations, as in the case of the NACA009 simulations, the results were averaged over the time. The following figures show the average vapor cavity position, fluid velocity and pressure distribution, during the time frame from 0.08 seconds to 0.18 seconds.
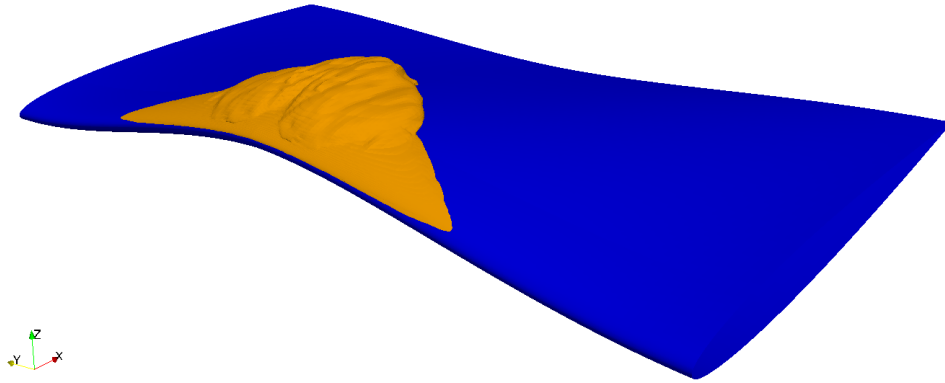
Figure 5.32: Average vapor fraction distribution around the Delft Twist 11 hydrofoil for a laminar flow.
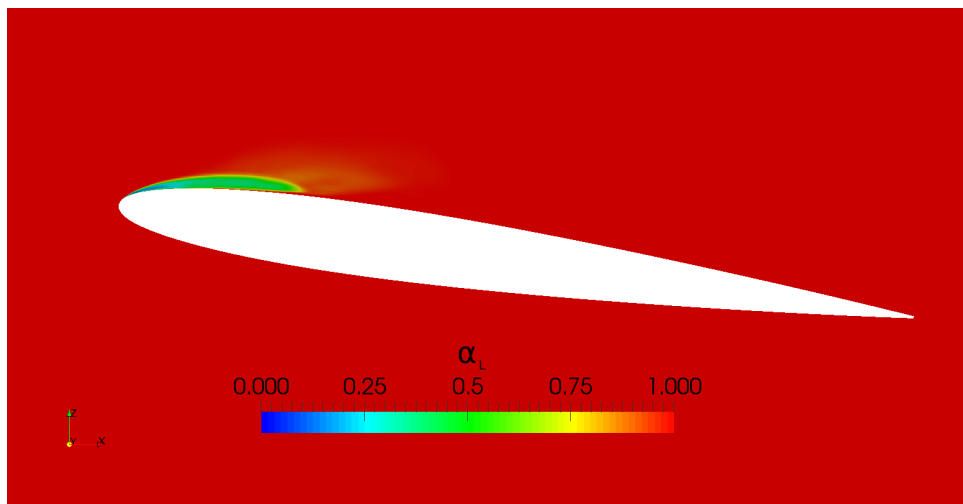

Figure 5.33: Average vapor fraction distribution around the midspan section of the Delft Twist 11 hydrofoil for a laminar flow.

Figure 5.34: Average pressure distribution around the midspan section of the Delft Twist 11 hydrofoil for a laminar flow.

Figure 5.35: Average fluid velocity distribution around the midspan section of the Delft Twist 11 hydrofoil for a laminar flow.

As for the turbulent flow:
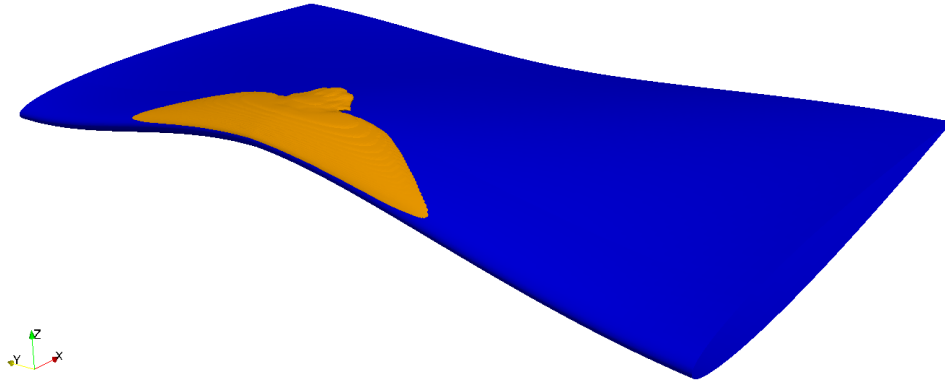
Figure 5.36: Average vapor fraction distribution around the Delft Twist 11 hydrofoil for a turbulent flow.
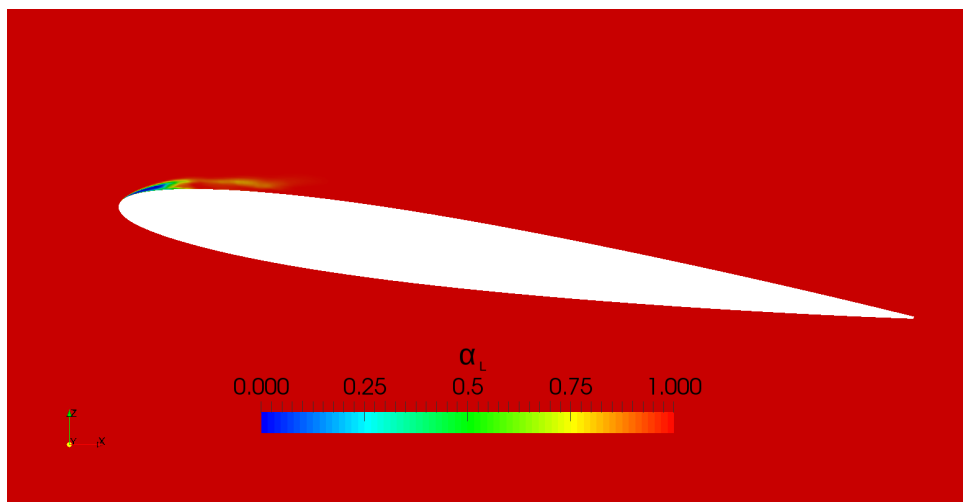
Figure 5.37: Average vapor fraction distribution around the midspan section of the Delft Twist 11 hydrofoil for a turbulent flow.
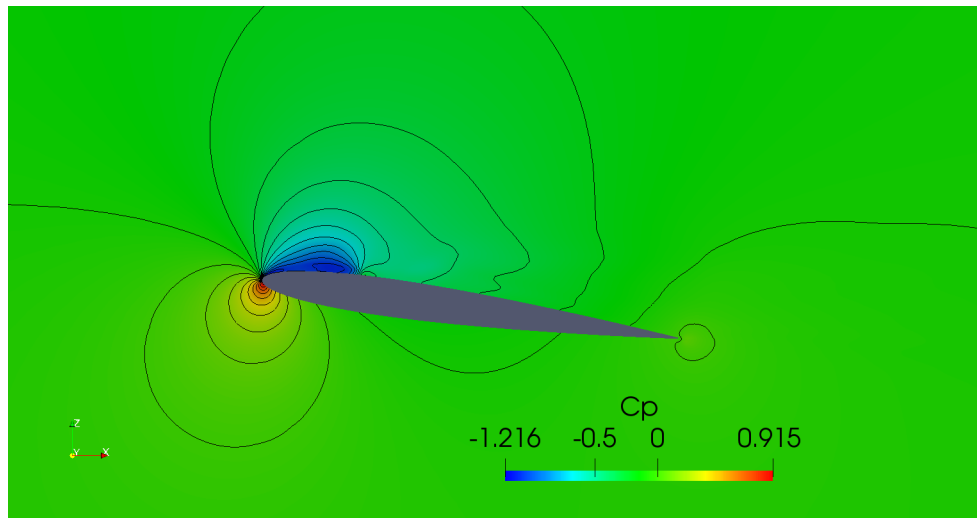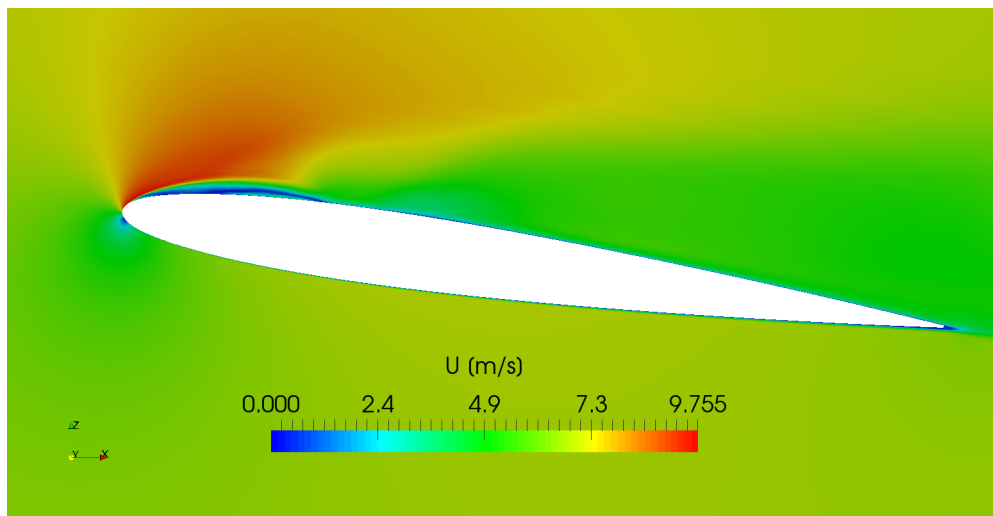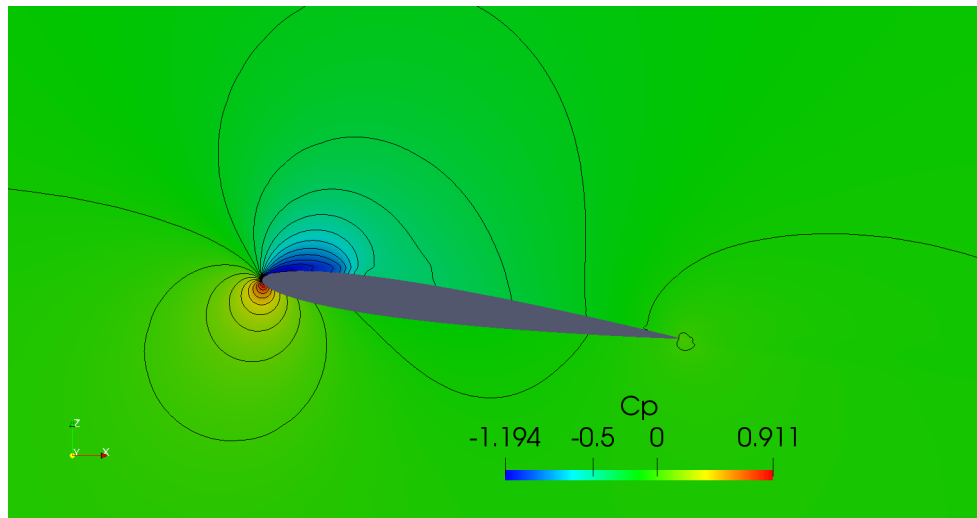
Figure 5.38: Average pressure distribution around the midspan section of the Delft Twist 11 hydrofoil for a turbulent flow.
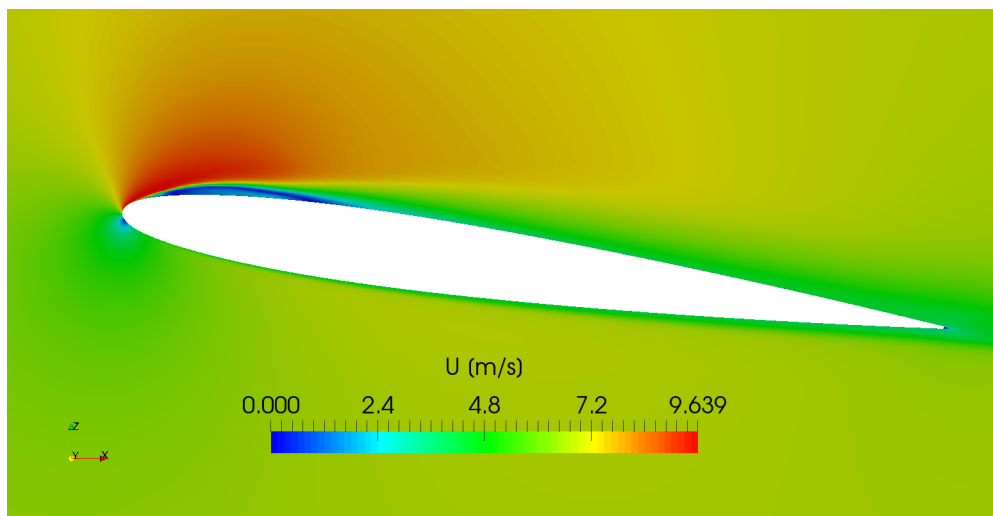
Figure 5.39: Average fluid velocity distribution around the midspan section of the Delft Twist 11 hydrofoil for a turbulent flow.

As the transient flow images suggested, the attached cavity is far larger in the laminar flow. Also, Fig. 5.36 shows, that the detached bubble in the turbulent flow stays much closer to the foil then in the laminar flow. This is even more evident when comparing the velocity distribution in Fig. 5.35 and Fig. 5.39. It also seems that just as in the case of the NACA009 simulations, the increased diffusivity, inhibits the growth of the vapor

cavity. The difference in the pressure distribution in 5.34 and Fig. 5.38 also illustrates the difference in the behavior of the flows. The laminar flow is much more irregular then the turbulent flow. This will be further discussed in force measurement section.

The pressure distribution was measured over the midspan section of the hydrofoil.
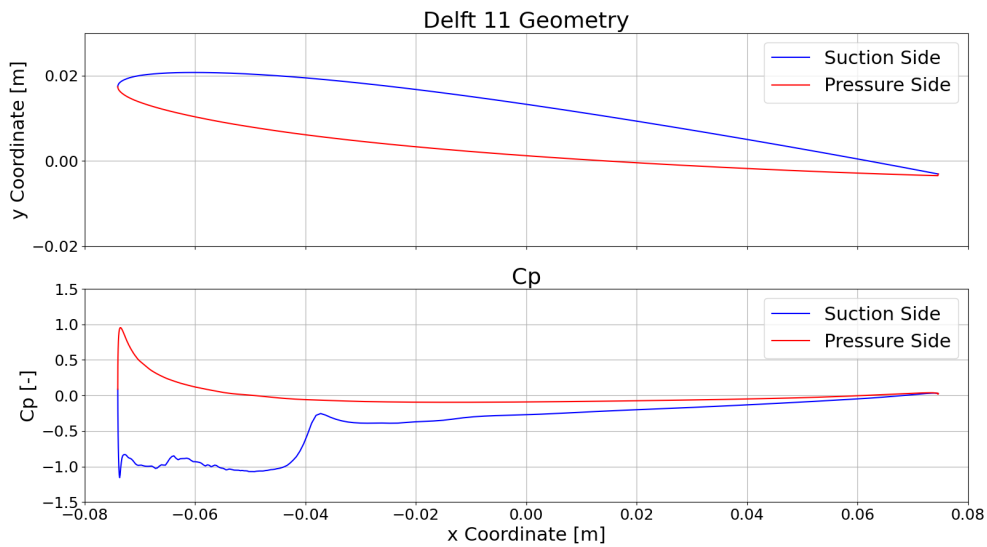
Figure 5.40: Representation of C_P on the Delft Twist 11 pressure side and suction side.
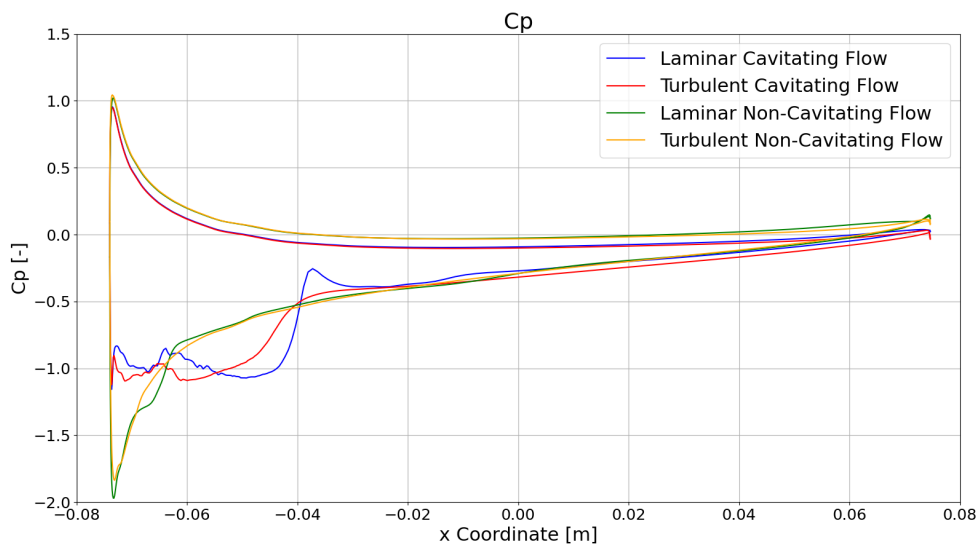
Figure 5.41: Delft Twist 11 C_P comparison.

Unlike in the NACA009 simulation results, the laminar flow pressure distribution curve shows a peak, which is probably the result of cavity implosions occurring around that area of the foil. Unfortunately, no experimental results were found for comparison. Instead the results were compared to the simulation results from [35]. The simulations in [35], are of flows with a different σ_{cav}, but the curve shapes were determined to show a similarity to the results in this thesis.

Finally, the lift and drag coefficients were measured.
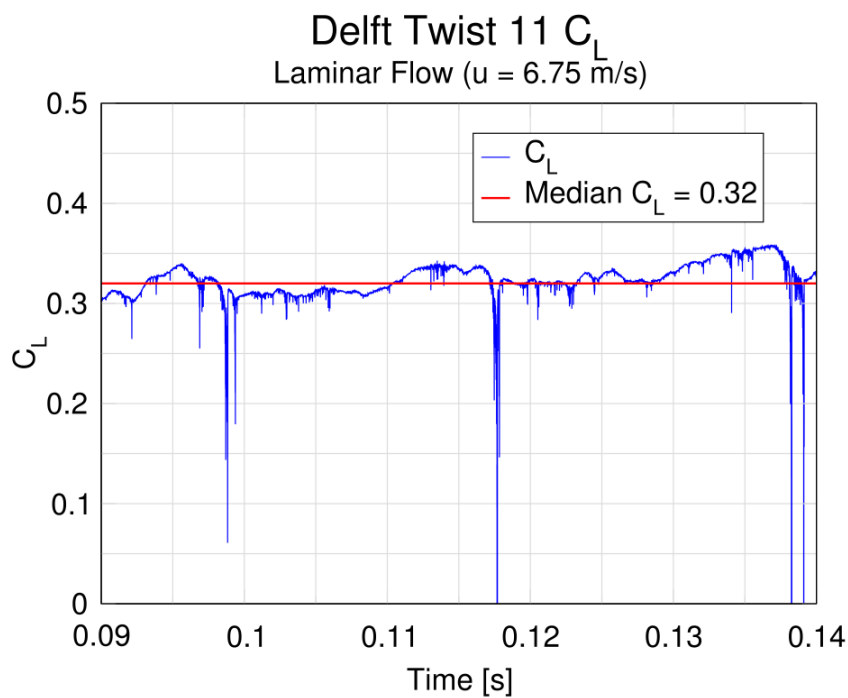
Figure 5.42: Delft Twist 11 laminar flow C_L.
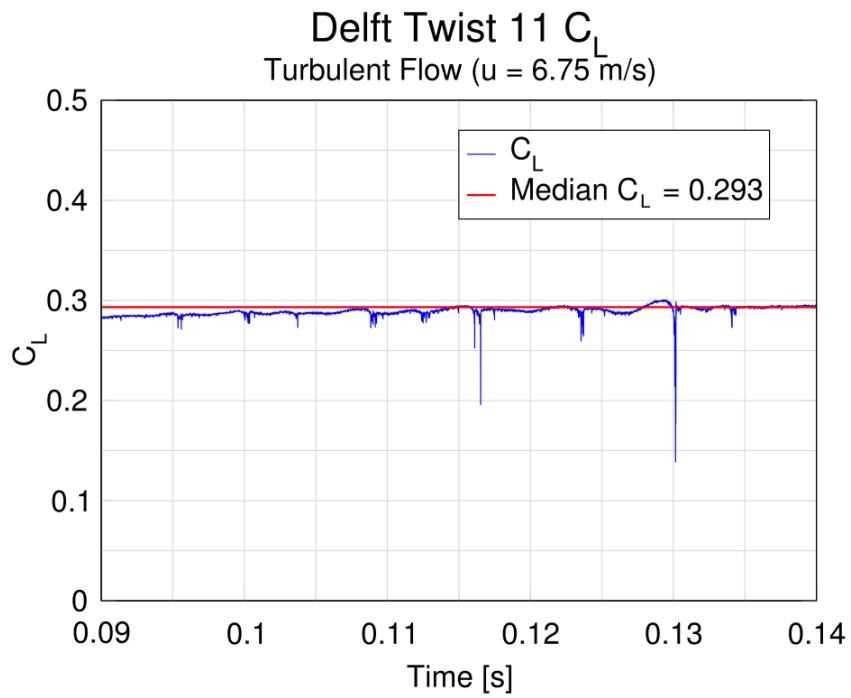
Figure 5.43: Delft Twist 11 turbulent flow C_L.
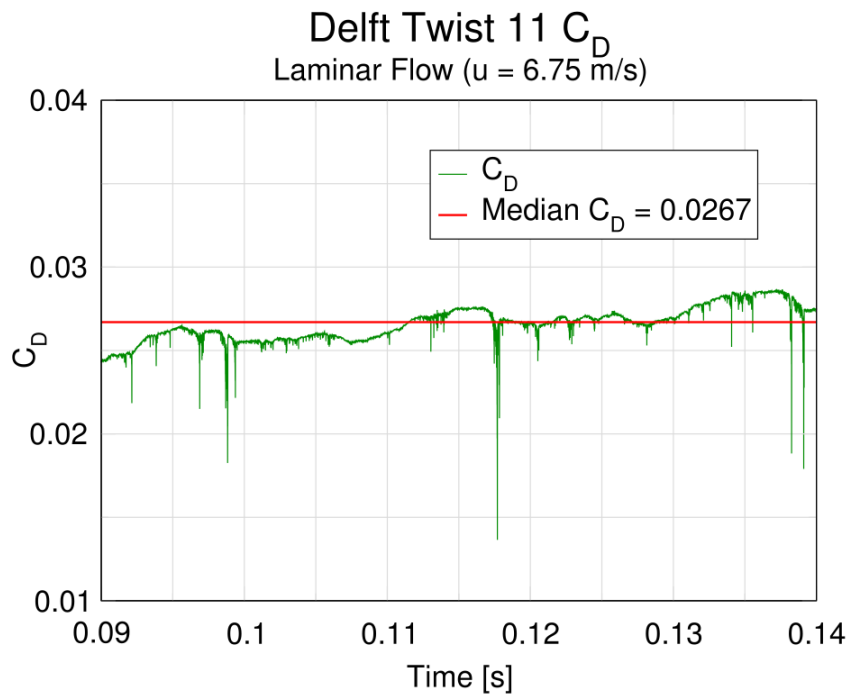
Figure 5.44: Delft Twist 11 laminar flow C_D.
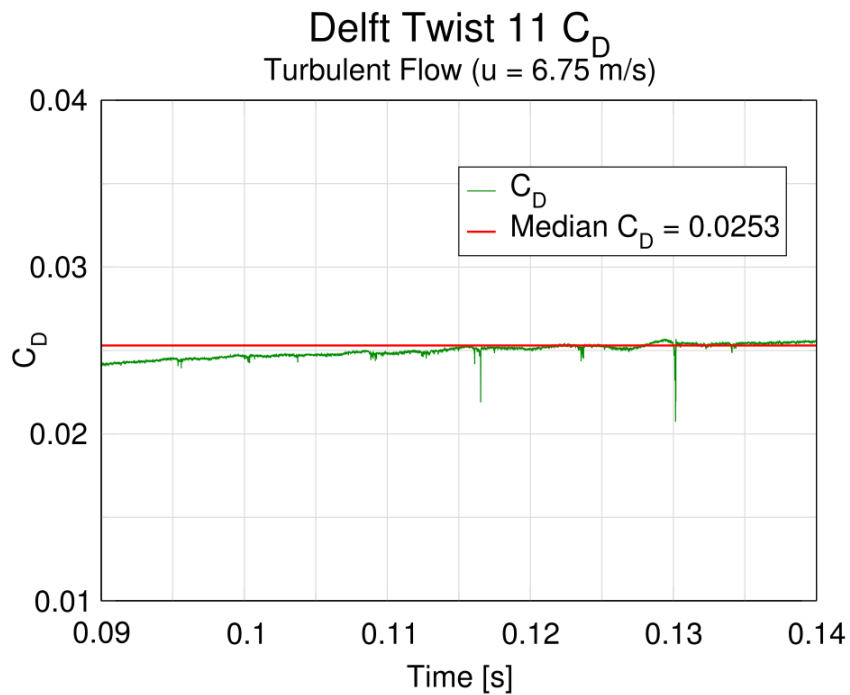
Figure 5.45: Delft Twist 11 turbulent flow C_D.

Again, there is less variation of the lift and drag force in the turbulent flow. The spikes from the cavity implosions are much more pronounced in the laminar flow simulations, which is most likely the result of the detached cavities being larger in volume in those conditions.

The results were compared to the simulation and experimental results from [7] and [9].

Table 5.4: Lift coefficient values for the Delft Twist 11 Hydrofoil.

Delft Twist 11 C_L	
Experimental [7]	0.53
LES [7]	0.45
RANS $k - \omega$ SST with correction [9]	0.43
Laminar Flow Simulation	0.32
Turbulent Flow Simulation	0.293

Evidently, the simulations in this thesis grossly underestimated the lift in the cavitating flow around the Delft Twist 11 foil. However, it is worth mentioning, that Fig 5.42 and Fig. 5.43 depict the lift coefficient values actually increasing in time. This could mean that, if a longer time frame was taken into account, fully evolved sheet cavities may have been achieved and the simulations may have shown different results.

5.4. Closure

The current chapter presented the results of the research performed for this thesis. A comparison to experimental results and other CFD research was shown, and the similarities and differences were explained.

The final chapter will present a brief commentary on the whole research and conclude the thesis.

6 | Conclusion

6.1. Conclusion

This thesis presented the One Fluid Homogenous Mixture cavitation models and, using CFD, attempted to determine the accuracy with which these models predict cavitation behavior. Specifically, the Schnerr-Sauer model [8], and its implementation in the `interPhaseChangeFoam` solver was tested. The thesis also researched the effect of turbulence in cavitating flows. It produced mixed results.

On the one hand, simulations of cavitating flows that do not take turbulence into account, produce accurate images of cavitation behavior. The shedding and transport of the cavities seems correct when compared to photographs of experiments. The lift force values measured on the wings also depict stochastic behavior, which is in accordance with the nature of cavitation. The spikes in the signal, which represent implosions of the detached cavities, are possibly excessive. This could stem from the model equations, that take the bubble growth inertia into account. The lack of turbulence causes the bubbles to grow without control. As mentioned in the thesis, simulations of laminar flows are incorrect, because the Reynolds numbers of the flows are far beyond the turbulence threshold.

When turbulence is taken into account, the cavitation behavior randomness is greatly diminished, and it becomes almost periodic. The turbulence dissolves the detached cavitation bubbles very quickly, and the implosions are perhaps understated. In the 2D NACA009 simulations, turbulence caused the attached sheet cavity to be extremely stable, which caused the shedding phenomenon to be much less pronounced.

For the NACA009 simulations, the results were attempted to be verified by mea-

suring the average pressure distribution on the foil. The distribution didn't drastically diverge from the experimental results, and the laminar flow models produced a correct curve shape, but the results in neither case, completely matched the experimental measurements. The mere averaging of the pressure, may present a problem. The flow was simulated in a time frame of 0.2 seconds, which is very short. Although the cavitation shedding was correctly determined to be of a high frequency, the randomness of the cavitation behavior coupled with the small time frame, may have impacted the correctness of averaging the solution.

For the Delft Twist 11 foil simulations, the time frame may have been an even bigger factor. If a longer time frame was taken into account, the cavitation images may have shown different results. Unfortunately, a transient simulation on a large 3D mesh takes a lot of time to solve. Nonetheless, the images can be compared to experimental results, and the shape and behavior of the cavitation is corroborated by photographs of experiments. The simulation doesn't fully capture all the details of the shedding process, but it is impossible to determine if that is due to the not completely evolved nature of the sheet vapor cavities in the simulation, or due to the cavitation model shortcomings. Also, in the Delft Twist 11 foil simulations, it is more difficult to determine whether the turbulent or the laminar flow produces a more physically correct image of the cavitation. The lift coefficient values in the Delft Twist 11 foil simulations were drastically underestimated, however, again, it is impossible to determine whether this is due to the length of the time frame of the flow that was simulated.

In summation, the results of the validation are somewhat inconclusive. Turbulence modeling should be taken into consideration when studying cavitating flows. Current research favors the LES model and RANS with correction coefficients, but both present an underestimation of the lift coefficient by more then 12%. Research also indicates that the RANS $k-\omega$ SST model can mimic those results, but in the case of this thesis it was perhaps modeled incorrectly. This may indicate that a more comprehensive cavitation model must be taken into account to reach a correct solution for the lift force. For additional research on the basis of this thesis, a modification of the turbulence model should be attempted and the time frame that is simulated should be increased.

Appendices

A | Discretisation Parameters

Appendix A gives an overview of the discretisation settings used in this thesis

```
ddtSchemes
{
    default Euler;
}

gradSchemes
{
    default                         cellMDLimited Gauss linear 1;
}

divSchemes
{
    default                     Gauss linear;
    div(phi,U)                  Gauss upwind;
    div(phi,k)                  Gauss upwind;
    div(phi,omega)              Gauss upwind;
    div(phi,R)                  Gauss upwind;
    div(R)                      Gauss linear;
    div(phi,nuTilda)            Gauss upwind;
    div((nuEff*dev(T(grad(U)))))    Gauss linear;
}

laplacianSchemes
{
    default                     Gauss linear limited 1;
}

interpolationSchemes
{
    default         linear;
}

snGradSchemes
{
    default         limited 1;
}

wallDist
{
    method meshWave;
}
```

Bibliography

[1] J. P. Franc. Physics and control of cavitation, 2006.

[2] Luka Balatinec. An overview of rotor-stator interfaces for computational fluid dynamics simulations in turbomachinery. Master's thesis, University of Zagreb, 2019.

[3] G. Kuiper. Course materials for cavitation in ship propulsion, January 2010.

[4] O. Coutier-Delgosha, B. Stutz, A. Vabre, and S. Legoupil. Analysis of cavitating flow structure by experimental and numerical investigations. *Journal of Fluid Mechanics*, 578:171–222, 2007.

[5] P. Dupont. *ETUDE DE LA DYNAMIQUE D'UNE POCHE DE CAVITATION PARTIELLE EN VUE DE LA PREDICTION DE L'EROSION DANS LES TURBOMACHINES HYDRAULIQUES*. PhD thesis, ECOLE POLYTECHNIQUE FEDERALE DE LAUSANNE, 1993.

[6] E.-J. Foeth. *The structure of three-dimensional sheet cavitation*. PhD thesis, Technische Universiteit Delf, 2008.

[7] R. E. Bensow. Simulation of the unsteady cavitation on the the delft twist11 foil using rans, des and les. *Second International Symposium on Marine Propulsors*, 2011.

[8] J. Sauer and G.H. Schnerr. Unsteady cavitating flow – a new cavitation model based on modified front capturing method and bubble dynamics. *Proc. Fluids Engineering Summer Conference*, 2000.

[9] Bian Ji, Xianwu Luo, Yulin Wu, Xioaxing Peng, and Yunling Duan. Numerical analysis of unsteady cavitating turbulent flow and shedding horse-shoe vortex structure around a twisted hydrofoil. *International Journal of Multiphase Flow*, 51:33–43, 2013.

[10] F. Moukalled, L. Mangani, and M. Darwish. The finite volume method in computational fluid dynamics, 2016.

[11] H. Jasak. Course materials for Numerical Methods in Continuum Mechanics Method, February 2018.

[12] S. V. Patankar and D.B. Spalding. A calculation procedure for heat, mass and momentum transfer in three-dimensional parabolic flows. *International Journal of Heat and Mass Transfer*, 15:1787–1806, 1972.

[13] R. I. Issa. Solution of the implicit discretized fluid flow equations by operator splitting. In *Mechanical Engineering Report*, Imperial College, London, UK, 1982.

[14] T. Holzmann. Mathematics, Numerics, Derivations and OpenFOAM, December 2016.

[15] F. Menter and T. Esch. Elements of industrial heat transfer prediction. In *16th Brazilian Congress of Mechanical Engineering (COBEM)*, Uberlandia, Brazil, 2001.

[16] B.E. Launder and D.B. Spalding. The numerical computation of turbulent flows. *Computer Methods in Applied Mechanics and Engineering*, 3:269–289, 1974.

[17] B.E. Launder and B.I. Sharma. Application of the energy-dissipation model of turbulence to the calculation of flow near a spinning disc. *Letters in Heat and Mass Transfer*, 1:131–137, 1974.

[18] David C. Wilcox. *Turbulence Modeling for CFD*. DCW Industries, 1993.

[19] F.R. Menter, M. Kuntz, and R. Langtry. Ten years of industrial experience with the sst turbulence model. *Turbulence, Heat and Mass Transfer*, 4:625–632, 2003.

[20] Nasa turbulence modeling resource. http://turbmodels.larc.nasa.gov/sst.html. Accessed: 12-02-2019.

[21] A. Hellsten. Some improvements in menter's k-omega-sst turbulence model. In *29th AIAA Fluid Dynamics Conference*, Albuquerque,NM,USA, 1998.

[22] C. E. Brennen. *Cavitation and Bubble Dynamics.* Oxford University Press, 1995.

[23] Lord Rayleigh. On the pressure developed in a liquid during the collapse of a spherical cavity. *The London, Edinburgh, and Dublin Philosophical Magazine and Journal of Science, Seires 6*, 34:94–98, 1917.

[24] M. S. Plesset. The dynamics of cavitation bubbles. *Journal of Applied Mechanics*, 16:277–282, 1949.

[25] Daniele Liuzzi. *Two-Phase Cavitation Modelling.* PhD thesis, University of Rome -La Sapienza-, 2012.

[26] Chao-Kun Huang. *Turbulence and cavitation: applications in the NSMB and Open-FOAM solvers.* PhD thesis, Universite de Strasbourg, 2017.

[27] M. Ishii. Thermo-fluid dynamic theory of two phase flow. 1975.

[28] C.L. Merkle, J. Feng, and P.E.O. Buelow. Computational modelling of the dynamics of sheet cavitation. *Proc. 3rd Intl Symp. on Cavitation*, 2:307–314, 1998.

[29] R.F. Kunz, D.A. Boger, D.R. Stinebring, T.S. Chyczewski, J.W. Lindau, H.J. Gibeling, S. Venkateswaran, and T.R. Govindan. A preconditioned implicit method for two-phase flows with application to cavitation prediction. *Computer Fluids*, 29:849–875, 2000.

[30] A. Kubota, H. Kato, and H. Yamaguchi. A new modelling of cavitating flows: a numerical study of unsteady cavitation on a hydrofoil section. *Journal of Fluid Mechanics*, 240:59–96, 1992.

[31] A.K. Singhal, M.M. Athavale, H.-Y. Li, and Y. Jiang. Mathematical basis and validation of the full cavitation model. *Journal of Fluids Engineering*, 124:617–624, 2002.

[32] R.T. Knapp, J.T. Daily, and F.G. Hammit. *Cavitation.* McGraw Hill, 1970.

[33] Y.S. Wei and R.J. Sadus. Equations of state for the calculation of fluid-phase equilibria. *AlChE Journal*, 46:169–196, 2000.

[34] Tom van Terwisga. The delft twist 11 foil test case. `http://maritimetechnology.tudelft.nl/SHS/`, 2010.

[35] T. Maquil, B. Cankurt, P. Schiller, S. Yakubov, M. Abdel-Maksoud, and T. Rung. Rans simulation of the delft twist 11 foil, 2011.